PARTICLE IDENTIFICATION WITH CALORIMETERS FOR THE MEASUREMENT OF THE RARE DECAY $K^+ \to \pi^+ \nu\bar{\nu}$ AT NA62

DISSERTATION
ZUR ERLANGUNG DES GRADES

"Doktor der Naturwissenschaften"

AM FACHBEREICH PHYSIK, MATHEMATIK UND INFORMATIK DER
JOHANNES GUTENBERG UNIVERSITÄT IN MAINZ

Riccardo Aliberti
GEBOREN IN MONCALIERI

MAINZ, AUGUST 2018

1. Gutachter: -

2. Gutachter: -

Datum der mündlichen Prüfung: 22.01.2019

Abstract

Flavour physics is one of the most powerful fields in the search of new physics beyond the Standard Model. The kaon sector with the rare decay $K^+ \to \pi^+\nu\bar{\nu}$ provides one of the cleanest and most promising channels.

NA62, a fixed target experiment at the CERN SPS, aims to measure $K^+ \to \pi^+\nu\bar{\nu}$ branching ratio with 10% precision to test the Standard Model up to an energy scale of hundreds of TeV. The rejection of the muon background is a crucial task for the measurement of the $K^+ \to \pi^+\nu\bar{\nu}$ decay. The information from the Cherenkov and the Muon Veto detectors are not sufficient to achieve the required $\mathcal{O}(10^7)$ muon suppression and an additional factor of 10^2 has to be reached with a purely calorimetric particle identification.

The calibration of the hadron calorimeter (HAC) represents an important challenge, which requires the development of innovative techniques. Since electrons and photons are absorbed by the electromagnetic calorimeter (LKr), the response of the HAC to electromagnetic showers is calibrated by exploiting stopped high energy muons. The obtained HAC energy resolution meets all the demands.

The information about energy and shape of the showers detected by the LKr and HAC are combined into a Boosted Decision Trees algorithm to classify the impinging particles as muons, pions or electrons. The particle identification algorithm allows a muon rejection of 10^5 (including suppression from the muon veto detector) for 90% pion efficiency.

Zusammenfassung

Flavourphysik ist einer der Bereiche, in dem die Suche nach neuer Physik jenseits des Standardmodells am aussichtsreichsten ist. Mit dem seltenen Zerfall $K^+ \to \pi^+\nu\bar{\nu}$ bietet der Kaonsektor einen der saubersten und vielversprechendsten Kanäle.

Das Fixed-Target-Experiment NA62 am CERN SPS strebt eine Messung der $K^+ \to \pi^+\nu\bar{\nu}$-Zerfallsrate mit einer Präzision von 10% an. Dies entspricht einem Test des Standardmodells bis zu einer Energieskala von einigen Hundert TeV. Die Elimination des Untergrunds aus Myonen ist dabei eine wesentliche Voraussetzung für die $K^+ \to \pi^+\nu\bar{\nu}$-Messung. Da die Cherenkov- und Myonvetodetektoren nicht die komplette erforderliche Unterdrückung von $\mathcal{O}(10^7)$ leisten können, müssen die Kalorimeter eine zusätzliche Myonunterdrückung von $\mathcal{O}(10^2)$ erreichen.

Die Kalibration des Hadronkalorimeters (HAC) ist daher eine wesentliche Aufgabe, welche die Entwicklung neuer, innovativer Techniken nötig macht. Da Elektronen und Photonen im elektromagnetischen Kalorimeter (LKr) absorbiert werden, wird das HAC mit Hilfe von elektromagnetischen Schauern von vollständig im Kalorimeter gestoppten, hochenergetischen Myonen kalibriert. Die damit erreichte Energieauflösung des Hadronkalorimeters erfüllt sämtliche Anforderungen.

Die im LKr und HAC gemessenen Schauerprofile und -energien dienen als Input für einen sogenannten Boosted Decision Tree, der die einfallenden Teilchen als Myonen, Pionen oder Elektronen klassifiziert. Der Algorithmus zur Teilchenidentifikation erreicht dabei eine Unterdrückung von 10^5 (einschließlich der Information des Myonvetodetektors) bei einer Effizienz von 90% für Pionen.

Contents

Introduction

The Standard Model of particle physics (SM) is a quantum field theory which provides a unified framework for the description of elementary particle interactions through electromagnetic, strong and weak processes. The SM was developed in the 20^{th} century thanks to the theoretical and experimental efforts of brilliant physicists like Richard Feynman, Steven Weinberg and Chien-Shiung Wu.
The Standard Model provides accurate predictions for all processes involving elementary particles and is confirmed by the experimental observations. The discovery in 2012 of a new particle at a mass of about 125 GeV/c^2 completed the observation of the basic elements composing the SM with a candidate for the Higgs Boson.
Despite the great success of this theory, there are strong hints that the current formulation of the Standard Model represents an effective theory integrating out physics processes at (presently) inaccessible energy scales. The observation of neutrino oscillations has confuted the SM assumption of the massless nature of neutrinos. Moreover, the evidence of dark matter from cosmological observation does not find any source candidate within the SM particles.
New physics processes are therefore likely to exist and to be located either at very low energy scales (below the eV scale) or above the energies currently accessible to direct searches (up to few TeV). In the latter case, precision measurements of flavour physics transitions (like kaon and B-meson decays) represent the perfect environment to search for flaws in the Standard Model, probing for new physics at energies as high as several hundreds of TeV.

NA62, a fixed target experiment at CERN, aims to discover new physics effects in rare kaon decays. The $K^+ \to \pi^+ \nu\bar{\nu}$ transition represents a golden channel in this search and the goal of NA62 is to achieve 10% precision on the measurement of $Br(K^+ \to \pi^+ \nu\bar{\nu})$. This branching ratio is very sensitive to any effect arising from new physics thanks to the Flavour Changing Neutral Current (FCNC) nature of the transition combined with a quadratic CKM suppression. The Standard Model provides a precise prediction for $Br(K^+ \to \pi^+\nu\bar{\nu})$, reading

$$Br\left(K^+ \to \pi^+\nu\bar{\nu}\right) = (8.4 \pm 1.0) \times 10^{-11}$$

The uncertainty is dominated by the current precision on the CKM parameters, in particular for the V_{td} matrix element, while the hadronic contribution is below the percent level.

The signature of a $K^+ \to \pi^+\nu\bar{\nu}$ event is the detection of a beam kaon, decaying into a pion and nothing else. Due to the tiny branching ratio and the weak signature of this process, all the other kaon decays represent background sources to the measurement. The $K^+ \to \mu^+\nu_\mu$ decay ($K_{\mu 2}$), with a branching ratio of about 63%, is one of the most dangerous backgrounds to the $K^+ \to \pi^+\nu\bar{\nu}$ detection. Even though the measurement of the event kinematics provides a strong suppression of the $K_{\mu 2}$ background, a μ-π separation of 10^7 has to be achieved by particle identification. The combined information of the Muon Veto and the RICH detector is not sufficient to fulfill this requirement and an additional muon rejection factor of about 100 is required from the analysis of showers in the calorimeters.
The analysis of the data collected by NA62 in 2016 lead to the observation of a first $K^+ \to \pi^+\nu\bar{\nu}$ signal event. In that analysis a particle identification algorithm, based on a Boosted Decision Trees technique developed by the author, was used for the μ-π separation in the calorimeters. The algorithm relies on a calibration of the hadron calorimeter (HAC) obtained from Monte Carlo simulations, providing sub-optimal detector performance.
This work presents an innovative procedure for the calibration of HAC response to electromagnetic shower based on stopped high energy muons. The calibration of the HAC response to pions and the inter-calibration with the electromagnetic calorimeter are also described. Following the improved energy reconstruction, an updated version of the above mentioned particle identification algorithm has been implemented leading to a significant improvement of the pion efficiency.

Chapter 1

The $K \to \pi\nu\bar{\nu}$ decay: a Golden Probe of the Standard Model

The present status of particle physics has many open questions that do not have answers inside the framework of the Standard Model (SM) – a brief review of the Standard Model can be found in [1]. The very different mass scales from neutrinos up to the *top* quark, dark matter and the baryon/anti-baryon asymmetry in the universe are just a few examples of missing pieces in the puzzle of describing nature in a fully consistent model. Until now direct searches of new physics at the LHC have not provided any evidence of new particles or processes up to the scale of few TeV.

Complementary to the LHC, indirect searches provide an effective tool to explore mass scales which are completely unreachable by the current accelerator machines. As an example, in 1970 the *charm* quark was predicted by Glashow, Iliopoulos and Maiani, before the direct observation, following the experimental evidence that $\Delta S = 2$ transitions were strongly disfavoured with respect to $\Delta S = 1$ processes [2]. Along these lines, SM predictions of several processes are under investigation. The kaon decay $K \to \pi\nu\bar{\nu}$ provides one of the most interesting transitions in both the neutral ($K_L \to \pi^0\nu\bar{\nu}$) and the charged ($K^+ \to \pi^+\nu\bar{\nu}$) channel.

The decays take place through Flavour Changing Neutral Current processes with quadratic GIM suppression, resulting in SM branching ratios of the order of 10^{-11} [3]:

$$Br\left(K^+ \to \pi^+\nu\bar{\nu}\right) = (8.4 \pm 1.0) \times 10^{-11} \tag{1.1}$$

$$Br\left(K_L \to \pi^0\nu\bar{\nu}\right) = (3.4 \pm 0.6) \times 10^{-11} \tag{1.2}$$

These processes are theoretically very clean, since uncertainties from hadronic contribution can be estimated to a few percent by extrapolating the $K \to \pi$ transition form factor from the leading semi-leptonic kaon decays $K \rightarrow \pi l \nu$ (K_{l3}, with $l = e, \mu$) via an isospin rotation [4]. Many expansions of the SM predict significant contributions to the branching ratio of this process by new particles inside the Feynman loop diagrams (Figure 1.1). The $K \rightarrow \pi \nu \bar{\nu}$ decays are therefore sensitive to new physics up to energy scales of several hundreds of TeV [5] and precise measurements of both the charged and the neutral decay represent a severe check of the Standard Model.

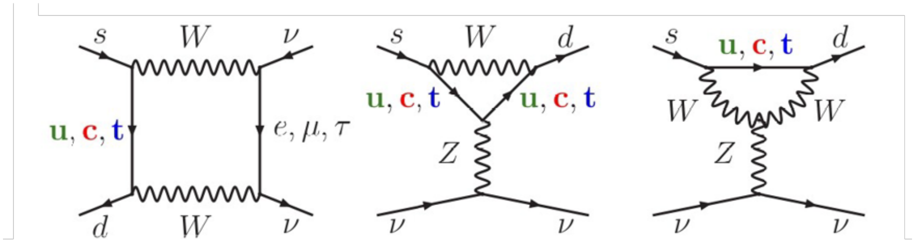

Figure 1.1 – Feynman diagrams of the $s \rightarrow d\nu\bar{\nu}$ process, leading to the $K \rightarrow \pi\nu\bar{\nu}$ decay.

The experimental measurement of $K \rightarrow \pi\nu\bar{\nu}$, however, presents a significant difficulty due to the weak signature of the decay and the very tiny branching ratio. The current results are $Br(K_L \rightarrow \pi^0\nu\bar{\nu}) < 2.6 \times 10^{-8}$ at 90% CL and $Br(K^+ \rightarrow \pi^+\nu\bar{\nu}) = \left(17.3^{+11.5}_{-10.5}\right) \times 10^{-11}$ from the E391a [6] and the E949 [7] Collaborations respectively.

The KOTO [8] experiment currently running at J-PARC in Japan aims to observe a few $K_L \rightarrow \pi^0\nu\bar{\nu}$ SM events by 2021 [9]. Meanwhile at CERN the NA62 experiment intends to measure the $K^+ \rightarrow \pi^+\nu\bar{\nu}$ branching ratio with 10% precision.

1.1 Theoretical Framework

1.1.1 The CKM Matrix and the Unitary Triangles

The study of the rare decays $K^+ \rightarrow \pi^+\nu\bar{\nu}$ and $K^0_L \rightarrow \pi^0\nu\bar{\nu}$ is strongly related to the Cabibbo-Kobayashi-Maskawa (CKM) Matrix of weak interaction.

The CKM matrix was introduced in 1973 by Makoto Kobayashi and Toshihide Maskawa [10]. The matrix was needed in order to allow CP-violating transitions, as experimentally observed in hadron decays, in the description of the weak interaction proposed by Weinberg. In the proposed – and then accepted – approach the weak interaction sees quarks as mixture of the flavour (and mass) eigenstates. The CKM matrix, shown in Equation 1.3, connects the quark flavour eigenstates to those of the weak interaction, determining the probability of transition between different quark flavours.

$$\begin{pmatrix} d \\ s \\ b \end{pmatrix}_{weak} = \begin{pmatrix} V_{ud} & V_{us} & V_{ub} \\ V_{cd} & V_{cs} & V_{cb} \\ V_{td} & V_{ts} & V_{tb} \end{pmatrix} \times \begin{pmatrix} d \\ s \\ b \end{pmatrix}_{flavour} = V_{CKM} \times \begin{pmatrix} d \\ s \\ b \end{pmatrix}_{flavour} \tag{1.3}$$

The standard formulation of the weak interaction provides a mixing between quarks of down-type (d, s, b), leaving the up-type unmixed. This choice is arbitrary and has a historical reason: when Cabibbo [11], as first, supposed the mixing between quarks, the known quarks were *down*, *strange* and *up* so that the mixing could be imposed only between down-type quarks.

The magnitude of the mixing between the quarks is proportional to $|V_{ij}|^2$. In Equation 1.4 the measured CKM elements [12] are shown. The diagonal terms are clearly dominating, therefore transitions between quarks of the same doublet (*up-down*, *charm-strange*, and *top-bottom*) are strongly favoured.

$$V_{CKM} = \begin{pmatrix} 0.97420 \pm 0.00021 & 0.2243 \pm 0.0005 & (3.94 \pm 0.36) \times 10^{-3} \\ 0.218 \pm 0.004 & 0.997 \pm 0.017 & (42.2 \pm 0.8) \times 10^{-3} \\ (8.1 \pm 0.5) \times 10^{-3} & (39.4 \pm 2.3) \times 10^{-3} & 1.19 \pm 0.025 \end{pmatrix} \tag{1.4}$$

The CKM matrix is a 3 × 3 matrix, containing 9 complex elements. However, the requirements of unitarity and of gauge invariance reduce the number of free parameters to only four: three angles and a complex phase (responsible for the CP violation).

The CKM matrix is often considered in the Wolfenstein parametrization [13], which is generated by the 4 parameters λ, A, ρ and η defined as follows:

$$\lambda = \frac{V_{us}}{\sqrt{|V_{ud}|^2+|V_{us}|^2}} \tag{1.5}$$

$$A = \frac{V_{cb}}{\lambda^2\sqrt{|V_{ud}|^2+|V_{us}|^2}} \tag{1.6}$$

$$\rho = \frac{Re(V_{ub})}{A\lambda^3} \tag{1.7}$$

$$\eta = \frac{Im(V_{ub})}{A\lambda^3} \tag{1.8}$$

In this parametrization each matrix term is expanded as a power series in the parameter $\lambda \simeq V_{us}$. Generally, due to the smallness of λ, it is possible to consider only the first few terms of the expansion:

$$V_{CKM} = \begin{pmatrix} 1-\frac{\lambda^2}{2} & \lambda & A\lambda^3(\rho - i\eta) \\ -\lambda & 1-\frac{\lambda^2}{2} & A\lambda^2 \\ A\lambda^3(1-\rho-i\eta) & -A\lambda^2 & 1 \end{pmatrix} + O(\lambda^4) \tag{1.9}$$

The constraints on the unitarity of the CKM matrix can be expressed through a set of equations:

$$\sum_{i=\{u,c,t\}} |V_{ik}|^2 = 1 \quad \text{for the diagonal elements } i = k \tag{1.10}$$

$$\sum_{i=\{u,c,t\}} V_{ij}^* V_{ik} = 0 \quad \text{for the other terms } j \neq k \tag{1.11}$$

Equation 1.11 with $j = s$ and $k = d$ results in the relation:

$$V_{us}^* V_{ud} + V_{cs}^* V_{cd} + V_{ts}^* V_{td} = 0 \tag{1.12}$$

which defines, in the complex plane (ρ, η) of the Wolfenstein parametrization, the unitarity triangle shown in Figure 1.2 where $\bar{\rho}$ and $\bar{\eta}$ are defined as follows:

$$\bar{\rho} = \rho\left(1-\frac{\lambda^2}{2}\right) \tag{1.13}$$

$$\bar{\eta} = \eta\left(1-\frac{\lambda^2}{2}\right) \tag{1.14}$$

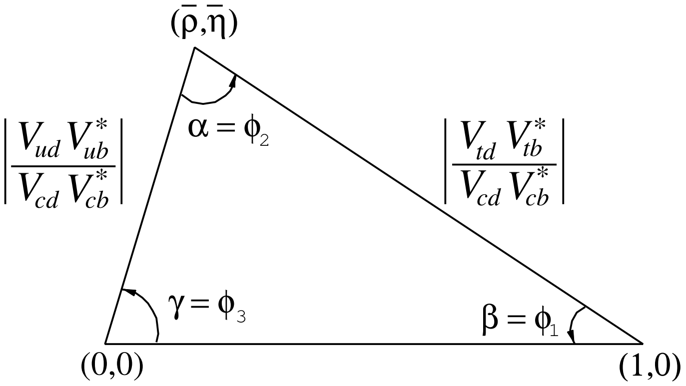

Figure 1.2 – Unitarity Triangle [12].

1.1.2 The $K \to \pi\nu\bar{\nu}$ decay

The $K^+ \to \pi^+\nu\bar{\nu}$ and $K_L \to \pi^0\nu\bar{\nu}$ transitions, in the Standard Model, arise from an $s \to d\nu\bar{\nu}$ process at quark level. This transition happens through a Flavour Changing Neutral Current (FCNC) which is forbidden at tree level within the Standard Model. The $K \to \pi\nu\bar{\nu}$ decays can proceed through either one of the two penguin or a box Feynman diagrams, involving the exchange of W and Z bosons, as shown in Figure 1.3.

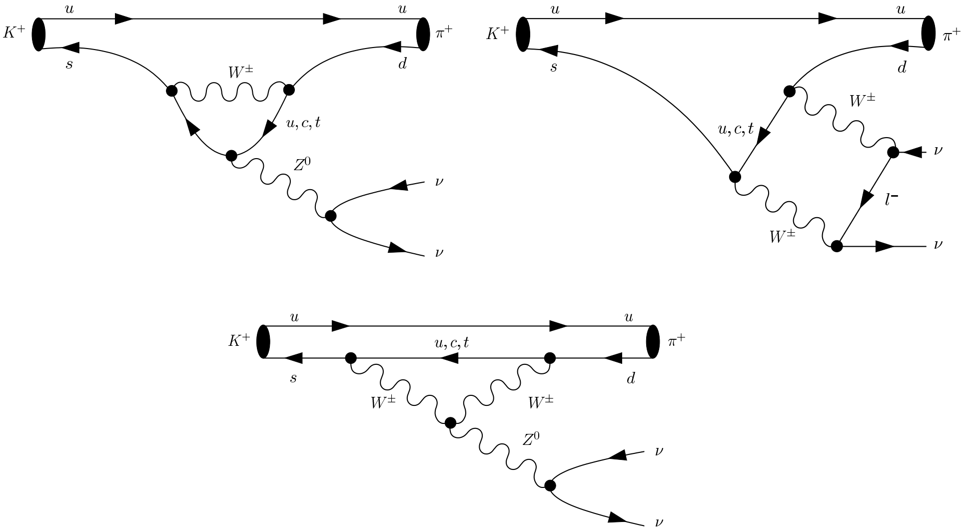

Figure 1.3 – Feynman diagrams of the $K^+ \to \pi^+\nu\bar{\nu}$ decay [14]. The $K_L \to \pi^0\nu\bar{\nu}$ process is described by the same diagrams, where the spectator quark is changed from u to d.

Each diagram consists in the sum of three different terms: the interaction can be mediated by each one of the up-type quarks (*up*, *charm* or *top*). The contribution of a quark flavour $q = u, c, t$ to the decay amplitude can be written in the approximate form

$$A_q \simeq \frac{m_q^2}{m_W^2} V_{qs}^* V_{qd} \tag{1.15}$$

The ratio between the quark and the W boson squared masses is the leading term in the definition of the quark flavour hierarchy in the decay. The diagrams containing an *up* quark are therefore strongly suppressed, while those with a *top* quark are the dominant contributors. Loops with *charm* provide a small, but non-negligible contribution to the total decay rate.

The $K \to \pi\nu\bar{\nu}$ decay amplitudes are, hence, dominated by the short range interaction. This allows to consider the Fermi-like effective Hamiltonian [14]

$$H_{eff} = \sum_{l=\{e,\mu,\tau\}} \frac{G_F}{\sqrt{2}} \frac{\alpha}{2\pi sin^2\Theta_W} \left(V_{ts}^* V_{td} X(x_t) + V_{cs}^* V_{cd} X_{NL}^l\right) (\bar{s}d)_{V-A} \left(\bar{\nu}_l \nu_l\right)_{V-A} \tag{1.16}$$

where:

- G_F is the Fermi coupling constant
- α is the electromagnetic fine structure constant
- Θ_W is the Weinberg angle
- $x_t = m_t^2/M_W^2$ is the ratio between *top* and W squared masses
- X_{NL}^l and $X(x_t)$ are the functions describing the *charm* and *top* quark contributions
- $(\bar{s}d)$ and $(\bar{\nu}\nu)$ are the vector-axial weak neutral currents for the quarks and the neutrinos

The hadronic contribution to the $K^+ \to \pi^+\nu\bar{\nu}$ and the $K_L \to \pi^0\nu\bar{\nu}$ decays are obtained by isospin rotation from the leading semileptonic kaon decays K_{l3} ($K \to \pi l\nu$ with $l = e, \mu$) as described in [4]. The branching ratios for the two processes can be written as:

$$Br\left(K_L \to \pi^0\nu\bar{\nu}\right) = k_L \left(\frac{Im\lambda_t}{\lambda^5} X\left(x_t\right)\right)^2 \tag{1.17}$$

$$\begin{aligned} Br\left(K^+ \to \pi^+\nu\bar{\nu}\right) = k_+(1+\Delta_{EM}) \Bigg[& \left(\frac{Im\lambda_t}{\lambda^5} X\left(x_t\right)\right)^2 \\ & + \left(\frac{Re\lambda_t}{\lambda^5} X\left(x_t\right) + \frac{Re\lambda_c}{\lambda} P_c\left(X\right)\right)^2 \Bigg] \end{aligned} \tag{1.18}$$

where $\lambda \simeq |V_{us}|$ from the Wolfenstein parametrization, $\lambda_i = V_{is}^* V_{id}$ (with $i = c, t$), Δ_{EM} the electromagnetic radiative corrections, $P_c(X)$ the *charm* loop contributions, k_+ and k_L summarizing the remaining constants and the hadronic corrections with the most recent values [3]

$$k_+ = (5.173 \pm 0.025) \times 10^{-11} \left[\frac{\lambda}{0.225}\right]^8 \tag{1.19}$$

$$k_L = (2.231 \pm 0.013) \times 10^{-10} \left[\frac{\lambda}{0.225}\right]^8 \tag{1.20}$$

Hence the Standard Model predictions are [3]:

$$Br\left(K^+ \to \pi^+\nu\bar{\nu}\right) = (8.4 \pm 1.0) \times 10^{-11} \tag{1.21}$$

$$Br\left(K_L \to \pi^0\nu\bar{\nu}\right) = (3.4 \pm 0.6) \times 10^{-11} \tag{1.22}$$

The measurement of both these branching ratios will provide the determination of two elements of the unitarity triangle as shown in Figure 1.4:

1. the measurement of the $Br(K_L \to \pi^0\nu\bar{\nu})$ allows to directly extract the height of the unitarity triangle. The $K_L \to \pi^0\nu\bar{\nu}$ is a CP-violating process and only the imaginary part of the decay amplitude is involved.
2. the $K^+ \to \pi^+\nu\bar{\nu}$ branching ratio is, instead, contributed by both the imaginary and the real component of the decay amplitude. The imaginary part is the same as for the K_L branching ratio, while the real part is provided by the *top*, within the unitarity triangle, and by the *charm*. The $K^+ \to \pi^+\nu\bar{\nu}$ decay provides, therefore, the measurement of one side of the unitarity triangle (after the correction for the *charm* contribution).

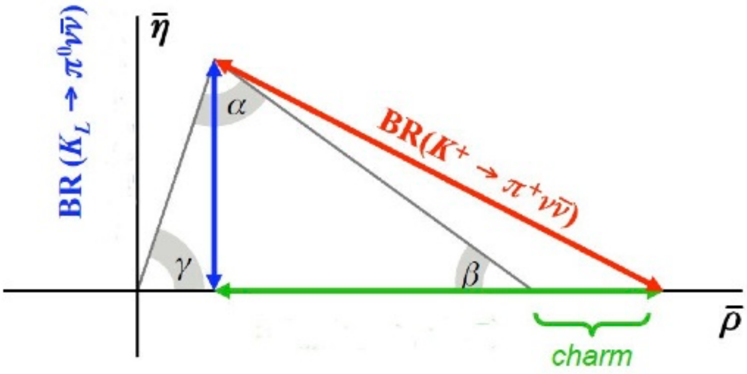

Figure 1.4 – Relation between the unitarity triangle and the $K \to \pi\nu\bar{\nu}$ decays. The blue line shows the imaginary contribution to the branching ratio, common to both charged and neutral kaon decays, the green line is the real component of the branching ratio with the *charm* contribution highlighted (only in the K^+ decay), and the red line shows the relation of the $K^+ \to \pi^+\nu\bar{\nu}$ decay to the triangle.

The measurement of both branching ratios provides the determination of the V_{td} element of the CKM matrix. Comparing this result with the measurement performed on the β angle in the B-physics experiments [15] and on $|V_{ts}|, |V_{td}|$ from B mixing [16] [12], the consistency of the Standard Model can be carefully verified.

The FCNC nature of these decays, combined by the strong suppression of the leading CKM transition, make the $K \to \pi\nu\bar{\nu}$ decays a golden channel for the search of new physics beyond the Standard Model at energy scales nowadays inaccessible to direct searches. Heavy particles, like the SUSY squarks, or new vector bosons, like the Z' introduced by many models, could enter the loops or mediate the $s \to d\nu\bar{\nu}$ transition, determining consistent changes in the decay amplitudes. A precise measurement of the $K^+ \to \pi^+\nu\bar{\nu}$ and $K_L \to \pi^0\nu\bar{\nu}$ decays allows to probe for new physics up to energy scales of several hundreds of TeV, as explained in [5].

1.2 Current Experimental Results and Perspectives

1.2.1 $K_L \to \pi^0\nu\bar{\nu}$

The presently best limit on the $K_L \to \pi^0\nu\bar{\nu}$ branching ratio has been obtained by the E391a experiment at the KEK proton synchrotron [6]. The experiment employed a K_L pencil beam, with a central kinetic energy of about 2 GeV, combined with an hermetic photon detection system. 8.7×10^9 kaon decays were collected with the decay-in-flight technique. The analysis provided a single event sensitivity of 1.1×10^{-9} and no event was observed. A 90% confidence level limit was set to:

$$Br\left(K_L \to \pi^0\nu\bar{\nu}\right) < 2.6 \times 10^{-8} \text{ (90\% CL)}$$

Despite E391a did not observe any signal event, it proved the sensitivity of the adopted experimental scheme.

The KOTO experiment [8] [9], currently running at J-PARC, aims to reach the sensitivity of the Standard Model prediction by 2021 and to perform the measurement of the branching ratio with 10% precision by 2024. KOTO uses the same experimental technique as E391a with an upgraded detector to reduce the background from beam neutrons. First results from the KOTO collaboration published in 2017 [17] have shown that the experiment (with just 100 hours of data taking in 2013) is able to already reach the E391a experiment single event sensitivity.

The complexity and the importance of this measurement does certainly motivate the construction of a concurrent experiment, which could compare and validate the KOTO results. For this reason a new experiment, KLEVER [18], is currently under discussion at CERN with the aim to perform a $Br(K_L \to \pi^0\nu\bar{\nu})$ measurement with 10% precision starting from 2026.

1.2.2 $K^+ \to \pi^+\nu\bar{\nu}$

The E787 and E949 experiments, at Brookhaven National Laboratories (BNL), provide the only available measurement of the $K^+ \to \pi^+\nu\bar{\nu}$ branching ratio [7]. The study was performed stopping 710 MeV/c kaons inside a target made of scintillation fibers, situated at the center of the experimental apparatus inside a magnetic field of 1 T. The analysis required the identification of both the kaon, by a Cherenkov detector, and the pion, by the reconstruction of the full decay chain $\pi^+ \to \mu^+ \to e^+$ combined with the absence of signals in the veto detectors.

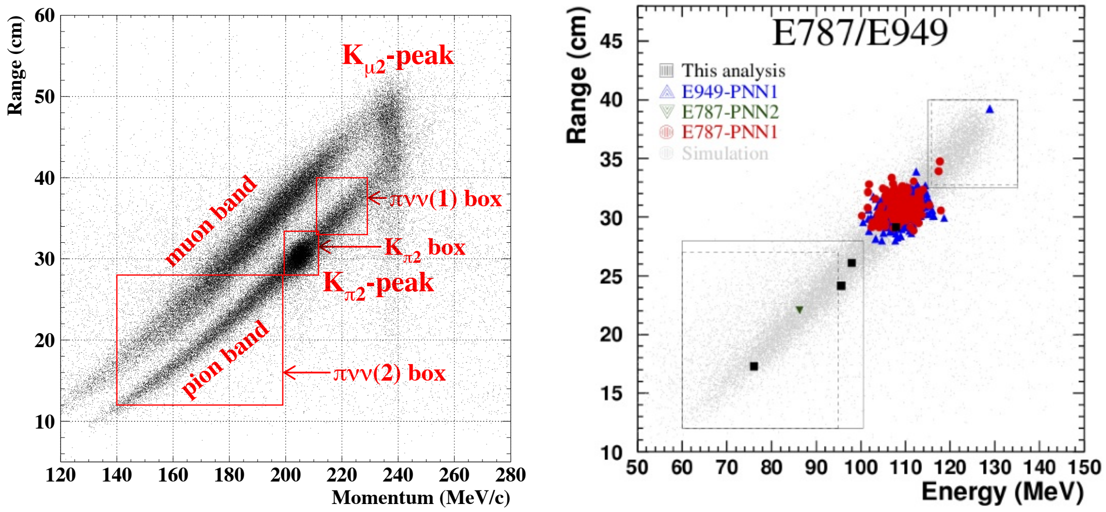

Figure 1.5 – Distribution of the discriminating variables used for the E747 and E949 signal region definition [7]. On the left for events with a single charged particle in the final state. The leading kaon decays are highlighted: $K^+ \to \mu^+\nu_\mu$ ($K_{\mu 2}$) and $K^+ \to \pi^+\pi^0$ ($K_{2\pi}$) as well as the signal regions ($\pi\nu\nu(1,2)$ boxes). On the right the final result of the combined data sample of E747 and E949 experiments.

The signal regions were defined in a 2-dimensional plane by the range of the daughter particle in the scintillator and its energy, as shown on the left of Figure 1.5. The analysis of the data collected within four years of operation (1995 – 1998 with the E747 experiment, and 2002 with the upgraded E949 apparatus) lead to the observation of 7 signal candidates as shown on the right of Figure 1.5. The branching ratio was measured as:

$$Br(K^+ \to \pi^+\nu\bar{\nu}) = 1.73^{+1.15}_{-1.05} \times 10^{-10} \tag{1.23}$$

The NA62 experiment, currently taking data at CERN, aims to improve and reduce the uncertainty on the $K^+ \to \pi^+\nu\bar{\nu}$ branching ratio to 10%. NA62 exploits a different technique based on kaon decay-in-flight. The analysis of the data collected during the 2016 allowed to almost reach the Standard Model sensitivity and a first signal candidate has been observed [19].

Chapter 2

The NA62 Experiment

The NA62 experiment is located in the CERN research site of Prevéssin-Moëns (France), also known as North Area (NA). The apparatus is hosted in the same experimental hall (ECN3) previously occupied by the NA31 and NA48 experiments, from which part of the infrastructure was inherited.

As described before, the main purpose of NA62 is the measurement of $Br\left(K^+ \to \pi^+\nu\bar{\nu}\right)$ with 10% precision. The experimental apparatus – beam line and detector – has been specifically designed in order to fulfil the requirements of the measurement.

In the following the strategy and the apparatus adopted by NA62 are briefly reviewed, further and more detailed informations can be found in [20] and in [21]. All the figures and data are from these two references.

2.1 Measurement Strategy

NA62 is a fixed-target experiment and aims to detect $K^+ \to \pi^+\nu\bar{\nu}$ events by their decay-in-flight. A $75\,\mathrm{GeV}/c$ secondary hadron beam containing kaons is produced and selected by impinging protons on a beryllium target.

A $K^+ \to \pi^+\nu\bar{\nu}$ event is detected as a beam particle, identified as a kaon, which matches a track in the detector, classified as a pion, and nothing else. All the main kaon decays and the in-time beam activity represent dangerous sources of background, due to the tiny branching ratio of the signal and the weakness of its signature. The strategy for the $K^+ \to \pi^+\nu\bar{\nu}$ measurement, which has driven the choice for the apparatus design, is based on the following keystones:

- **High Intensity Beam:** the decay-in-flight allows a better background suppression with respect to the decay-at rest technique, but on the other hand requires a far more intense beam. The kaon content in the secondary hadron beam is only 6%, and just 15% of these happen to decay within the fiducial region.

- **Good Timing:** working in a high intensity configuration, where the beam particle rate approaches the GHz limit, requires a $O(100\text{ ps})$ time resolution when combining the measurements of beam particles and decay products.

- **Precise Measurement of Kinematics:** a precise measurement of kaon and pion directions and momenta allows to accurately reconstruct the event kinematics. In particular the kinematic variable $m^2_{miss} = (P_{K^+} - P_{\pi^+})^2$ provides an excellent tool to discriminate the major kaon decays. Two signal regions for the $K^+ \to \pi^+\nu\bar{\nu}$ decay are defined between the three major kaon decays $K_{\mu 2}$ $(K^+ \to \mu^+\nu_\mu)$, $K_{2\pi}$ $(K^+ \to \pi^+\pi^0)$ and $K_{3\pi}$ $(K^+ \to \pi^+\pi^+\pi^-)$ as shown in Figure 2.1. Only a fraction of about 10^{-4} of events from these decays is expected to fall inside the signal region in the restricted track momentum region $[15, 35]$ GeV/c

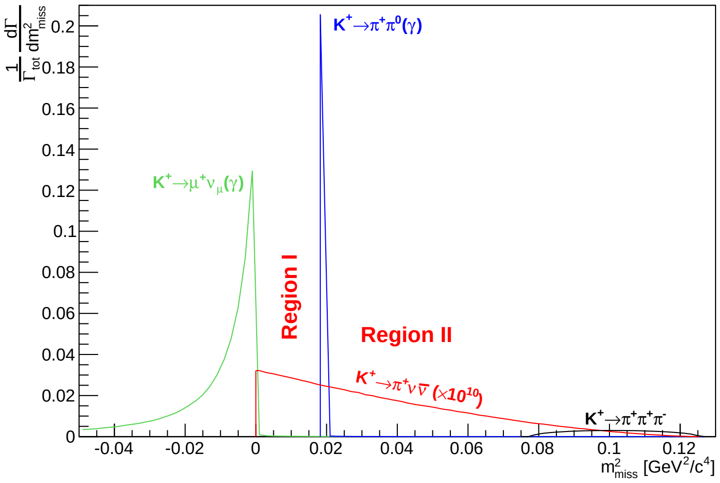

Figure 2.1 – Distribution of the m^2_{miss} kinematic variable for the $K^+ \to \pi^+\nu\bar{\nu}$ signal and for the main backgrounds [21].

- **Hermetic Photon Detection:** the $K^+ \to \pi^+\pi^0$ represents, with a branching ratio of about 20%, the second largest decay channel for charged kaons. A strong rejection for this background can be achieved by exploiting the kinematics, but also an efficient detection of the photons from the following $\pi^0 \to \gamma\gamma$ decay is crucial to reject events with mis-measured kinematic variables.

- **Efficient Particle Identification:** the signature of the $K^+ \to \pi^+\nu\bar{\nu}$ decay is the presence of a beam kaon, a pion and nothing else. Several processes can mimic this configuration. The most important – as the most abundant – is the $K^+ \to \mu^+\nu_\mu$ decay ($Br = 63.6\%$), where the muon is misidentified as a pion. In order to keep the background at a 10% level, a 10^7 muon rejection is needed. An efficient particle identification system is therefore an imperative requirement for NA62.

2.2 Kaon Beam

A 400 GeV/c proton beam is extracted from the SPS ring using the slow-extraction technique and driven, through the so-called P42 beam line, to impinge a 40 cm long beryllium target (T10). About 33×10^{11} protons are extracted in a 4.8 s long pulse with an almost flat intensity profile.

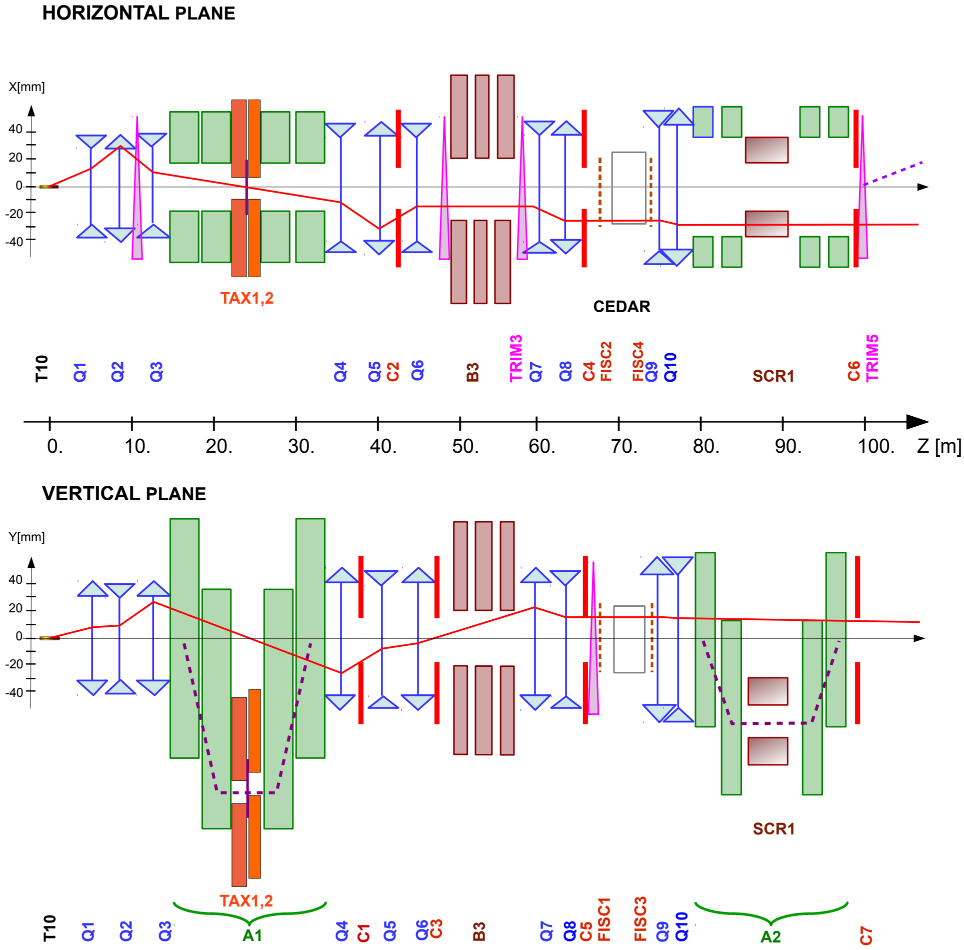

Figure 2.2 – Scheme of K12 beam line: the lines shows the trajectory followed by a 75 GeV/c positively charged particle when produced on-axis (dashed-black) and with the limiting angles of 2.7 mrad horizontal and 1.5 mrad vertical (solid-red) [21].

The K12 beam line, shown in Figure 2.2, follows the T10 target and is devoted to the charge and momentum selection of the secondary hadron beam. A 95 cm long copper-collimator, with selectable hole size, follows the T10 target, absorbing particles generated in the interaction with the extreme borders.
A triplet of quadrupole magnets (Q1-3) followed by an achromat (A1) focuses the beam particles and deflects the beam by 11 cm in the vertical direction (y-axis), selecting 75 GeV/c positively charged particles with about 1% precision. Inside the achromat, the beam passes through two beam dump units (TAX1-2) which absorb particles not satisfying the selection criteria. The TAXes can be closed in order to obtain different data taking conditions like muon runs or to perform searches for exotic particles [22].
A series of quadrupoles and collimators (Q4-10 and C1-C7) perform further selection and focussing of the beam. A series of tungsten foils, up to 5 mm thick (1.3 X_0), placed between the TAX1 and TAX2, degrade positron energies to reject them in the second achromat (A2), while inducing minimal losses of hadrons due to scattering. The beam crosses steel plates inserted in the B3 dipole magnet through a 4 cm wide field-free bore. The magnetic field in the surrounding iron allows to sweep away off-axis muons of both signs. A horizontal steering magnet (TRIM5), placed at the end of the selection line, applies a 1.2 mrad deflection of the hadron beam on the positive x-axis in order to compensate the effect of the spectrometer magnet about 95 m downstream and therefore keeping beam particles within the transportation tube until the dump at end of the experiment.
The particle flow of the hadron beam counts 750×10^6 particle/s which are composed as follows:

- Pions: 70%
- Protons: 23%
- Kaons: 6%
- Muons: $< 1\%$

2.3 Experimental Apparatus

The NA62 apparatus extends over more than 200 m, from the T10 target until the beam dump at the end of the experiment, while the transverse acceptance is limited to 35 mrad thanks to the large boost of the particles. The scheme of the detector is shown in Figure 2.3 and can be subdivided into two regions:

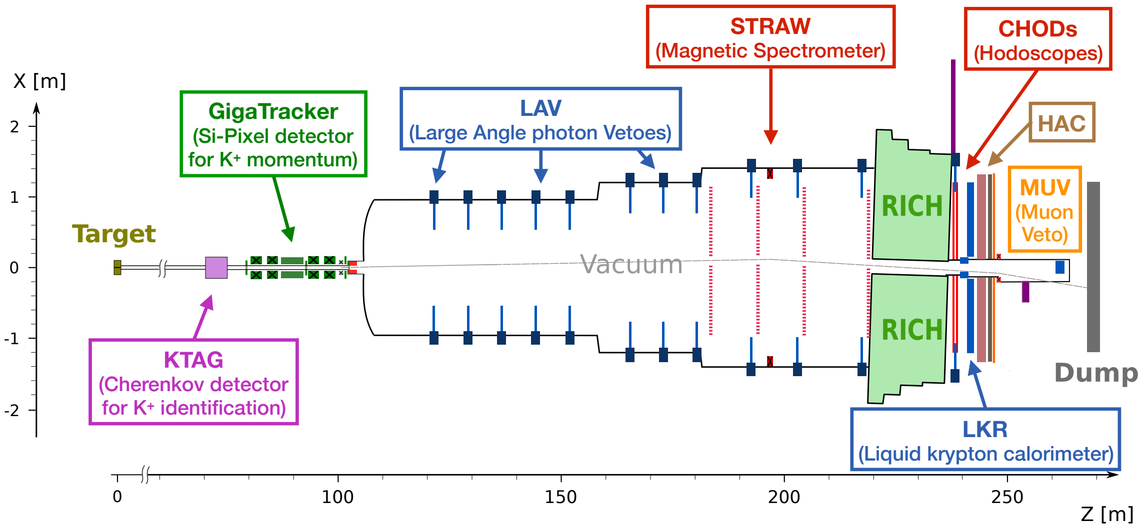

Figure 2.3 – Scheme of the NA62 apparatus [21].

- **Upstream** detectors dedicated to beam kaon identification and measurement.
- **Downstream** detectors providing the characterization of the kaon decay products.

The beginning of the Downstream region, between the CHANTI and the first station of the spectrometer, is the fiducial decay region for the event selection corresponding to $[105, 165]$ m after the target. In order to obtain the best measurement of the event kinematics and, at the same time, limit the amount of beam particle scattered into the detector acceptance, the beam tube and the decay region up to the last station of the STRAW spectrometer is kept in vacuum (about $10^{-5} - 10^{-6}$ mbar).

2.3.1 Upstream Detectors: Beam Characterization

The measurement of the beam particles direction and momentum is a crucial point for NA62. However, since only 6% of the beam particle rate is due to kaons, the identification of K^+ with an excellent time resolution is indispensable to correctly classify the events. Three systems, integrated in the K12 beam line, are considered as upstream detectors:

- KTAG
- GTK
- CHANTI

KTAG: Kaon Identification

The KTAG is a differential Cerenkov counter designed to identify K^+ mesons and to measure their time with a resolution of about 100 ps. This detector employs a 1.6 m long volume filled with nitrogen at 1.75 bar (ambient temperature) as radiator coupled with an optical box to detect the Cherenkov light produced by beam particle at a defined angle. An optical system selects and transmits the light to eight arrays of photomultipliers (referred as octants) placed on a circle. The coincidence between several octants (usually at least 5) provides the kaon tagging.

The pressure of the gas can be changed to select different masses or momenta of the crossing particles. Special runs are acquired regularly along the data taking periods to perform pressure scans in the detector, determining the effective beam particle composition (kaons, pions and protons as shown in Figure 2.4) and the best working pressure to select kaons, as well as to align the detector optics.

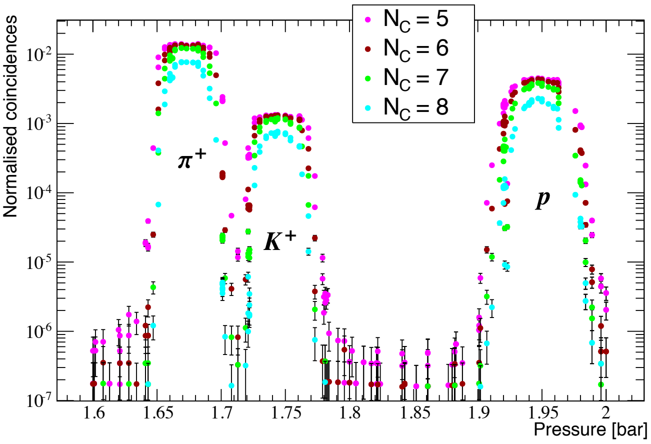

Figure 2.4 – Results of a KTAG pressure scan. The plot shows the rate of detected events at different pressure of the nitrogen radiator and for different number of minimum required octants coincidences. The three signal regions corresponding to pions, kaons and protons are clearly visible [21].

GTK: Beam Spectrometer

The deflection of the particle trajectories induced by the last achromat (A2) of the K12 beam line is used to measure momenta and directions of the beam particles. The beam spectrometer, Gigatracker (GTK), consists of three stations of silicon pixel detectors (GTK 1,2,3) installed around A2 as shown in Figure 2.5.

A GTK station consists of a 200 µm thin silicon sensor containing 18000 pixels of 300×300 µm^2. The readout electronics are directly attached to the sensor via bump-bonding. They consist of an assembly of 10 ASICs with fixed threshold discriminator

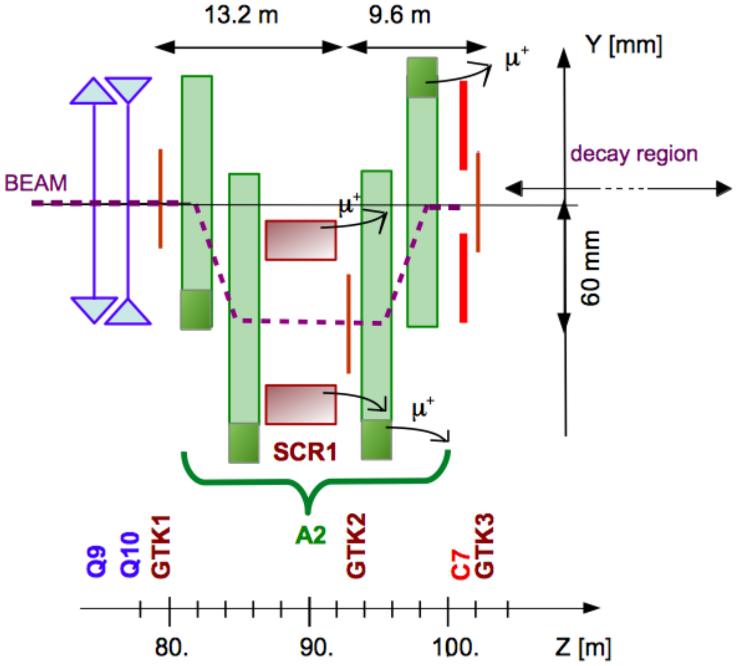

Figure 2.5 – Schematic view of the GTK in the beam line [21].

connected to a 97 ps time resolution TDC, measuring the times of threshold crossing in both the leading and the trailing edges to allow an offline time-walk correction. Each chip encodes and transmits the information recorded by the TDCs to a readout board out of the beam area via optical fibers. The whole detector is kept at a temperature of −15 °C through a micro-channels cooling plate glued on the readout in order to dissipate the heat generated by the readout electronics and to limit the radiation damage on the sensor. The complete assembly of a GTK station accounts for about 500 µm of silicon – 200 µm from the sensor, 100 µm from the readout chips and 200 µm from the cooling plated – equivalent to less than 0.5% X_0.
The Gigatracker provides a reconstruction of the beam particles with a precision of about 0.2% on the momentum and about 20 µrad on the direction. It shows also remarkable timing performance with about 200 ps resolution for the single station and 150 ps for reconstructed tracks.

CHANTI: Beam Interactions Veto

Beam particles interact with a very small probability with the GTK material. Particularly dangerous for the $K^+ \to \pi^+\nu\bar{\nu}$ measurement is the inelastic scattering of beam pions and kaons on the last station of the beam tracker (GTK3), that can mimic a signal event. Following the scattering, a pion enters the fiducial volume

with momentum and direction compatible with a signal event, while other charge particles produced in the event are emitted at large angle escaping the apparatus undetected by the downstream detectors. The CHANTI is, therefore, devoted to the detection of particles produced with a range of angles between 28.5 mrad and 1.37 rad with respect to the beam pipe.
The detector is composed of a series of 6 rectangular stations of scintillators following the last station of the beam spectrometer. By design, the CHANTI is required to have better then 2 ns time resolution in order to limit random losses due to overlapping events. This requirement has been fully satisfied: the detector timing has a precision at the level of about 800 ps.

2.3.2 Downstream Detectors: Decay Products Measurement and Classification

The downstream section of the NA62 apparatus is devoted to the characterization of the kaon decay products. In the perspective of the $K^+ \to \pi^+ \nu\bar{\nu}$ branching ratio measurement this translates, as discussed in 2.1, in four main tasks listed in the following with the involved detectors:

- Reconstruction of the kinematics: STRAW Spectrometer.
- Particle identification: RICH, electromagnetic and hadron calorimeters (LKr and HAC), MUV.
- Photon Rejection: LKr, LAV and SAV.
- Timing and Triggering: CHOD and NewCHOD.

As central proponents of this work, the calorimeters are described separately in Chapter 3.

STRAW: Spectrometer

The NA62 spectrometer (STRAW) represents the first tracking system based on straw tubes in vacuum. The STRAW detector is composed of 4 chambers distributed, almost equidistantly, over a length of 35 m along the beam direction, with a dipole magnet (MNP33) between the second and the third station providing an integrated field of 0.9 Tm. Four layers of straw tubes (views) provide, in each chamber, redundant information about the particle impact position (Figure 2.6). The horizontal and vertical tube orientation are complemented with the respective $\mp 45^\circ$

rotations respect to the x-axis, resolving ambiguities in presence of several crossing particles. The center of each STRAW station is displaced with respect to the apparatus axis in order to accommodate the deflection of the beam induced by the TRIM5 and the MNP33 magnets.

The spectrometer provides and excellent reconstruction of the particle momentum and direction. The resolution on the track momentum has been measured [21] as:

$$\frac{\sigma_p}{p} = 0.30\% \oplus 0.005\% \cdot p \text{ [GeV}/c] \tag{2.1}$$

and the angular resolution is about 60 µrad. Such good performance allows to reconstruct the kaon mass in $K^+ \rightarrow \pi^+\pi^+\pi^-$ events with a precision better than $1\,\mathrm{MeV}/c^2$.

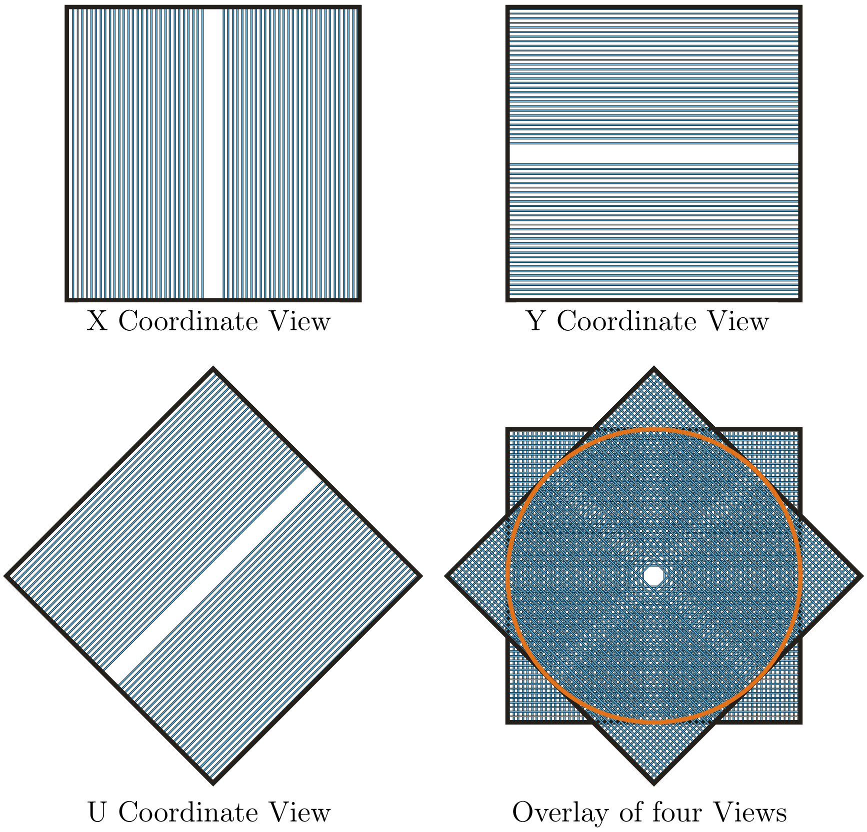

Figure 2.6 – Sketch of the 4 planes in a station of the STRAW tracker [20].

RICH: Particle Identification

The RICH, Ring Imaging Cherenkov detector, has been conceived in order to distinguish with high precision between pions and muons in a momentum range from

15 GeV/c up to 35 GeV/c. The detector (Figure 2.7) is built out of a 17.5 m long vessel filled with Neon gas at atmospheric pressure. A mosaic of 21 spherical mirrors – 19 with an hexagonal shape and 2, surrounding the beam tube, semi-hexagonal – reflects Cherenkov light toward two arrays of photomultipliers with a resulting focal length of about 17 m.

The measurement of the Cherenkov light radius, together with the STRAW momentum measurement, provides an excellent tool to separate between positrons, muons and pions, by reconstruction of the particle mass.

The RICH mirrors are kept precisely aligned employing piezo-motors connected to the mirrors though thin aluminium ribbons, thus allowing to adjust the orientation of each mirror separately. The RICH combines excellent particle identification performance with a precise event timing, approaching a resolution of 100 ps.

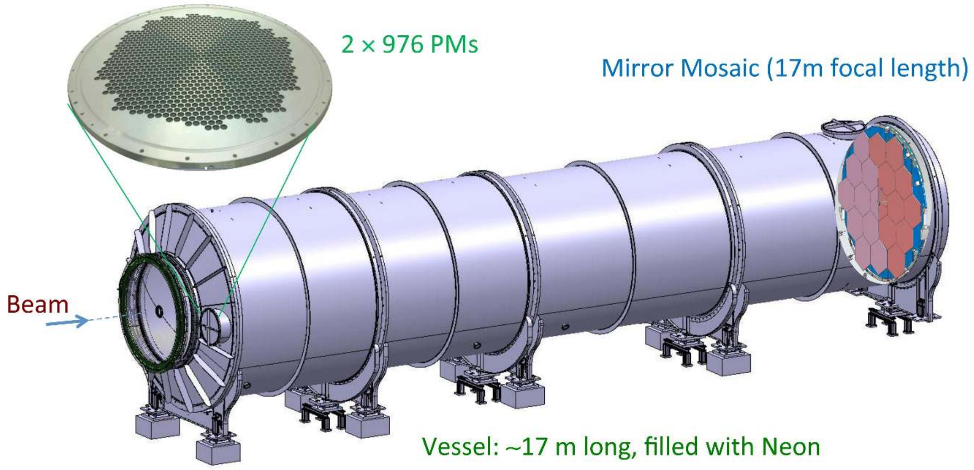

Figure 2.7 – Schematic view of the RICH detector [21].

MUV: Fast Muon Veto

The fast muon veto (MUV) frequently referred as MUV3, being the third element of the muon veto system after the front and back module of the hadron calorimeter, is required to provide an efficient rejection of final states with muons already at the trigger level.

The detector is composed of a 12×12 array of 5 cm thick scintillators, each readout by two photomultipliers facing directly the tiles. It is placed after the hadron calorimeter and shielded by a 80 cm iron wall (a particle tracked by the STRAW crosses a material amount equivalent to more than 14 interaction lengths before reaching

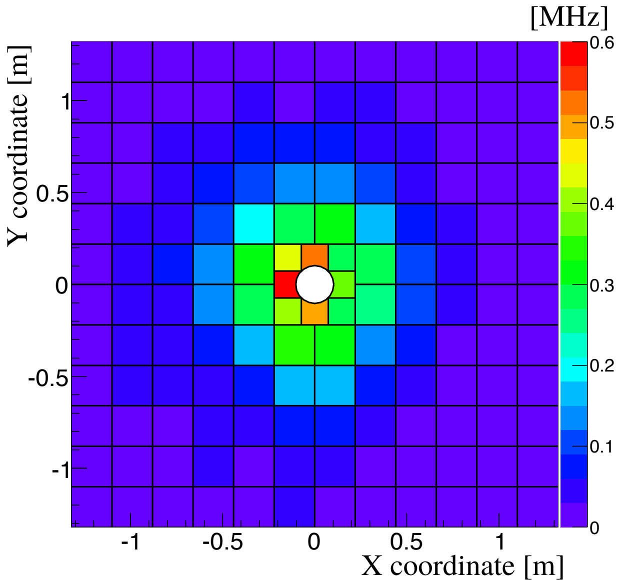

Figure 2.8 – MUV tiles geometry and expected rate at nominal intensity. The rate of the innermost left tile in red is 3.2 MHz, outside the selected axis range [21].

the MUV). A significant number of beam pions happen to decay into muons, which escape the beam pipe after the CHOD and illuminate the inner region of the MUV3 as shown in Figure 2.8. In order to minimize accidental losses due to such events, the fast muon veto provides a time resolution of about 500 ps.

LAV: Photon Detection at Large Angle

The rejection of photons is a crucial task in NA62. The apparatus was designed to achieve a rejection factor of 10^8 of the $K^+ \to \pi^+\pi^0$ decay through the detection of at least one of the photons from the $\pi^0 \to \gamma\gamma$ decay.

Low energy photons are often emitted at large angles with respect to the detector axis. With twelve stations (LAV1-12) of annular electromagnetic calorimeter, the large angle vetoes (LAV), provides the coverage for gammas emitted in the angular range of $[8.5, 50]$ mrad. The LAV stations have been built of lead glass blocks, refurbished from the electromagnetic calorimeter of the OPAL experiment. Each station contains 4 to 5 layers of lead glass blocks, slightly misaligned to avoid inefficiencies due to photons travelling in the gap between two blocks.

A test beam of a LAV station prototype was performed in Frascati (Italy) in 2009, using a tagged electron beam. The prototype showed an inefficiency of about 10^{-4} for a beam energy of 200 MeV and about 10^{-5} for 500 MeV electrons.

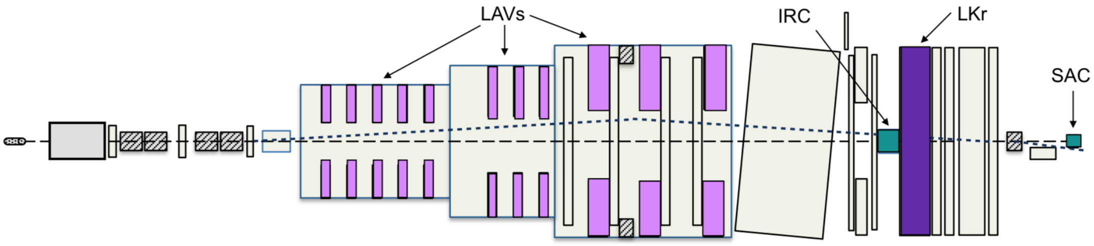

Figure 2.9 – Photon Veto System: in pink the 12 stations of the LAV and in green the two Small Angle Vetoes (SAV) [23].

SAV: Photon Detection at Small Angle

The energy sharing of the photons from a $\pi^0 \to \gamma\gamma$ decay can be, in rare cases, very unbalanced. In these events the very low energetic photon can escape the NA62 apparatus undetected – flying between two LAV stations – while the other may have such a large boost – due to π^0 momentum conservation – to remain within the beam tube. The small angle veto (SAV) system extends the photon detection coverage around and within the beam tube by employing two Shashlyk calorimeters, IRC and SAC. Both calorimeters are built with 1.5 mm thick scintillator-lead plates for a total of 19 radiation lengths X_0. The IRC, Intermediate Ring Calorimeter, is placed in front of and slightly overlaps the LKr, while the SAC, Small Angle Calorimeter, is at the end of the experiment line.

The IRC is a cylindrical tube divided in two halves: the first has 25 planes of scintillator and lead, while the second has 45. The detector is rotated by a small angle in the horizontal axis (x) in order to avoid detection inefficiencies due to photons crossing the detector within a wavelength-shifting fiber (WLS).

The SAC is inserted in the beam pipe in vacuum, right after the final magnet deflecting charged particles towards the dump region. The shape of the detector is a square, tilted by 23 mrad with respect to the beam axis in order to avoid losses due to photons crossing the detector within a WLS fiber. In different electron test beams the SAC showed an inefficiency ranging from 5×10^{-3} at 600 MeV down to 3×10^{-5} at 25 GeV.

CHOD

The CHOD – often referred as NA48-CHOD since it is inherited from the previous experiment – is one of the most important detectors in NA62. The detector consists of two consecutive planes of horizontally and vertically oriented scintillators (on the left of Figure 2.10), placed between the LAV12 and the IRC. Each scintillator spans half the detector size (about 1.2 m) and is 10 cm or 6.5 cm wide depending on the distance from the beam tube.

The timing performance of the CHOD is remarkable with a resolution of about 200 ps, representing the best candidate to improve the track time provided by the STRAW (about 5 ns time resolution).

During the data acquisition, the CHOD signals are also employed in the generation of the first level of trigger (L0).

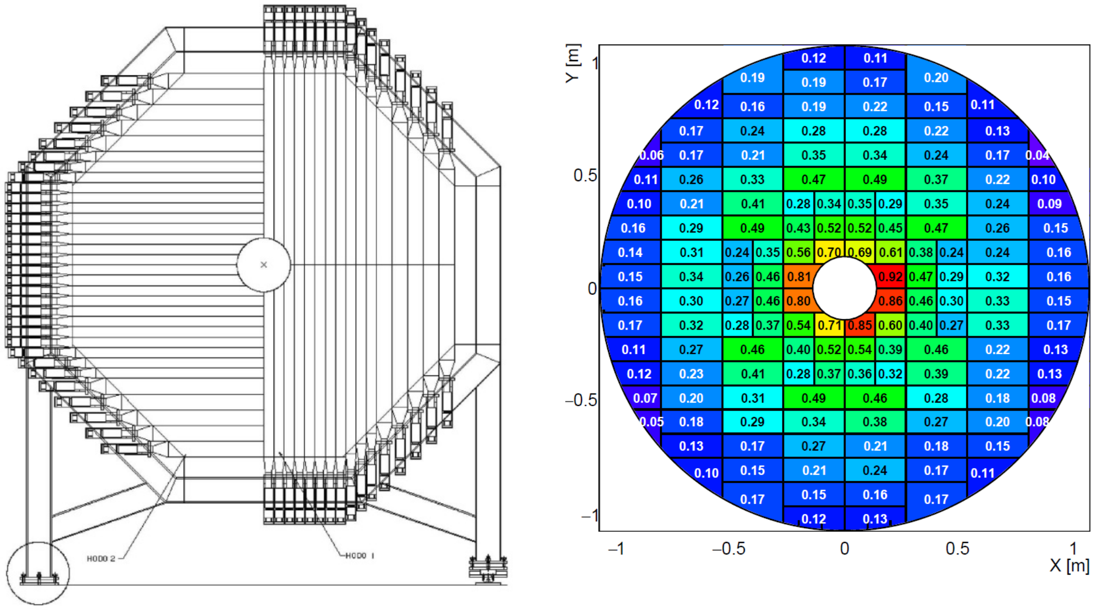

Figure 2.10 – Schematic view of the hodoscopes. On the left the CHOD [20], on the right the NewCHOD with the expected rate (in MHz) in each tile [21].

NewCHOD

The NA48-CHOD provides an excellent timing, but the long strips do not cope the high rate of the new experiment. The crossing of several particles, close in time, leads to a large number of fake coincidences between horizontal and vertical plans, limiting the trigger selection capability. A new hodoscope, the NewCHOD – also referred simply as CHOD in combination with NA48-CHOD – has been built with a rectangular tile structure. The NewCHOD (on the right of Figure 2.10) consists of 152 plastic scintillators mounted on a thin copper structure, alternately on the upstream and on the downstream side, with about 1 mm overlapping. In each tile, WLS fibers perform the light collection and are then readout on both the ends of the scintillator with silicon photomultipliers.

The detector was installed in front of the LAV12, just before the 2016 data taking. In that run period old fixed threshold discriminators were employed for the signal discrimination, degrading the timing capabilities of the NewCHOD to a resolution of about 1 ns. Starting from the 2017 data taking, the hodoscope is equipped with constant fraction discriminators (CFDs), with a significant improvement of the time resolution (below 500 ps).

The NewCHOD is an important contributor to the first trigger level. The detector geometry provides a simplified description of the event topology as the number and the distribution of the crossing charged particles.

2.4 Trigger and Data Acquisition (TDAQ)

NA62 faces a flux of beam particles of about 750 MHz, resulting in around 10 MHz of events with at least one particle in the acceptance of the downstream detectors (half of which due to kaon decays inside the fiducial region). For this reason a fast and reliable data acquisition system and an effective trigger chain is required to efficiently collect signal events, while keeping the data written on disk at a sustainable size.

An integrated system for both data acquisition and trigger generation was chosen. In this scheme the system analyses the same data that are then written on disk to selects the events, thus allowing an excellent control and reproducibility of the trigger conditions – representing a strict requirement for high precision measurements.

2.4.1 NA62 Data Flow

The data acquisition process in NA62 is schematically shown in Figure 2.11. The signals produced by the detectors are continuously digitized in readout boards employing TDCs or ADCs. The digitized pulses of some of the downstream detectors are analysed internally by the readout boards, providing the hardware level trigger processor (L0TP) with a simplified description of the event. When an event matches the selection requirements of the L0TP, a L0 trigger signal is issued and all the detector readout boards send their event data to the PC Farm.

In order to guarantee the correct association of triggered events with collected detector data, a precise synchronisation between the elements of the data acquisition system is a crucial requirement. This is achieved, at a level better than 100 ps, by

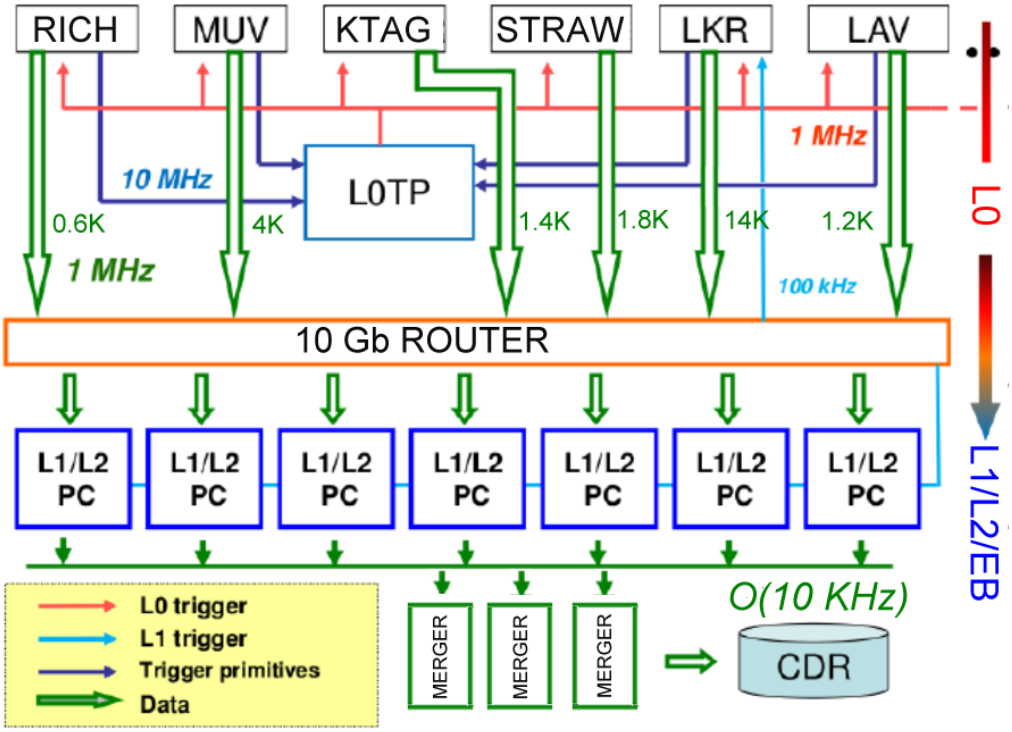

Figure 2.11 – A simplified overview of the NA62 data acquisition process [21].

distributing a clock – centrally generated with a frequency of 40.079 MHz – and command signals through a combined system of TTC [24] – Timing, Trigger and Control – and LTU [25] – Local Trigger Unit – boards. One second before the actual extraction of the beam, the SPS sends a warning signal to announce the arrival of the particles. This signal is translated in a initialization and synchronisation command, Start-Of-Burst (SOB), indicating the beginning of the data acquisition. An end-of-acquisition command, End-Of-Burst (EOB), is propagated about 0.5 s after the end of the spill. The machine spill is therefore the unit of the NA62 data taking and is usually referred as burst.
In the PC Farm, two levels of software triggers refine the event selection. Accepted events in a bursts are then written on disk and transferred to the permanent storage.

2.4.2 Trigger

The NA62 experiment adopts a trigger strategy based on three stages: a hardware level trigger (L0) and two software implemented in the data flow within the PC Farm (L1 and L2).

Hardware Trigger: L0

The event selection at the lowest trigger level is performed by a central processor, the L0 trigger processor (L0TP), based on a distributed analysis of the event carried on by six detectors (L0 sources): CHOD, NewCHOD, RICH, LAV12, MUV and LKr. NA62 is the first experiment in high energy particle physics to employ a system for data acquisition and triggering that shares the very same data already at the hardware trigger level.

The readout boards of each L0 source verify the correspondence of the acquired data to interesting patterns and encode the time and the matching event topology in a 64 bits long trigger word (primitive, later referred also as trigger signals). The primitives are sent to the L0TP via a Gigabit Ethernet connection in packets using the UDP standard.

Inside the trigger processor the primitives from the various sources are combined, if within a programmable time window with respect to the time of the reference trigger signal – which in the first running period of NA62 (2015-2018) comes from the RICH – and compared with a set of up to 31 interesting event configurations (trigger masks) to generate a L0 trigger for the physics analysis. The L0TP is able to generate, in parallel with the physics data taking, triggers based on the primitives sent by a single detector, independently from the chosen reference source. These triggers are called Control Triggers because they allow to directly monitor the trigger operation and performance. After each L0 trigger, the L0TP sends a copy of the primitives to the PC Farm, which are then stored in the data. This mechanism allows a precise determination of the efficiency for each element involved in the trigger. Calibration and periodic triggers are also acquired along with the normal data acquisition, providing a tool to monitor the detector response before, during and after the beam extraction.

Software Triggers: L1 and L2

When a L0 trigger is issued, all detectors, but the calorimeters and the GTK, send the event data to the computers of the PC Farm. By design, the L0 trigger rate can be up to 1 MHz, resulting in about 1 ms processing time available for the event selection at L1. In order to comply the tight timing requirement, the L1 trigger elaborates only a restricted set of informations. The first stage of the event selection analyses single detector information, extending the trigger selection performed at L0 with the detectors not involved at the hardware level (i.e. the kaon identification with the KTAG). The L1 trigger is required to reduce the accepted event rate below the 100 kHz limit imposed by the network bandwidth of the GTK and calorimeters readout.

At the second level of software trigger a partial reconstruction of the event can be performed, exploiting also the results of the previous selection stage. The L2 trigger architecture allows a selection of high level event variables like the position of the closest distance of approach between a STRAW and a GTK track. The L2 trigger is expected to reduce the data rate by a factor 10, below 10 kHz, matching the transfer data rate to the permanent tape storage. However, the optimization and the technological improvement of the data transfer system allowed to acquire data in the first phase of NA62 (2015-2018) with the L2 trigger stage disabled.

The selection algorithms employed at the software level of the trigger, can be run in two different modes: flagging and cutting. In flagging mode the response of the algorithm is stored, but not considered in the selection process. In the cutting configuration, instead, the response is enforced. The L1 and L2 algorithms are always run in flagging mode for events triggered by the control trigger line.

The selection requirements of the software triggers can be set independently for each L0 trigger mask, allowing the acquisition of data for very different studies. A programmable fraction of events is processed by the L1 and by the L2 in flagging mode to generate a sample of data for the determination of the trigger efficiency.

2.5 NA62 Software Framework

The data collected by the NA62 apparatus are written in plain binary files – usually referred as raw-files – of about 4 GB size per burst. The raw-files encode the response of each detector recorded by the readout boards.

The NA62 collaboration has developed an integrated software framework, NA62FW [26], that provides a common environment for raw data decoding and reconstruction, event simulations, and data analysis.

The framework is implemented in the C++ standard, with some Fortran routines imported from the NA48 software, and consists of three modules:

- **NA62MC:** this module is dedicated to the production of simulated events. Configuration files allow to define the beam shape and the decay mode.

- **NA62Reconstruction:** the reconstruction of collected and simulated events is performed by the NA62Reconstruction module. A raw-file contains basic information about the signal in the detector. In the reconstruction the event information are decoded and stored in simple objects, called hits, indicating

for example the time, the amplitude, and the channel of a pulse. Hits are then grouped into complex objects, the candidates, providing higher level information like tracks in the spectrometer or clusters in the calorimeters.
The Monte Carlo simulation files generated by the NA62MC module contain the physic signals generated in the detectors like energy deposits or produced photons. The first stage of the reconstruction procedure, in this case, emulates the response of the readout electronics to the simulated signals, generating the hits. The hits from the simulation are then grouped in candidates, using the same code as for the acquired data.

- **NA62Analysis:** the analysis module provides a direct and flexible tool to access the information of reconstructed events. NA62Analysis is composed by a central manager executing low level data access operations as well as event consistency checks, and accessory tools implemented to simplify the user operations. The actual analysis code is written in template classes, named Analyzers.

2.5.1 Monte Carlo Simulation

The NA62MC component of the framework is dedicated to the generation of simulated events. The simulation of the kaon beam line starts just before the KTAG detector and makes use of the TURTLE [27] – Trace Unlimited Rays Through Lumped Elements – software package. The beam parameters are supposed to be tuned on a run-by-run basis, even though at the moment the simulation is calibrated on one reference run per year of data taking.
The description of the NA62 apparatus is achieved by the Geant 4 [28] software framework developed by CERN. This software package provides an accurate simulation of particle propagation and interaction with matter. The Geant software is also capable to manage the decay of unstable particles, according to their life time and boost, however in NA62MC this function is enabled only for secondary particles (those generated by the beam). The decay of the beam particles is, instead, managed by internal generators partly inherited from the NA48 experiment. These generators implement the simulation of beam particle decays (mainly kaon decays) at rest, boosting then the event according to the generated beam particle momentum into the laboratory frame.
NA62MC stores the information about the physical signals produced in the apparatus (like energy deposits or Cherenkov light) in output files, processed later by NA62Reconstruction.

The work presented in this document analysed Monte Carlo (MC) samples produced centrally by the NA62 collaboration using NA62FW revisions v0.11.0 and v0.11.1. The decay generators used to produce the analysed MC samples are based on [29] and [30].

Chapter 3

Calorimeters

An efficient particle identification through the precise measurement of shower shapes and energy deposits in calorimeters is a strict requirement for the NA62 experiment. The electromagnetic calorimeter (LKr), inherited from NA48, provides the measurement of electromagnetic showers (i.e. electrons or photons), while the hadron calorimeter (HAC) complements the information for hadronic cascades.

3.1 LKr Calorimeter

The electromagnetic calorimeter, in jargon LKr, is an homogeneous calorimeter filled with about 9000 liters of liquefied krypton kept at a temperature of 121 K.

The sensitive volume of the detector has the shape of an octagonal tower with an apothem of 93 cm and a depth of 127 cm, equivalent to 27 radiation lengths. Therefore, at the NA62 beam energies, the calorimeter ensures the containment of more than 99% of an electromagnetic shower.

The active volume of the calorimeter is subdivided in 13248 ($2 \times 2 \times 127$ cm^3) double ionization cells with a central anode as charge collector (Figure 3.1). Cathodes and anodes are made of thin Cu-Be ribbons almost aligned with the beam axis and with a zig-zag shape, in order to minimize the response dependence on the particle impact position. A 3 kV bias voltage is applied to the electrodes, making each cell work as an ionization chamber.

The signal generated by a particle crossing the detector is amplified and shaped by pre-amplifiers placed inside the cryostat. Immediately outside the detector, the pulse is converted into a differential signal and further shaped by transceiver boards, in order to be transferred, without distortions, to the readout.

The energy resolution of the LKr calorimeter for electromagnetic showers, namely electrons and photons, was measured during the NA48 experiment [31] as

$$\frac{\sigma_E}{E} = \frac{0.032}{\sqrt{E\ [\text{GeV}]}} \oplus \frac{0.09}{E\ [\text{GeV}]} \oplus 0.0042 \tag{3.1}$$

The data collected during the 2015 data taking have shown that the LKr performance are slightly worse in NA62, most probably because of missing fine calibrations and of the different readout electronics, leading to [21]:

$$\frac{\sigma_E}{E} = \frac{0.048}{\sqrt{E\ [\text{GeV}]}} \oplus \frac{0.11}{E\ [\text{GeV}]} \oplus 0.009 \tag{3.2}$$

Beside the particle identification, the LKr is also an indispensable element of the photon veto system. In a large majority of $K^+ \to \pi^+\pi^0\,(\to \gamma\gamma)$ events, at least one of the photons hits the calorimeter. The LKr photon detection inefficiency was measured, with NA48 2004 and 2006 data, to be better than 1×10^{-5} for photon energies above 10 GeV [32].

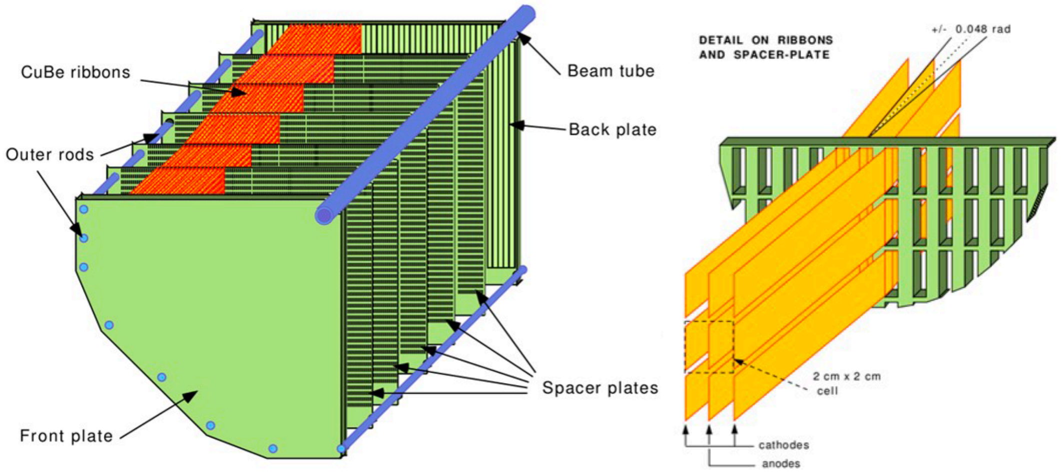

Figure 3.1 – On the left schematic view of a quadrant of the LKr calorimeter active volume. On the right the layout of a double ionization cell structure [21].

3.1.1 Calorimeter Signal Readout

The digitization of the calorimeter signals is performed using so-called CREAM (Calorimeter REAdout Module [33]) boards, which were developed in collaboration between NA62 and the CAEN company and provide a continuous 40 MHz digitization of the signals from 32 input channels. The signal from each input channel is preprocessed to have a pseudo-gaussian shape and then digitized by a flash ADC with a dynamic range of 2 V and 14 bits resolution (125 µV per ADC count). The baseline can be adjusted, singularly for each channel, with a digital to analog converter (DAC) connected to the entrance of the ADC.

The digitized samples are stored in an on-board memory and sent to the PC Farm for the events passing the first two trigger levels (L0 and L1). In normal operation a zero-suppression algorithm, requiring a pulse amplitude (difference between largest and smallest samples) of at least 20 ADC counts, is applied in order to reduce the bandwidth.

The reconstruction of clusters for the L0 trigger is performed in a central system, LKr L0, collecting the information from all the CREAMs. The bandwidth required for the transmission to the LKr L0 of the samples of each single channel is not feasible for NA62 (about 18 Gb/s per module). Hence, the samples collected in a CREAM are summed, after removing the pedestal, in two 16 bits values for transmission to the trigger system.

3.1.2 Signal and Cluster Reconstruction

The reconstruction algorithm for the LKr calorimeter signals was inherited from the NA48 software. The energy and time of a pulse is obtained using a digital filter, where the digitized signal is compared with a reference pulse. Special runs, without beam, are dedicated to the calibration of the LKr cell responses using an internal, precisely calibrated, charge injection system. This allows building a template of the pulse shape for different values of the injected charge, which is then used to determine the parameters of the digital filter method.

All the cells with a reconstructed energy of at least 250 MeV are marked as possible seeds for the cluster construction. Starting from the most energetic seed candidate, a cluster is defined if it is a local maximum (it has a larger energy deposit with respect to the neighbouring cells) and if its energy is larger than 1.8 times the mean energy of the neighbouring cells.

The energy of each cluster is then defined as the sum of all the cells within 11 cm from the seed, weighted by the possible overlap between different cascades (in the assumption of an electromagnetic shower shape).

3.2 Hadron Calorimeter

The hadron calorimeter, HAC, is a sampling calorimeter counting about 10 interaction lengths, subdivided in two separated modulesz. Since the hadron calorimeter takes part to the Muon Veto system (MUVs), as shown in Figure 3.2, its modules are usually referred as MUV1, in front, and MUV2, in the back. The two detectors consist of iron-scintillator sandwich calorimeters. The active planes are composed by long scintillator strips alternately oriented horizontally and vertically. In each module, the light collected by scintillators covering the same area is conveyed to the same photomultiplier.

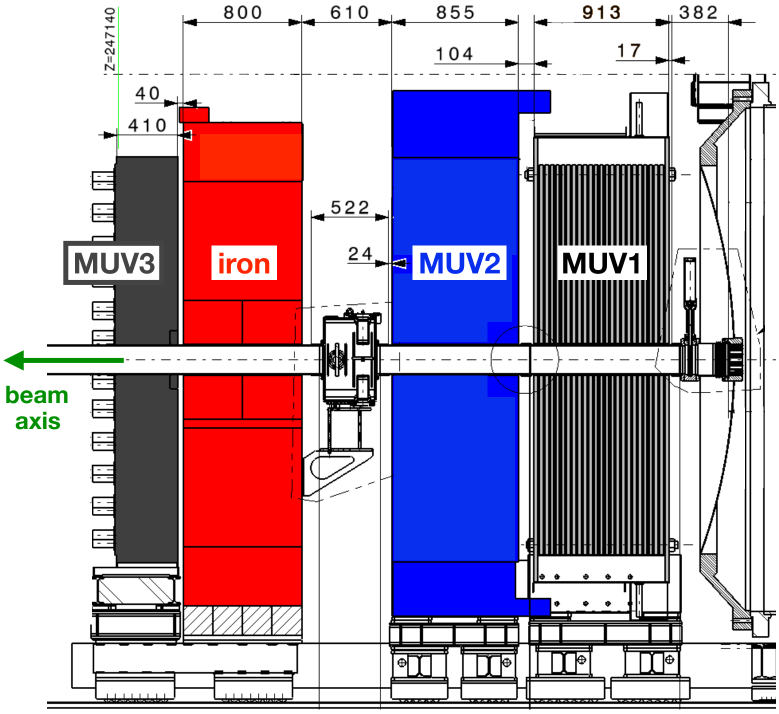

Figure 3.2 – Schematic of the NA62 muon veto system [21].

3.2.1 Front Module - MUV1

The front module of the hadron calorimeter consists of 24 iron plates of 2.7 cm thickness interleaved with 23 layers of 0.9 cm thick scintillator strips. Each active layer is composed of 44 scintillators 6 cm wide and spanning the whole detector length. The innermost scintillators, 8 in the horizontal and 10 in the vertical plane, are divided in two parts, each spanning (up to) half of the detector length, in order to accommodate the higher rate and the beam tube. A sketch of a MUV1 scintillator layer is shown on the left of Figure 3.3.

Two wavelength-shifting fibers (WLS), glued inside the strips, perform the light collection and transmission to photomultipliers on both sides of the scintillator. For shorter strips the light readout is performed only on the outer side, while on the inner end reflective foils are glued on the fibers. In order to minimize the light losses, each scintillator is wrapped in aluminised mylar foils.

The MUV1 thickness is determined by 24 × 2.7 cm of iron and 23 × 0.9 cm of scintillator, thus meaning 4.1 interaction lengths λ_i. The sampling fraction is a calorimetric parameter which describes, in first approximation, the fraction of the energy deposited in the active material respect to the total energy release in the calorimeter. It is defined as the ratio between the active and total material in the calorimeter. The MUV1 sampling fraction – neglecting the last iron plate which is not followed by an active layer – is provided by 23×0.9 cm $\times$ 1.06 g/cm^3 of active material and 23×2.7 cm $\times$ 7.784 g/cm^3 of iron, leading to a value of 4.34%.

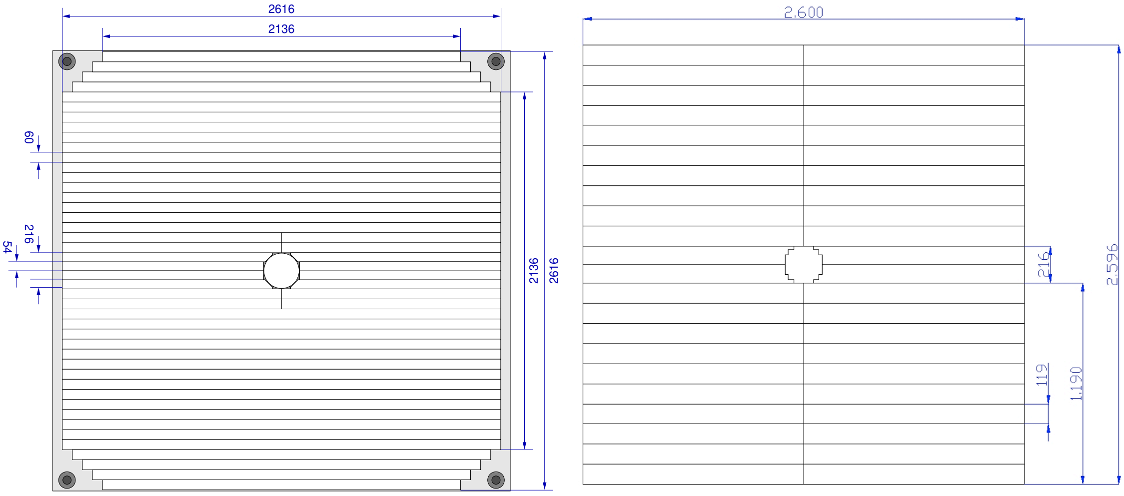

Figure 3.3 – Sketch of a horizontal scintillator layer: on the left for the MUV1 [34], on the right for the MUV2 [20].

3.2.2 Back Module - MUV2

The MUV2 is the former front module of the NA48 hadron calorimeter [31]. This section of the calorimeter counts as many iron plates (24) as scintillator layers, with a thin aluminium foil as support structure of the first active plane in the original configuration. The module was starting with a scintillator layer which allowed to detect the tails of showers starting in the electromagnetic calorimeter. However, because of the tighter space constraints in the new NA62 apparatus, the detector has been turned by 180°, leading to a configuration with two consecutive absorber

plates: the last and the first respectively of the front and the back module.
An active layer of the MUV2 (on the right of Figure 3.3) counts 2 × 22 (0.45 cm thick) scintillating strips spanning half of the detector size and providing a transverse segmentation of 12 cm. Light guides, directly attached to the scintillators, convey the scintillation light produced in the strips covering the same area to the respective photomultiplier.
The back module accounts for $3.7\lambda_i$, resulting in 7.8 interaction lengths for the complete calorimeter. The sampling fraction, including the last iron layer of the MUV1, is provided by 24×0.45 cm $\times$ 1.032 g/cm^3 of active material and (24×2.5 cm + 2.7 cm) $\times$ 7.784 g/cm^3 of iron, leading to a value of 2.23%.

3.2.3 Pulse Reconstruction

The hadron calorimeter employs the same readout boards as the LKr. Photomultiplier signals are routed to shaper modules, refurbished from the NA48 HAC readout, converting the fast (10 ns to 20 ns wide) pulses into a LKr-like differential signal. The output of two shaper modules (16 channels each) is then connected to one CREAM board.
A stream of 10 ADC samples per channel is sent to the storage for each event passing the L0 and L1 trigger conditions. At the beginning of the 2016 data taking 12 samples were requested, but instabilities in the data acquisition suggested the reduction to 10. The pulse shape is a slightly asymmetric gaussian, with a width at half maximum of about 1.2 clock cycles (about 30 ns), followed by a small, but long undershoot.
The reconstruction of the pulse information consists of two elements: the peak finding algorithm and the pulse fitting.

Peak Finding Algorithm

Within the acquisition window of one event several pulses may be recorded, a peak finding algorithm is therefore employed to identify signal candidates. As first, the algorithm performs an estimate of the event baseline as the mean of all the samples compatible with a constant shape. This is obtained requiring half the difference between the amplitudes of the previous and of the following samples below 5 ADC counts. In case less than 5 samples satisfy the requirement for the baseline evaluation, the absolute minimum of the recorded stream is used as pedestal value.
Pulse candidates are then defined as local maxima having an amplitude of at least

20 ADC counts with respect to the estimated baseline or a difference between two samples before the maximum of at least 20 ADC counts. The amplitude requirements allow to reject most of the pulses originating from noise or cross talk, which would significantly increase the signal processing time.

Pulse Fitting

The pulse parameters (amplitude and time) are obtained by fitting the collected samples with a template function using the MINUIT minimization routine [35].
The template function has been defined by studying muon and pion signals, acquired with a stream of 32 samples, and differs for isolated and overlapping pulses.
In case the found signal candidate is isolated (namely at least 8 samples away from any other pulse), the sum of a constant (for the baseline) and a gaussian (for the signal) is used as template function describing the pulse. The fit range is adjusted to have, if possible, at least two baseline samples before the pulse and only two points after the local maximum as shown in Figure 3.4.

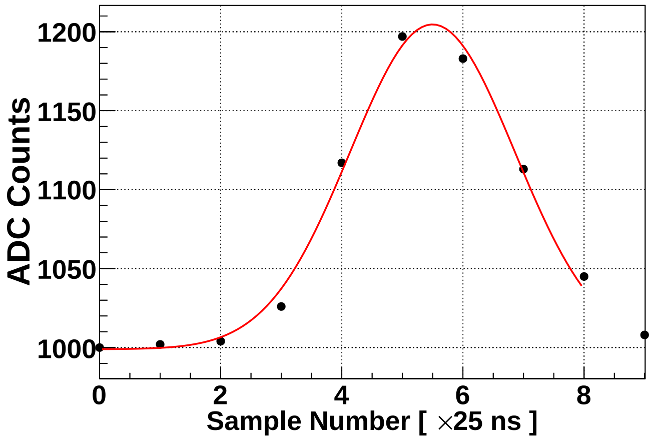

Figure 3.4 – Example of an isolated pulse signal reconstruction: CREAM samples (black) and result of the fitting algorithm (red).

When two pulses are found closer than 8 samples, the signals are combined in a single template function in the form: constant (baseline) plus two gaussians (the two pulses). The fit range attempts to accommodate at least 2 baseline points before the first pulse and two samples after the second peak. An example of a MUV1 signal containing two pulses is shown in Figure 3.5 with the result of the pulse fitting algorithm.
The charge of a reconstructed pulse is determined as the integral of the fitted gaus-

sian, which is provided by the simple formula shown in Equation 3.3, with A and σ the amplitude (converted in mV) and the width (converted in ns) of the gaussian respectively.

$$Q[pC] = \sqrt{\pi} \times A[\mathrm{mV}] \times \sigma[\mathrm{ns}] \tag{3.3}$$

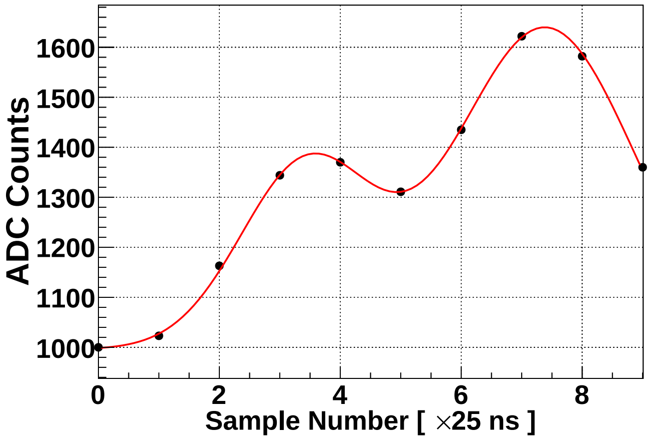

Figure 3.5 – Example of a two pulses signal reconstruction: CREAM samples (black) and result of the fitting algorithm (red).

3.3 Track Seeded Clustering

The NA62Reconstruction module does not provide an optimal environment for the reconstruction of hadron cascades. At this stage it is not allowed to combine the information from different detectors and, therefore, also MUV1 and MUV2 are to be treated separately and no external input can be used in the cluster reconstruction (like the STRAW tracks).

The `SpectrometerCalorimetersAssociation` tool [26] is an analysis code (Analyzer) intended to exploit the full potential of the calorimeters by:

- matching charged particle tracks reconstructed in the spectrometer with the energy deposits in the electromagnetic and hadronic calorimeters.
- applying all the needed energy calibrations, as obtained in Chapter 5.
- providing a particle identification response based on the Boosted Decision Trees algorithm described in Chapter 7.

3.3.1 LKr matching

The STRAW spectrometer provides excellent spatial extrapolation to the LKr, but poor timing information – the spectrometer time resolution is about 5 ns. The tracks are associated to reconstructed LKr clusters by minimizing a discriminant which combines the distance between the track extrapolation and the cluster position and the time difference:

$$D = \sqrt{\frac{(\vec{x}_{track} - \vec{x}_{LKr})^2}{2 \times 2 \text{ cm}^2} + \frac{(t_{track} - t_{LKr})^2}{5 \times 5 \text{ ns}^2}} \tag{3.4}$$

The selected cluster is then required to be within 6 cm from the track extrapolation and 15 ns from the track time.

The LKr reconstruction is optimized for electromagnetic showers and shows therefore considerable inefficiency for energy deposits related to ionization and hadron cascades. When a match with a standard cluster – a cluster built by the reconstruction software – is not found, a track seeded clustering approach is followed. The in-time cell (within 25 ns from the track time) with the largest energy deposit in a circle of 6 cm from the track extrapolation is used as seed to reconstruct the cluster. All the cells within 11 cm and 15 ns from the seed are assigned to the cluster, taking into account possible energy sharing effects with nearby clusters.

3.3.2 HAC cluster reconstruction

The reconstruction of clusters in the hadron calorimeter uses as initial information the extrapolated track impact position at the front module (MUV1) and the time of the LKr energy deposit. The algorithm consists of two steps: at first it computes the shower information in the MUV1, then includes the signals from the MUV2.

MUV1

The reconstruction of a MUV1 cluster starts with the definition of a seed hit for the two calorimeter views (horizontally and vertically oriented scintillator planes). A seed is defined as the channel with the largest energy deposit in time with the track (within 7 ns from the LKr time) and less than 30 cm from the expected track impact point.

In order to reconstruct the cluster, only energy deposits within 10 ns from the seed time are considered. The cluster is then defined as a box of 66×66 cm^2 centered on the seeds, corresponding to about 3 interaction lengths in iron on each side of the seeds. However if two consecutive channels are missing, the cluster is made smaller. The energy collected in a long scintillator is readout by two photomultipliers at both the ends of the strips. When computing the cluster energy and time, this additional information is used by performing the mean of the charge and time measurements, corrected for the expected shower position. The central region of the detector is equipped with scintillators which span half of the module length, are placed back-to-back, and are readout on the outer side. The energy of showers developing nearby the center of the calorimeter is hence collected by the two half strips. In order to take into account this effect, the energy measured by both the channels is summed up when the seed on the perpendicular view is found less than 30 cm from the cut point of these scintillators. The correction of the collected charge for the signal attenuation is performed considering the expected shower position for the channels on the side where the center of the cascade sits, and 6 cm away from the strip end on the other readout. The 6 cm margin from the center of the detector is used to avoid a possible over-correction of the energy deposit.

MUV2

The cluster obtained in the MUV1 is used as seed for the MUV2 reconstruction. A global distribution of the HAC channel energies is built from the in-time charge collected by channels in the front and back module covering the same area. The in-time condition for MUV1 is defined at the previous reconstruction step, while for the MUV2 hits the requirement is ±5 ns from the LKr cluster time: the single hit time resolution of the MUV2 is considerably better than that of the MUV1. The cluster seeds are than redefined as the most energetic HAC channels in vertically and horizontally oriented planes. The cluster limits are extended until an empty channel (as response of two MUV1 plus one MUV2 channels) is found or the distance to the center of the seed exceeds 40 cm.

The scintillators installed in the MUV2 span only half of the detector. In order to reconstruct correctly the energy deposited by cascades extending over the two halves of the detector, the information from scintillators on both sides are considered. The energy collected by the channel on the side of the center of the shower is corrected for the expected cluster position. The energy recorded on the opposite side is corrected assuming the inner end of the scintillator as light production position.

Algorithm Issues and Improvements

The algorithm for the HAC cluster reconstruction faces two major difficulties:

- a cluster is built only if associated to a track. Therefore particles leaving the beam tube after the spectrometer and generating a shower in the calorimeter are not reconstructed.
- in a multi-track event, like for example $K^+ \to \pi^+\pi^+\pi^-$, the superposition – and therefore the energy sharing – of the different cascades is not taken into account in the cluster building.

There is a common underlying problem related to these issues. In absence of an external input, it is extremely difficult to distinguish between clusters originating from real cascades or due to erroneous combination of hits. The definition of a discriminant, based on internal information like timing, charge asymmetry between the different scintillator orientations, and similar may provide a good handle of this problem. However, the treatment of the electronic signals from the HAC photomultipliers, with a LKr-like shaping, significantly reduces the timing capability and the double pulse resolution of the detector. Once real clusters are defined, a set of pion shower templates may be used to correct for the energy sharing in the overlapping region by exploiting the cascade developments far from that zone.

The main analysis of NA62, the $K^+ \to \pi^+\nu\bar{\nu}$ branching ratio measurement, expect a single isolated track and therefore the present clustering procedure fulfils the analysis requirements.

Chapter 4

The 2016 Data Taking

The NA62 experiment takes data from 2014 until end of 2018 and is currently waiting for the approval for running additional two years (2021 and 2022) after the long shutdown 2 of the CERN accelerator complex. The run periods in 2014 and 2015 were used to perform the commissioning of the detector, the trigger, and the data acquisition system.

The data taking in 2016 allowed to collect a first sample of high quality data for the main analysis. The 2016 run period extended for more than 6 months, from beginning of May until end of November. The first half of this period, until September has been dedicated to the final commissioning of the GTK readout, the LKr level zero trigger (LKr L0), and of the software L1 trigger. In the meanwhile physics quality data has been collected for complementary analyses like the measurement of $K^+ \to \pi^+\gamma\gamma$, the searches for lepton flavour violating processes (i.e. $K^+ \to \pi^-\mu^+\mu^+$) and heavy neutral leptons (in $K^+ \to l^+X$ with $l = \mu, e$).

During the second half of the run period, the NA62 apparatus was ready to acquire data for the $K^+ \to \pi^+\nu\bar{\nu}$ measurement. The analysis of this dataset proved the validity of the decay-in-flight technique and lead to the observation of a first signal event [19].

4.1 Beam Intensity

In a collider environment, like LHC, the protons are densely packed in well separated bunches in order to maximize the collision probability. In a fixed target experiment, instead, it is preferable to have a large amount of protons impinging the target spread over a larger time window. The technique to extract protons from the accelerator is commonly known as slow extraction, and allows to have homogeneous data taking conditions along the spill (an extraction, also referred later as a burst) and a lower instantaneous intensity. The NA62 beam line is expected to receive a 4.8 s long spill containing 33×10^{11} protons, with 3.3 s in a flat beam intensity condition (about 11×10^{11} protons/s).

During the 2016 data taking the beam extracted from the SPS was showing large intensity fluctuations (up to several times the mean value), leading to breakdowns of the data acquisition system. The data taking was therefore stabilized by reducing the amount of protons extracted per spill to about 40% of the nominal intensity (circa 13×10^{11} proton per spill).

4.2 Trigger Configuration

The flexibility of the NA62 trigger system allows to define – and refine – different streams already at the lower level. During the 2016 run period this feature was used to achieve the most convenient trigger configuration for the $K^+ \to \pi^+\nu\bar{\nu}$ measurement.

In the following the trigger configurations used in 2016 are reviewed for both the hardware (L0) and the software (L1) trigger stages.

4.2.1 L0 Trigger Conditions

During the 2016 data taking, the L0 trigger processor (L0TP) allowed the simultaneous acquisition of up to 8 physics data streams (usually referred as trigger masks) and one minimum bias trigger line defined as control trigger.

The physics trigger masks are defined combining the requirements on various detectors, starting from a commonly required trigger source, the reference detector, which during the 2016 - 2018 data taking periods was the RICH. The reference detector defines the L0 trigger time, which is then also used as reference time by the L1 trigger.

Detailed information about the L0 trigger configuration and the performance during the 2016 data taking can be found in [36].

Control Trigger

The control trigger is completely independent from the physics triggers settings. It is defined to be as much as possible an unbiased sample of data, used for example to verify the physics trigger efficiencies and the apparatus performance. A control

trigger is defined as an event with at least two hits in the same quadrant of the CHOD, meaning at least one charged particle crossed the detector. The rate of such events is very large (about 8 MHz in 2016) and therefore a downscaling of 400 – only one event acquired every 400 triggers – was applied.
The data taken with the control trigger are processed by the L1 in the so-called flagging mode: the software trigger algorithms run over these data and the results are stored but not enforced.

RICH L0

The RICH was chosen as reference detector for the physics trigger because of its time resolution, which is about 350 ps at trigger level.
The hits recorded in a time window of about 6 ns by the RICH TDCs are grouped into clusters. If a cluster contains at least 4 hits a trigger is issued.

NewCHOD L0

The NewCHOD L0 trigger allows to select the event topology. All channels providing a signal in a time window of a few nanoseconds are grouped to describe the event on basis of the spatial distribution of the scintillators. In 2016 run the following trigger conditions were used:

- Q1: requires at least one hit in the detector.
- Q2: requires at least two hits in the detector.
- Qx: requires at least two hits from opposite quadrants of the detector.
- UMTC: stands for Upper Threshold Multiplicity Counters, it requires signals from less than 6 scintillators.

MUV3 L0

The MUV3 is used at trigger level both to reject and to select events with muons in the final state. Hence, the algorithm used to generate the trigger does not only verify if there is a signal in the detector, but analyses also the topology of the event. The trigger conditions during the 2016 data taking were:

- MUV3: requires a signal by at least one scintillator.

- MO1: requires a signal from at least one scintillator far from the beam tube (to reduce the contribution from accidentals).
- MO2: requires a hit in at least two separated scintillators far from the beam tube.

LAV L0

The L0 trigger only uses the information from the last station of the large angle vetoes, the LAV12.
The trigger is intended to reject events with a photon in the LAV12. The requirement was to have signals in at least 3 lead glass blocks out of which at least one large is enough to cross the high threshold of the discriminator.

LKr L0

The LKr provides a major contribution to the event selection already at trigger level. The calorimeter can combine spatial and energy information for both neutral and charged particles, resulting in a powerful tool to select the event topology. The trigger requirement of only one cluster and at most 30 GeV of total energy allows to efficiently reject $K_{2\pi}$ events, with only a small acceptance loss for $K^+ \to \pi^+ \nu \bar{\nu}$.
During the 2016 data taking the LKr L0 trigger module was still under commissioning, hence only an upper limit at 20 GeV on the total energy was required. Debugging information, like the number of clusters and the collected energy, has been stored in the trigger primitive and sent to the L0TP for offline validation of the trigger behavior.
The LKr L0 system aggregates and analyses the information from all the CREAM boards (Section 3.1.1). The trigger receives the ADC samples digitized by groups of 4×4 cells, the so-called supercells. Following an improvement in the data transmission, the encoding of the samples sent by the CREAMs to the trigger was changed in 2016 – with respect to the 2015 commissioning run – to allow a 56 MeV resolution on the supercell energy. However this data format modification was not correctly propagated to the trigger algorithm devoted to the determination of pulse time, thus resulting in a corruption for supercells collecting an energy larger than 14 GeV ($2^8 \times 56$ MeV). The simulation of the effect of the mismatch in the data format is not easily reproducible without a deep knowledge of the firmware implementation. However, in a first order approximation the problem can be treated like a time overwriting problem. The probability that a supercell with more than 14 GeV is shifted out of the clustering time window would therefore be 50%, in the assumption only

one bit is affected: in half of the cases the overwritten value matches the original, in the other half instead it does not. This simulation of the trigger response, however, does not provide a good description of the data as will be shown later in Figure 6.18 (Chapter 6).

4.2.2 Software Trigger (L1) Conditions

The software trigger plays a crucial role in the online event selection. During the 2016 data taking the rate of events passing the hardware trigger was at the level of 435 kHz, but due to bandwidth limitations the CREAM boards and the GTK readout cannot send data to the PC Farm at a rate higher than 100 kHz.
Three algorithms have been implemented for the L1 trigger during 2016 based on the information of KTAG, LAV and STRAW. Depending on the L0 stream that triggered the events, the L1 algorithms are applied positively – the requirements must be fulfilled –, negatively – as a veto – or just in flagging mode.

KTAG L1

A very effective and minimally biassing constraint is the identification of an in-time beam kaon in the event. This requirement is implemented in the L1 KTAG algorithm. The data from the KTAG are scanned and a positive response is issued if a signal, within 5 ns from the trigger time, is found in at least 4 sectors.

LAV L1

A large fraction of kaon decays involves photons. A good photon rejection at trigger level therefore allows to reduce significantly the bandwidth requirements. At L0 level only the last station of the LAV is included, the L1 algorithm extends the veto on large angle veto signals to all the stations. The algorithm provides a positive response if at least 3 hits in the LAV (the sum over all the stations) are found within 10 ns from the trigger time.

STRAW L1

The STRAW L1 algorithm provides an online reconstruction and selection of the tracks. Reconstructed tracks are verified to fulfil minimal quality requirements:

- the position of closest distance of approach (CDA) with respect to the beam axis is in an extended fiducial region: z-coordinate in $[-100, 180]$ m.
- the CDA of the vertex is smaller than 20 cm.
- the track momentum is below 50 GeV/c to reject beam pions which are scattered on the last GTK station.

The algorithm provides two different responses:

- STRAW$_{pnn}$ for the $K^+ \to \pi^+\nu\bar{\nu}$ measurement. It is positive if at least one positive track is reconstructed and passes the selection criteria.
- STRAW$_{exotics}$ for multi-track events. It is positive if at least a negative track is reconstructed and passes the selection criteria.

4.3 Trigger Streams

The previously described trigger conditions have been combined during the 2016 $K^+ \to \pi^+\nu\bar{\nu}$ period of data taking in 8 data streams, as shown in Table 4.1, to allow the simultaneous collection of data for several analysis.

Name	**L0 Conditions**	**D**	**L1 Conditions**
Control	Control	400	
Mask 0	RICH × Q1 × !MUV3	200	KTAG
Mask 1	RICH × !Qx × UMTC × !MUV3 × !LAV × !LKr	1	KTAG × !LAV × STRAW$_{pnn}$
Mask 2	RICH × Q2 × MO2 × !LKr	1	STRAW$_{exotics}$
Mask 3	RICH × QX × MO1	5	KTAG × !LAV × STRAW$_{exotics}$
Mask 4	RICH × QX × LKr	2	!LAV × STRAW$_{exotics}$
Mask 5	RICH × QX	50	KTAG × !LAV × STRAW$_{exotics}$
Mask 6	RICH × QX × MO2 × !LKr	1	KTAG × !LAV × STRAW$_{exotics}$

Table 4.1 – L0 and L1 trigger configurations with the corresponding L0 downscaling (D) in the 2016 data taking.

Control Trigger Data taken with the control trigger allow to perform studies on detector performance, trigger efficiency, etc in a minimum bias sample. The $K^+ \to \pi^+\nu\bar{\nu}$ and other analyses use the control trigger to select normalization samples.

Mask 0 The mask 0 data stream provides a minimum bias sample for kaon decays without muons in the final state for analyses of $K^+ \to \pi^+\gamma\gamma$, $K^+ \to e^+\nu\gamma$ or the search for heavy neutral leptons in $K^+ \to l^+X$ (with $l = e, \mu$) decays.

Mask 1 This trigger configuration is devoted to the collection of data for the $K^+ \to \pi^+\nu\bar{\nu}$ analysis. The analysis of 2016 data has allowed the observation of a first signal candidate from the $K^+ \to \pi^+\nu\bar{\nu}$ decay [19]. Other interesting analyses using this dataset are the searches for the so-called dark photons [37] and for neutral pion into invisible decay [38].

Masks 2 and 6 The data from these trigger lines contain mostly events with two muons in the final state. These datasets are dedicated to the measurement of the $K \to \pi\mu\mu$ processes, both in the Standard Model ($K^+ \to \pi^+\mu^-\mu^+$) and in the lepton number violating ($K^+ \to \pi^-\mu^+\mu^+$) mode. Moreover, the absence of the kaon identification at trigger level (Mask 2) allows also to exploit this data for the search of long-lived particles produced in the beryllium target and decaying into a $\mu^+\mu^-$ pair inside the fiducial region [22].

Mask 3 and Mask 4 These data streams are intended for the search of exotic three-body kaon decays with a muon in the final state like $K^+ \to \pi^+\mu^-e^+$.

Mask 5 This data stream selects kaon decays with a multi-track final state. It provides a control sample of $K^+ \to \pi^+\pi^+\pi^-$ events use, for example, for the calibration of the GTK.

4.4 Data and Processing

The second period of the 2016 data taking, when high quality physics data have been acquired for the $K^+ \to \pi^+\nu\bar{\nu}$ analysis, is usually referred as sample A (or 2016A). The 2016A sample accounts for about 240 TB of raw-files, which translate into approximately 400 TB of reconstructed data. Analysing such a large amount of data requires a considerable amount of time mainly due to I/O operations. In order to optimize the computing resources and obtain shorter turn-around times for the physics analyses, separated streams of data were produced with a pre-selection, a so-called filter, already applied. The size of a filtered data stream is up to $10-20\%$ of the reconstructed data depending on the filter stream and the beam intensity in the considered data.

In this work data from the full reconstruction and from the following two filters have been analysed:

- `FilterPnn:` this filter provides the dataset for the $K^+ \to \pi^+ \nu\bar{\nu}$ measurement. Only events from the control and the mask 1 trigger lines are selected.
  The filter performs a loose selection of single-track events, namely events with a track not-forming a good vertex with any other track. Events collected by the physics trigger (mask 1) are also required not to match any in-time activity in the MUV3, in the LAV, and in the SAV.

- `FilterOneTrackTwoClusters:` this data stream is intended for the selection of $K^+ \to \pi^+\pi^0$ and $K^+ \to \pi^+\gamma\gamma$ decays.
  The filter uses data triggered by the control and the mask 0 triggers, selecting events with a track and two LKr clusters not associated to any track and with a total energy (track momentum plus the two cluster energies) larger than 40 GeV.

Chapter 5

Energy Reconstruction and Calibration in the Hadron Calorimeter

The energy calibration of the hadron calorimeter allows to define an absolute energy scale and to optimize the detector resolution.
Three different sources for corrections can be identified: single channel response equalization, light attenuation in scintillators and fibers, and energy reconstruction.

5.1 Single Channel Response Equalization

The first step of the hadron calorimeter calibration is the definition of the working voltage of each photomultiplier in order to obtain an homogeneous response over the calorimeter surface.
At the beginning of the data taking period, the gain of all the photomultipliers is adjusted by varying the supply voltage. The response of each channel to crossing muons is evaluated in steps of the applied voltage. The range of operation is defined by a coarse scan of the high voltage in steps of 50 V and then refined (20 V steps) around the selected working range as shown in Figure 5.1.
A value of 1500 pC is chosen as charge reference for the MUV1 because it allows a good separation between signal and noise while keeping large energy deposits within the dynamic range of the ADC[1].

---

[1] A muon crossing one module of the HAC deposits an energy of roughly 1 GeV. The signal amplitude for such event is about 30 mV at the 1500 pC point. Hence the dynamic range of a single channel is given by the ADC dynamic range (2 V) divided by the ratio of voltage to energy for muons (0.03 V/GeV), resulting in 67 GeV.

The MUV2 reference value is set to 1000 pC, because the photomultipliers in this module do not allow to reach the value of 1500 pC without approaching the limit of the operating range.

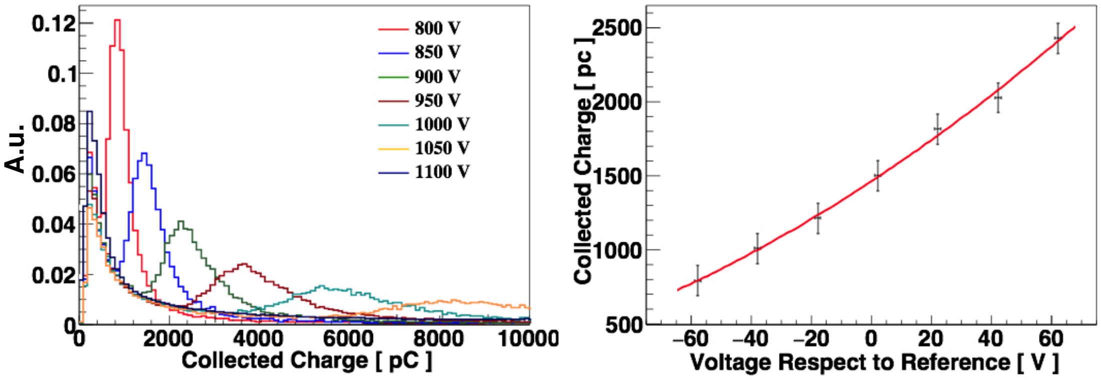

Figure 5.1 – Voltage Scan on the MUV1 detector, coarse on the left and refinement with 20 V steps around the 1500 pC point.

5.2 Light Attenuation and Time Delay along the scintillating strips

The long path which the light has to travel inside scintillators and fibers introduces an attenuation and a delay of the signal that depends on the hit position. A precise determination of the attenuation and delay patterns allows to improve significantly the detector performance.

A long run with muons is performed after the photomultiplier voltages have been adjusted. Events with only one well-reconstructed track in the spectrometer, matching a hit in the CHOD and in the MUV3 and an energy deposit compatible with a minimum ionizing particle in the LKr calorimeter are selected. The impacted scintillators in the HAC are determined by the track extrapolation with a few mm precision. A hit, within 50 ns from the CHOD time, in each of the expected scintillators is required for both MUV1 and MUV2 modules. Moreover the charge collected in this channel should be at least twice as large as the sum of what is collected in the neighboring channels. For each channel the charge and the time difference to the CHOD hit are studied as a function of the impact point along the scintillator.

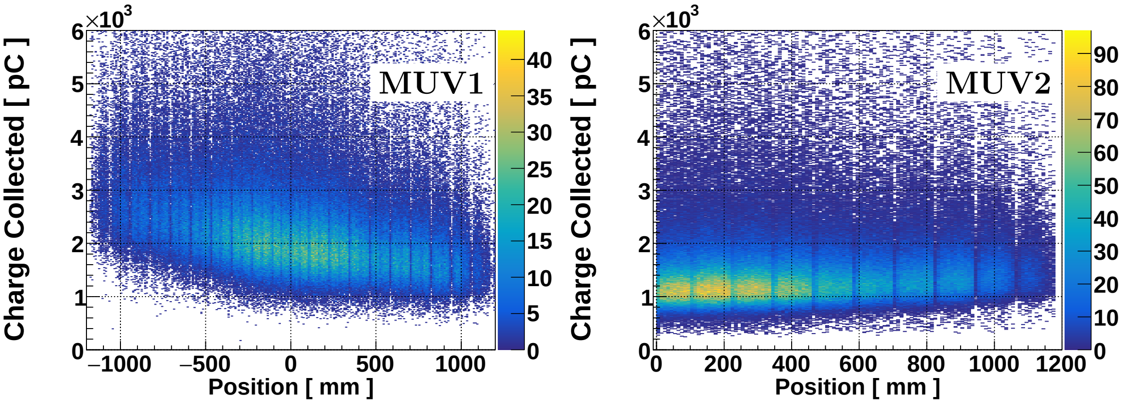

Figure 5.2 – Charge attenuation in MUV1 (left) and MUV2 (right) respectively for channels 115 and 107 (run 3117, August 2016). The positions are defined so that the origin of the axis corresponds to the center of the detector in the direction perpendicular to the scintillator orientation.

5.2.1 Light Attenuation

The charge distribution presented in Figure 5.2, obtained by analysing data from the muon run 3117, are fitted in 3 cm wide slices. A Landau function parameterizes the energy loss by the muon and is then convoluted with a Gaussian centered at zero to introduce the smearing due to the energy resolution of the detector. An example fit is presented in Figure 5.3, where the parameters of the fit are respectively: the normalization (Norm), most probable value (MPV), the sigma of the landau (σ_L), and the width of the gaussian (σ_G).

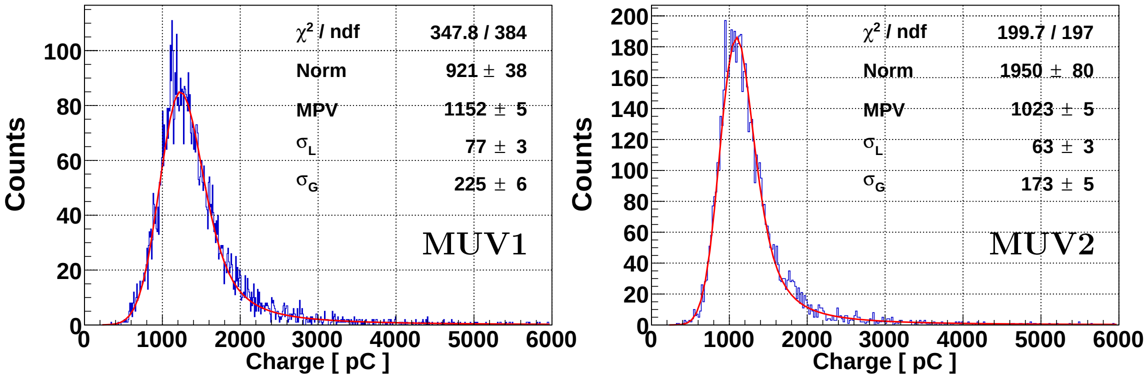

Figure 5.3 – Example of fit for the light attenuation: on the left for MUV1 channel 115, on the right for MUV2 channel 107 (same channels as Figure 5.2).

The MPV of each fitted slice is then plotted against the position to parameterize the dependency. In MUV2 strips the scintillation light reaches, in a first order approximation, the photomultiplier directly or after being reflected by the other end of the strip. The attenuation can therefore be parameterized by

$$A(x) = A_0 \cdot \left((1 - r) \cdot e^{-\frac{x}{\lambda}} + r \cdot e^{-\frac{2L - x}{\lambda}} \right) \tag{5.1}$$

where x is the distance from the instrumented end of the scintillator, L the scintillator length, λ the attenuation length, r the fraction of light reflected and A_0 the produced light intensity. This function provides excellent results in the MUV2 detector (Figure 5.4) thanks to the coupling of scintillator and photomultiplier via light guides.

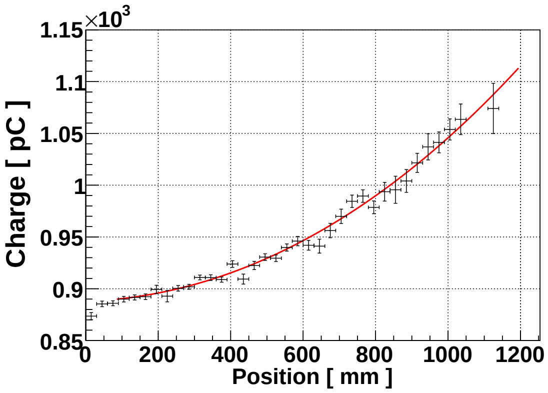

Figure 5.4 – MUV2 attenuation fit for channel 107.

The presence of WLS fibers inside the MUV1 does not allow to directly apply the simplified model of eq 5.1. Most of the light produced inside the scintillators is quickly trapped inside the fibers and propagates towards the ends. The remaining light propagates inside the scintillator and is partly absorbed by the fibers at a later time. The contribution of the light propagating in the scintillator can be assumed to modify the attenuation length λ into two different parameters λ_1 and λ_2. The function therefore becomes:

$$A(x) = A_0 \cdot \left((1 - r) \cdot e^{-\frac{x}{\lambda_1}} + r \cdot e^{-\frac{2L - x}{\lambda_2}} \right) \tag{5.2}$$

Most of the channels fit correctly with Equation 5.2 as shown on the left of Figure 5.5. However, the central scintillators span half of the detector and are read out only on one side. When the particle crosses the strip nearby the edge, part of the light is lost. Therefore a Fermi-Dirac function is added to the attenuation function to take into account the light losses at the edge in the center of the detector (Figure 5.5 right):

$$A(x) = A_0 \cdot \left((1 - r) \cdot e^{-\frac{x}{\lambda_1}} + r \cdot e^{-\frac{2L - x}{\lambda_2}} - \frac{a}{1 + e^{-\frac{x - b}{c}}} \right) \tag{5.3}$$

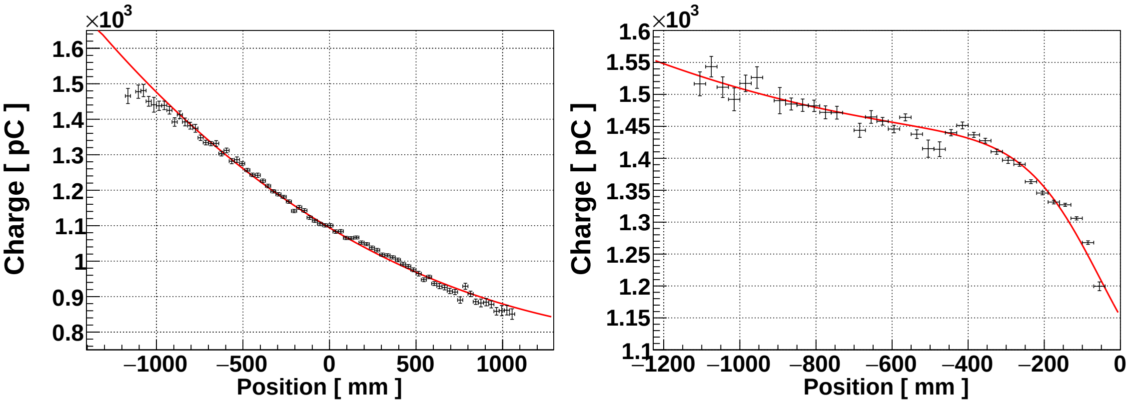

Figure 5.5 – Example of MUV1 channel attenuation fit: on the left for a long scintillator (channel 117, Equation 5.2), on the right for short one (channel 126, Equation 5.3).

The improvement of the detector response can be clearly observed when reconstructing muon showers in the two modules of the hadron calorimeter. The collected charge distribution are presented in Figure 5.6 before and after applying the attenuation correction.

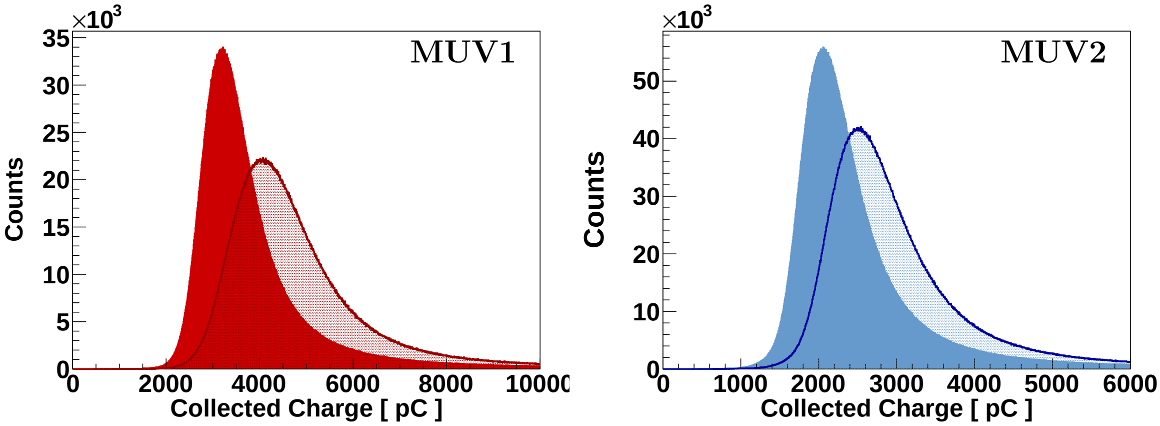

Figure 5.6 – MUV1 and MUV2 response to muons before (solid-line) and after (shaded-line) the attenuation corrections.

5.2.2 Time Delay

A crucial parameter when reconstructing showers in a calorimeter is the timing. The long path which the light has to travel inside the scintillators and fibers introduces a delay in the signal detection which depends on the hit position. The delay is studied in bins of position by considering the time difference between CHOD and the two modules of the hadron calorimeter, assuming the particle to travel with the speed of light.

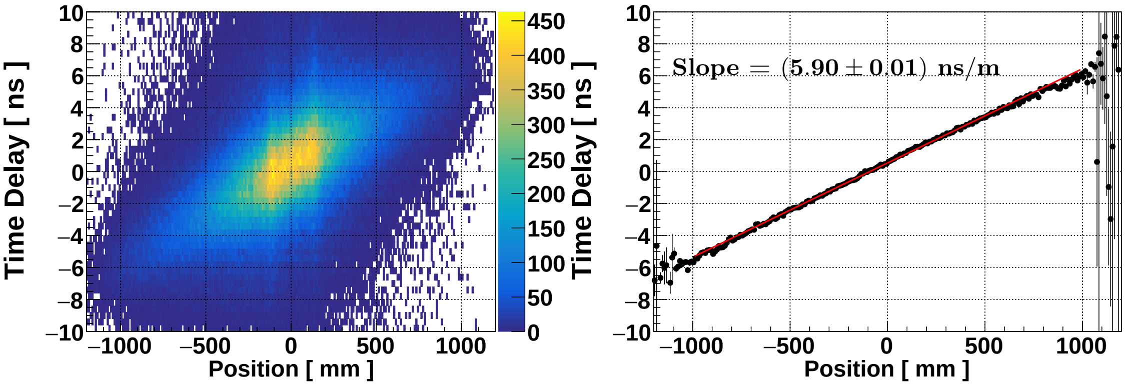

Figure 5.7 – Signal delay with respect to the CHOD as a function of the impact position for channel 128 of the MUV1.

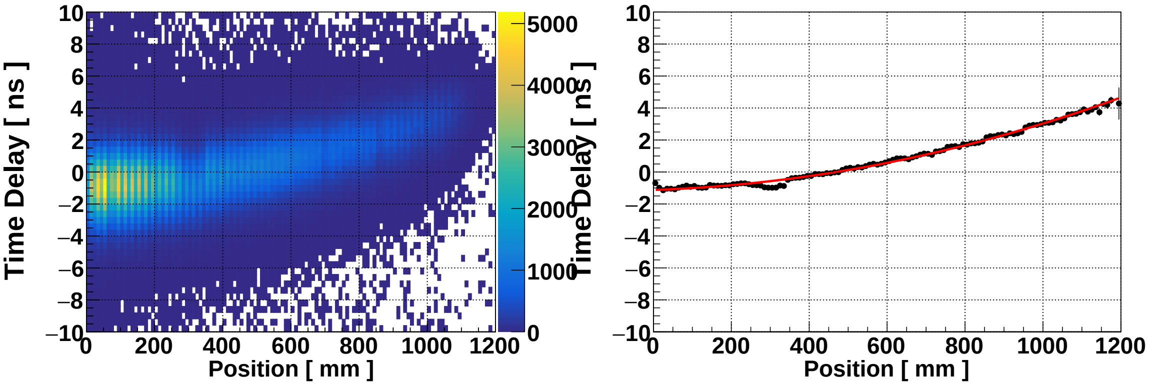

Figure 5.8 – Signal delay with respect to the CHOD as a function of the impact position for channel 160 of the MUV2.

The MUV1 shows a linear dependency (Figure 5.7), the light reaching the photomultiplier travel almost parallel to the fiber therefore the delay is determined simply by the speed of light inside the medium. The MUV2 presents a different behaviour due to the transverse size of the scintillators. The time delay inside the scintillators is parameterized in this case by a second order polynomial as shown in Figure 5.8. The detector time resolutions were evaluated after the corrections with a selection of muons from $K^+ \to \mu^+\nu_\mu$ (as described in 6.2), using the RICH as reference detector. The results are presented in Figure 5.9. The two modules show similar performances in terms of timing with a resolution around 1.6 ns and 1.2 ns respectively for MUV1 and MUV2. The difference is mainly related to the higher light yield provided by the light guide coupling with respect to the fibers light collection.

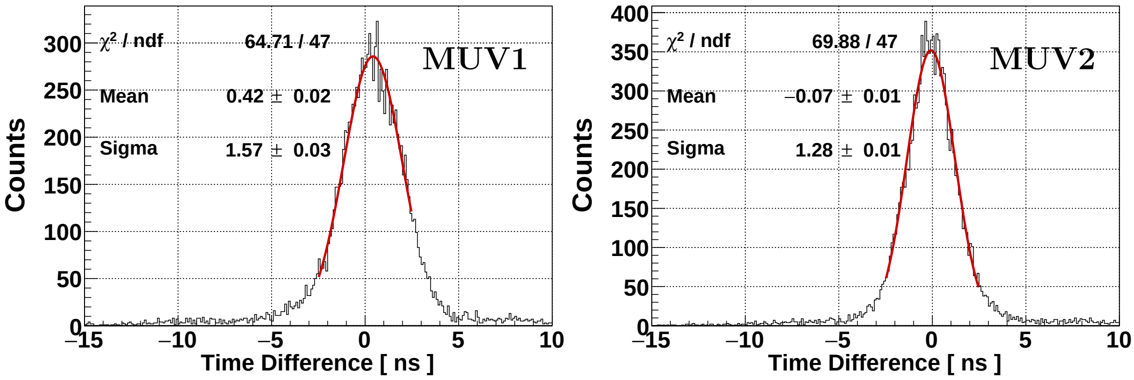

Figure 5.9 – Time resolution for MUV1 and MUV2.

5.3 Energy Reconstruction

The concept of absolute energy calibration is to determine the scaling factor between the measured charge and the energy collected inside the detector.

Showers produced by electrons or photons are very well known and predictable. These particles interact with material electromagnetically by generating bremsstrahlung photons and by conversion into electron-positron pairs, while deep inelastic scattering of electrons on nuclei and photo-nuclear interactions have negligible cross sections. Hadron cascades, on the other hand, are dominated by hadronic and nuclear processes with large fluctuations of particle content inside the shower. The production of secondary particles converts part of the hadron energy to electromagnetically interacting particles, for example π^0s. Hadronic processes and nuclear interactions determine also energy releases which happen at a later time with respect to the main shower development $\mathcal{O}(\mu\mathrm{s})$. This fraction of energy is usually not reconstructed and referred as *invisible energy*.

The reconstructed energy in a calorimeter is parameterized in literature [39] by

$$\frac{E_{vis}}{E} = \epsilon_e \left[1 + \left(\frac{\epsilon_h}{\epsilon_e} - 1 \right) F_h(E) \right] \tag{5.4}$$

where ϵ_e and ϵ_h are the efficiencies for the reconstruction of electromagnetic and hadronic energy deposits and F_h is the fraction of energy released hadronically. In most of the calorimeters $\epsilon_e \neq \epsilon_h$, which leads to a different response if the impinging particle interacts mainly electromagnetically (i.e. electrons) or hadronically (i.e. pions). The calibration of a hadron calorimeter should hence parameterize the two components involved in the energy deposition, by intrinsically determining ϵ_e and ϵ_h, and try to estimate F_h on a event-by-event basis.

5.3.1 Electromagnetic Energy Calibration

The calibration of the electromagnetic component of a shower is usually performed by studying the calorimeter response to impinging electrons and photons. In the NA62 HAC this possibility is ruled out by the presence of the LKr in front. Therefore a different approach based on the detector response to incoming muons is followed.

Energy Scale

The energy deposit by a muon when traversing a material is characterized by a Landau distribution typical of the ionization process. The most probable value of the energy release can be calculated analytically by multiplying the known average energy loss per unit of material, dE/dx, with the amount of crossed material. The scaling factor between charge and energy, for electromagnetic showers, is obtained by assuming linearity of the detector response. The distribution of the charge collected in each module of the HAC is fitted with a Landau function convoluted with a Gaussian, following the same scheme presented in 5.2.1. The expected energy release in the module is then divided by the MPV of the landau to obtain the calibration scaling factor parameter. The results are presented in Table 5.1. The computation for a muon momentum of 40 GeV/c is taken as reference point for the estimate of the calibration scale factor because the data analysed for this task were collected with the spectrometer magnet demagnetized, hence without any measurement of the track momentum.

The obtained scaling factors allow to combine the energy measurements by the two HAC modules. The point used for estimating the calibration parameters is located at the lower edge of the energy spectrum that the detector has to measure. Thus

Momentum [GeV/c]	E_{sc} [MeV]	E_{Fe} [MeV]	Charge [pC]	Scaling factor [MeV/pC]
		MUV1		
10	53.3	1000	3857	3.15
40	58.4	1166		
80	62.0	1326		
		MUV2		
10	27.3	933	2501	2.24
40	29.9	1087		
80	31.7	1237		

Table 5.1 – Computation of the calibration scale factors for MUV1 and MUV2. The expected energy deposit in iron (E_{Fe}) and scintillator (E_{sc}) is computed following ref. [40].

can lead to significant deviation of the measured energy respect to the deposited in presence of large energy releases.

Stopped Muons

Muons can be considered as a heavy copy of the electrons and can therefore release its complete energy by bremsstrahlung, even if with very tiny probability, producing an electromagnetic shower. The trigger mask implemented for the $K^+ \to \pi^+\nu\bar{\nu}$ measurement represents an excellent dataset to study muons being stopped inside the HAC. A sample of muons from the $K^+ \to \mu^+\nu_\mu$ decay is selected as described in Section 6.2. The selection is restricted to the events showering in the HAC by requiring an energy deposit in the electromagnetic calorimeter smaller than 700 MeV and no hit recorded by the MUV3 within 5 ns from the RICH time. More than $6 \cdot 10^6$ events are selected.

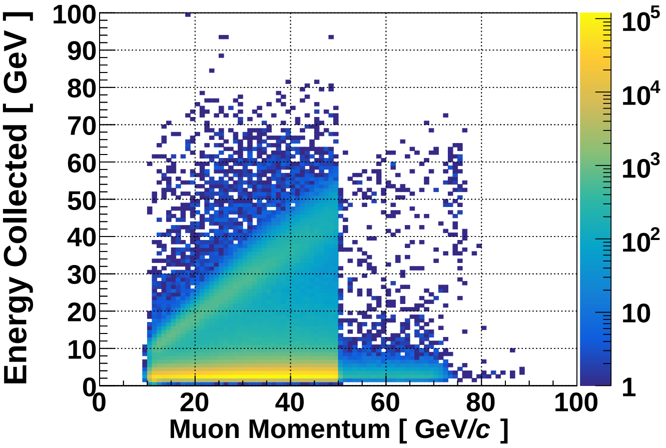

Figure 5.10 – Energy collected in the hadron calorimeter for muons not detected by the MUV3 detector.

The distribution of the total energy collected in the hadron calorimeter for the selected events is shown in Figure 5.10 as a function of the muon momentum. The cut-off at 50 GeV/c in the momentum distribution is determined by the L1 trigger requirement. The maximum in the low energy deposits originates from muons crossing the hadron calorimeter as minimum ionizing particles. A second signal, for events where energy and momentum are equal, contains the muons which release the energy completely inside the HAC.

The response of each HAC module to muon showers is studied by limiting the energy collected in the other to be below 2 GeV.

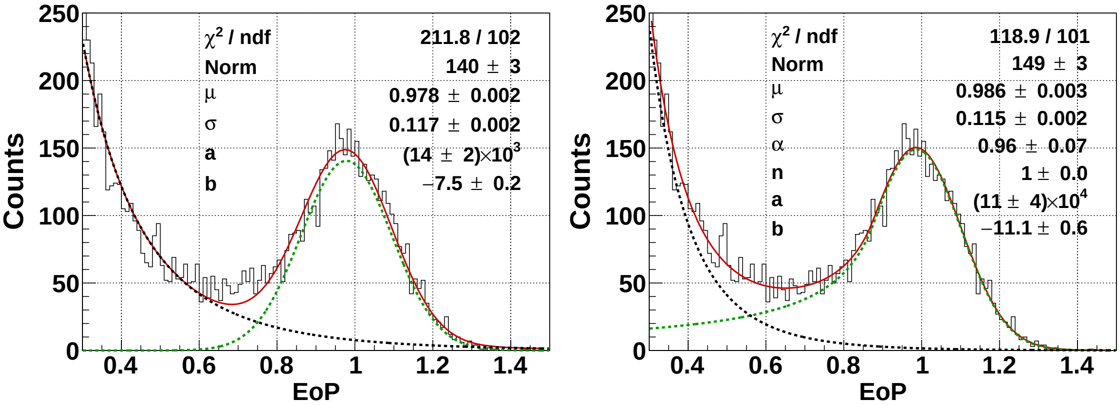

Figure 5.11 – Example of EoP distribution fits for 20 GeV/c muons showering inside the MUV1. On the left using a gaussian to describe the peak, on the right a Crystal Ball function.

The distribution of the ratio between the energy collected and muon momentum measured by the STRAW spectrometer (EoP) is fitted in bins of momentum to obtain the peak position. A simple model to parameterize the distribution above 0.4 is a falling exponential for muons with a partial energy release plus a gaussian for thus with the complete energy deposited (Equation 5.5).

$$f\left(x\right) = Norm \cdot e^{-\frac{(x-\mu)^2}{2\sigma^2}} + a \cdot e^{b \cdot x^{0.5}} \tag{5.5}$$

The decay of the muon during the shower development introduces a non gaussian tail on the lower side of the collected energy spectrum. The Crystal Ball (CB) function [41] provides an excellent parameterization of this energy losses. It consists of a gaussian core with a power-law extension on the lower energy side (Equation 5.6):

$$f(x) = Norm \cdot \begin{cases} e^{-\frac{(x-\mu)^2}{2\sigma^2}} & : \frac{x-\mu}{\sigma} \leq -\alpha \\ A \cdot \left(B - \frac{x-\mu}{\sigma}\right)^{-n} & : \frac{x-\mu}{\sigma} > -\alpha \end{cases} \tag{5.6}$$

where $A = (\alpha/n)^{\alpha} \cdot e^{-0.5 \cdot n^2}$ and $B = n/|\alpha| - |\alpha|$.
An example of the fit results of the two different modelling functions is shown on Figure 5.11. The Crystal Ball function, with the parameter n fixed to 1, improves the description of the tail leading to slightly higher value for the maximum.
The final EoP distributions are presented in Figure 5.12. The gaussian mean is systematically lower than the Crystall Ball. The shift can be considered as an estimate of the systematic uncertainty.

The reconstructed energy inside the detectors is underestimated and never reaches EoP = 1.

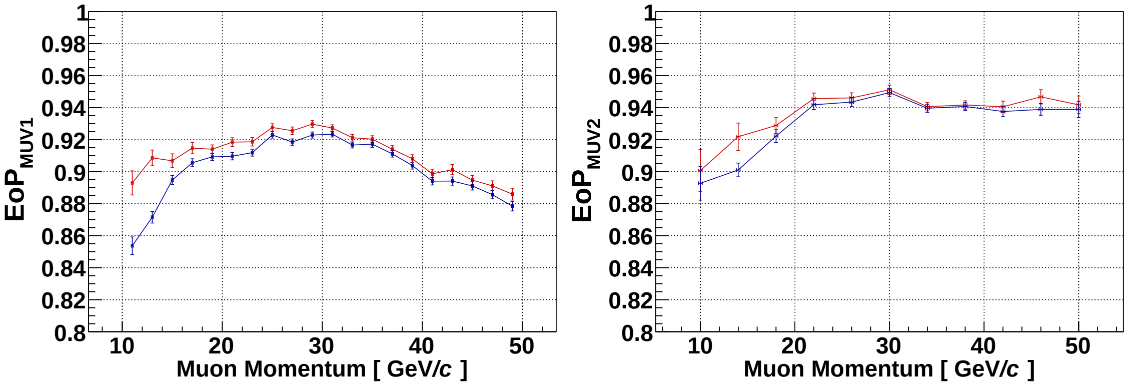

Figure 5.12 – Distributions of EoP as a function of the muon momentum for MUV1 (left) and MUV2 (right). Gaussian (Equation 5.5) and Crystal Ball (Equation 5.6) parameterization are plotted respectively in blue and red.

Equalization Biases and Check of Saturation Effects

The MUV1 detector counts 23 scintillator layers, 12 horizontal and 11 vertical. During the charge equalization the presence of a odd number of layers was not considered and photomultipliers connected to horizontally oriented strips collect roughly 10% more light. Therefore a study of unforeseen biases introduced by the equalization procedure is performed by exploiting the electromagnetic shower confinement on the transverse plane. The Molière radius R_M defines the radius of a cylinder containing in average 90% of the shower energy. For iron $R_M = 1.719\,\mathrm{cm}$, therefore, inside the HAC modules, more than 90% of the shower energy is collected by one scintillator per plane. Furthermore, differently to what happens with electrons, muon showers begin at any depth of the detector leading to a perfect equivalence between the energy collected in the vertically and in the horizontally oriented scintillators. The correlation between muon momentum and seed energy for different classes of strips provides the scaling factors to correct the equalization biases and allows to verify the presence of saturation effects that would lead to non-linearity of the detector response.

The requirement $E/p > 0.85$ allows to isolate stopped muons. MUV1 channels were classified by scintillator orientation (vertical or horizontal) and length of the strip (spanning the full detector length or only half of it), while MUV2 scintillators only by orientation. The ratio between seed energy and muon momentum as a function of the latter is shown in Figure 5.13 for MUV1 and MUV2. A clear difference between the vertically and horizontally aligned strip is visible, while the difference between long and short scintillators is considerably smaller. The origin of the discrepancy between vertically and horizontally oriented channels in the MUV2 was not expected and is not been understood yet.

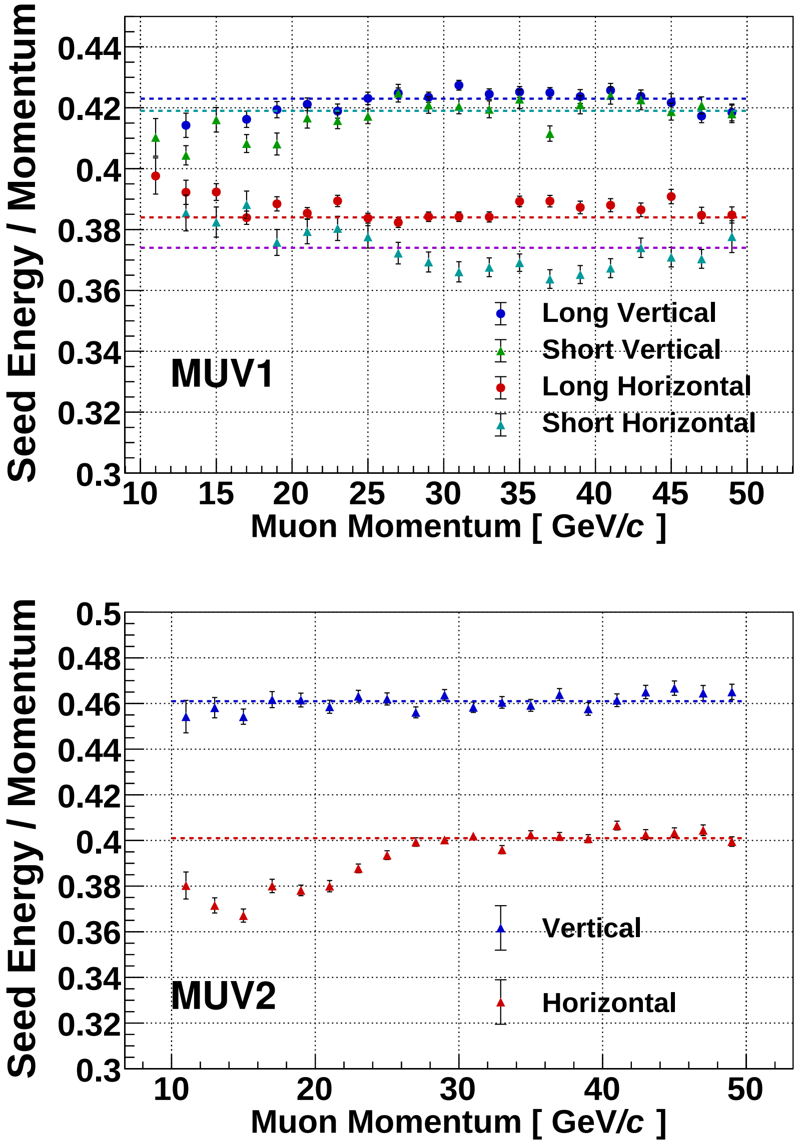

Figure 5.13 – Fraction of muon energy reconstructed in the seed for different categories of scintillators. Blue and green markers indicate vertically aligned strips, red and cyan horizontally. Triangles represents strips spanning only half of the detector length. The dotted lines shows the average value over the full momentum range. The distribution for horizontally aligned MUV2 channels shows a significant depletion at low momenta, therefore the region below 25 GeV/c was excluded by the mean calculation.

The highest value of the seed energy momentum ratio in each detector is used as reference to determine the scale correction on the other categories. The results are summarized in Table 5.2.

Module	Category	Seed Energy/Momentum	Correction
MUV1	horizontal-long	0.423	1.0
	horizontal-short	0.419	1.01
	vertical-long	0.384	1.10
	vertical-short	0.374	1.13
MUV2	horizontal	0.461	1.
	vertical	0.401	1.15

Table 5.2 – Scale factors for different scintillator categories in MUV1 and MUV2.

Radial Correction

The correction for different scintillator orientation results in a significant improvement of the energy reconstruction as shown in Figure 5.14. The MUV2 shows a good stability of the reconstructed energy which, applying a small scale correction, aligns to the EoP = 1 line. The MUV1 shows instead a decreasing trend of the reconstructed energy fraction for momenta above 30 GeV/c. The energy loss cannot be explained by saturation or detector non-linearity: the distribution of the ratio between the seed energy and the muon momentum is perfectly constant in the region of high momenta (see Figure 5.13).

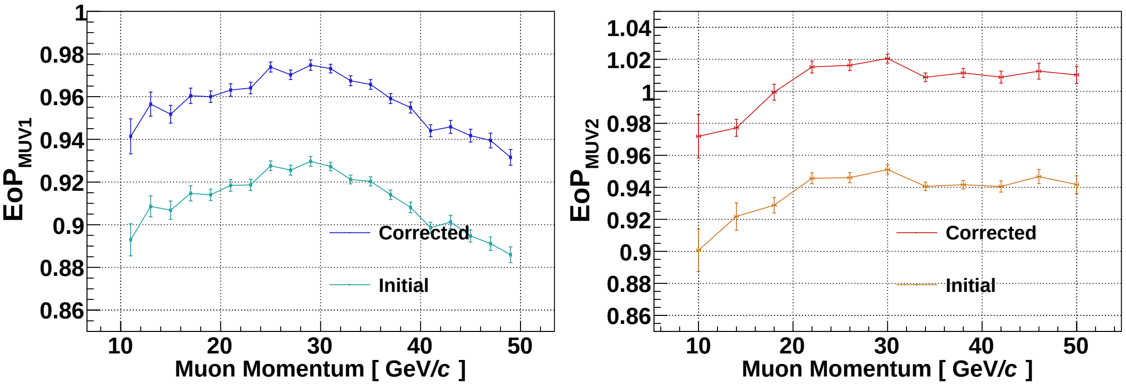

Figure 5.14 – Distributions of EoP as a function of the muon momentum for MUV1 (on the left) and MUV2 (on the right) before and after the correction due to the scintillators orientation.

However, at higher momenta, the radial impact position of the muons on the calorimeters is correlated with the momentum as presented on the left of Figure 5.15. This consideration leads to the presence of geometrical effects as a source of the energy loss. The EoP distribution as a function of the distance from the detector center shows a clear trend (Figure 5.15, right). The correlation was parameterized with a straight line and strongly improves the reconstructed EoP, as shown on Figure 5.16.

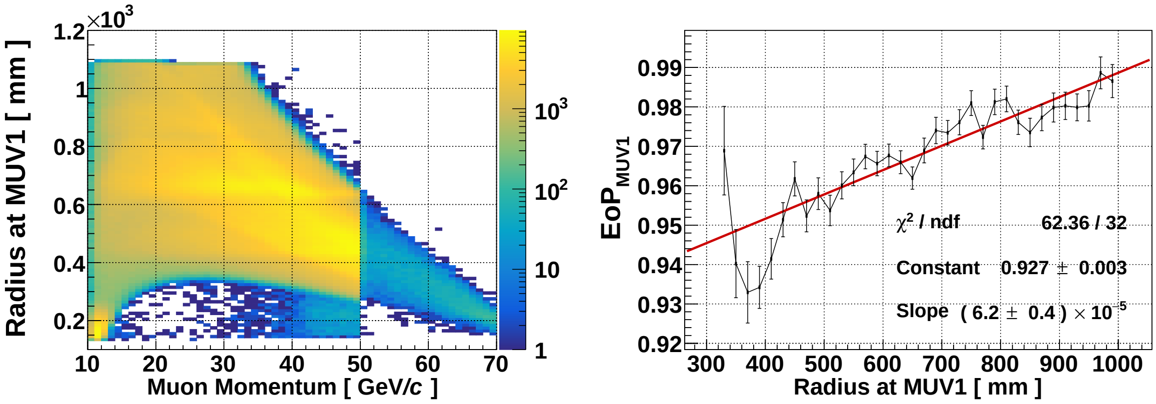

Figure 5.15 – Left: Muon radial impact point at the calorimeter as a function of the momentum. Right: Dependency of the reconstructed EoP on the radial impact position.

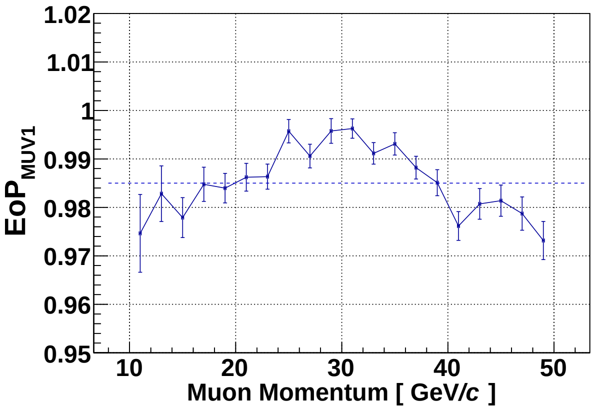

Figure 5.16 – MUV1 EoP as a function of the momentum after the correction for the impact position.

Results

At last the muon energies reconstructed in MUV1 and MUV2 are scaled respectively by a factor 1.012 and 0.985 to have the mean EoP centered at 1. Figure 5.17 shows the response of the hadron calorimeter to muon showers after the corrections. The EoP distribution shows very small deviations at momenta above 15 GeV/c. The width of the peak is an estimate of the detector energy resolution to electromagnetic cascade.

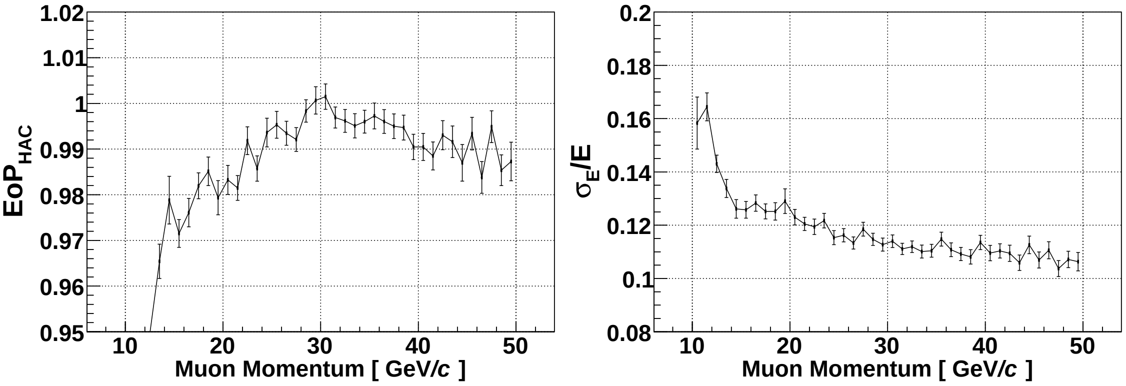

Figure 5.17 – Left: fraction of reconstructed energy in the HAC for stopped muons after all corrections. Right: width of the muon signal from the Crystal Ball fit which is an estimate of the energy resolution of electromagnetic showers.

5.3.2 Hadronic Energy Calibration

The analysis of the HAC response to hadrons is studied on a sample of pions produced through the $K^+ \to \pi^+\pi^0$ ($K_{2\pi}$,), decay, crossing the LKr without showering.

Sample Selection

$K_{2\pi}$ events are selected starting from the one track selection, described in Section 6.1, followed by the identification of the pion inside the RICH and rejecting events with a hit in the MUV3 within 5 ns from the RICH time. The selection is applied on data collected with a minimum bias trigger (Control and Mask0), preselected by the `FilterOneTrackTwoClusters` filter [26] [2], and on a sample of $50 \cdot 10^6$ Monte Carlo simulated $K^+ \to \pi^+\pi^0(\gamma)$ events. The kinematic variable $M^2_{miss} = (P_K - P_{\pi^+})^2$, computed with the nominal kaon momentum, is shown in Figure 5.18 (left) for the selected events as function of the track momentum. The selection is finalized by requiring M^2_{miss} to be within 0.006 GeV$^2/c^4$ from the squared π^0 mass.

A simple estimate of the background contribution to the sample can be performed by parameterizing the M^2_{miss} distribution around the peak using two concentric

---

[2] it requires at least one reconstructed track in the spectrometer and two clusters in the LKr calorimeter not associated to a track with a total energy, $p_{track} + E_1 + E_2$, in the range $[60, 80]$ GeV.

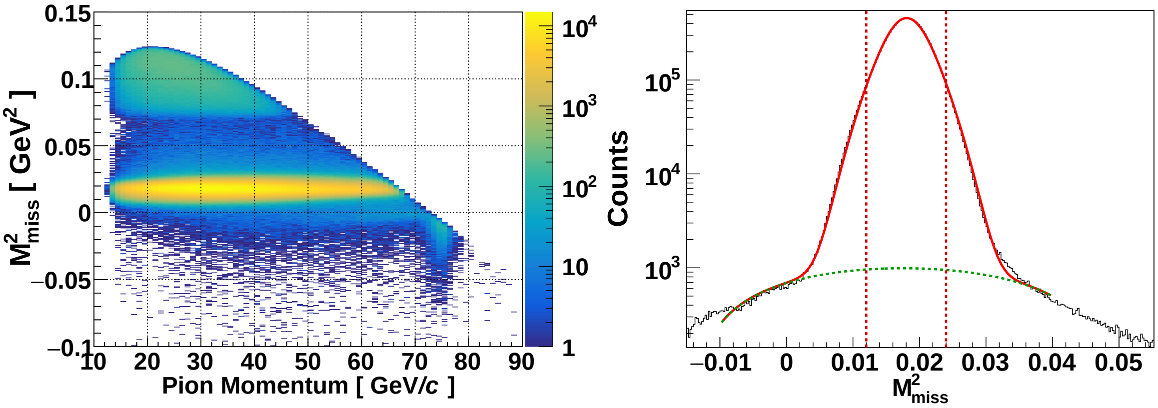

Figure 5.18 – Distribution of the kinematic parameter $M^2_{miss} = (P_K - P_{\pi^+})^2$ for selected $K_{2\pi}$ events on data, as a function of the momentum (left) and estimation of the background (right). The red lines indicate to selection cuts.

gaussians to reproduce the signal and a second order polynomial for the background as shown in Figure 5.18 (right). The method allows to set only an upper limit of 0.5% to the background contribution: a large fraction of the events falling in the background estimate are due to the radiative and kinematic tails of the $K_{2\pi}$ reconstruction. The calibration of the HAC response is performed considering only pions that do not shower inside the electromagnetic calorimeter. This is ensured by imposing an upper limit to the energy deposit at 700 MeV. The distribution of the reconstructed energy as a function of the pion momentum is shown in Figure 5.19 for data and MC.

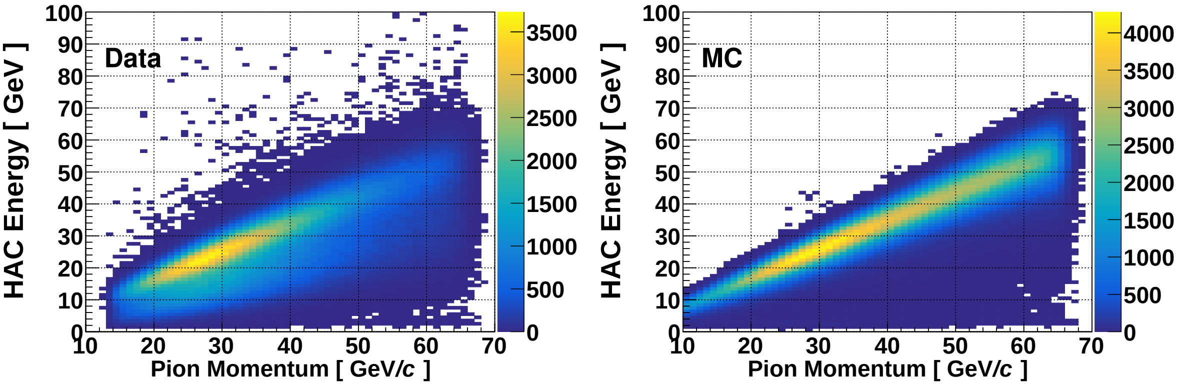

Figure 5.19 – Energy collected in the HAC as a function of the pion momentum for data (left) and MC (right).

Data-Monte Carlo Comparison

The spectra of collected energy have very different shapes in the two samples. The EoP distributions for pions in a 1 GeV/c wide momentum bin centered on 30 GeV/c are shown in Figure 5.20.

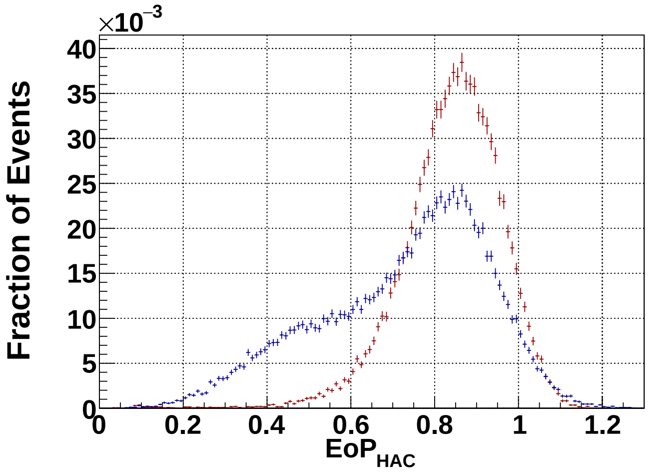

Figure 5.20 – Overlay of the EoP spectrum for data (blue) and MC (red) in a 1 GeV/c wide bin around 30 GeV/c.

The data distribution has a large tail at low EoP that is not reproduced by the simulation. The fraction of mis-reconstructed events was discovered to be strongly related to the distance between the reconstructed cluster position and the extrapolated track impact point in the data, as shown in Figure 5.21. This observation suggests a deep inelastic scattering happening in the material before the hadron calorimeter and deflecting the pion by an angle proportional to the transferred energy.

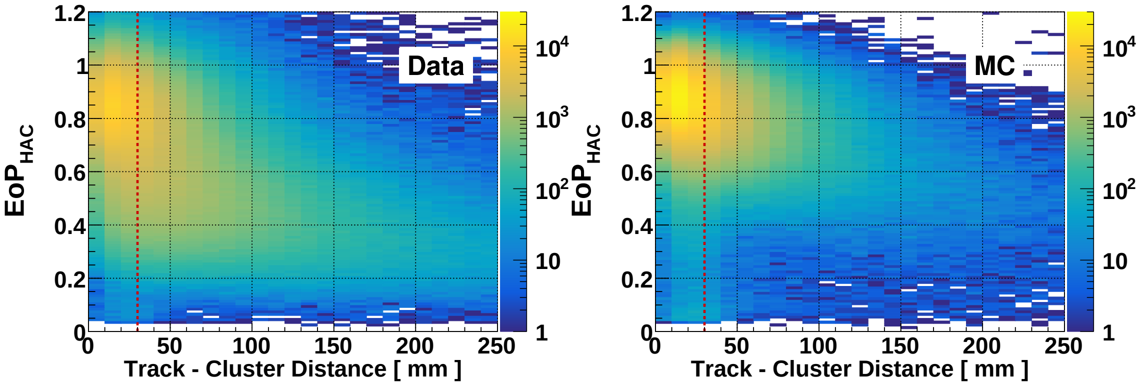

Figure 5.21 – EoP distribution as a function of the distance between reconstructed cluster position and track extrapolation for data (left) and MC (right).

Studying simulated events where the distance between reconstructed cluster position in the HAC and track extrapolation is larger than 5 cm, in most of the cases the pion was found to start showering at the end of the LKr active volume (Figure 5.22). This observation suggests the presence of passive material between the electromagnetic calorimeter sensitive region and the hadron calorimeter which is not (or not correctly) simulated. In order to validate this assumption, a part of the

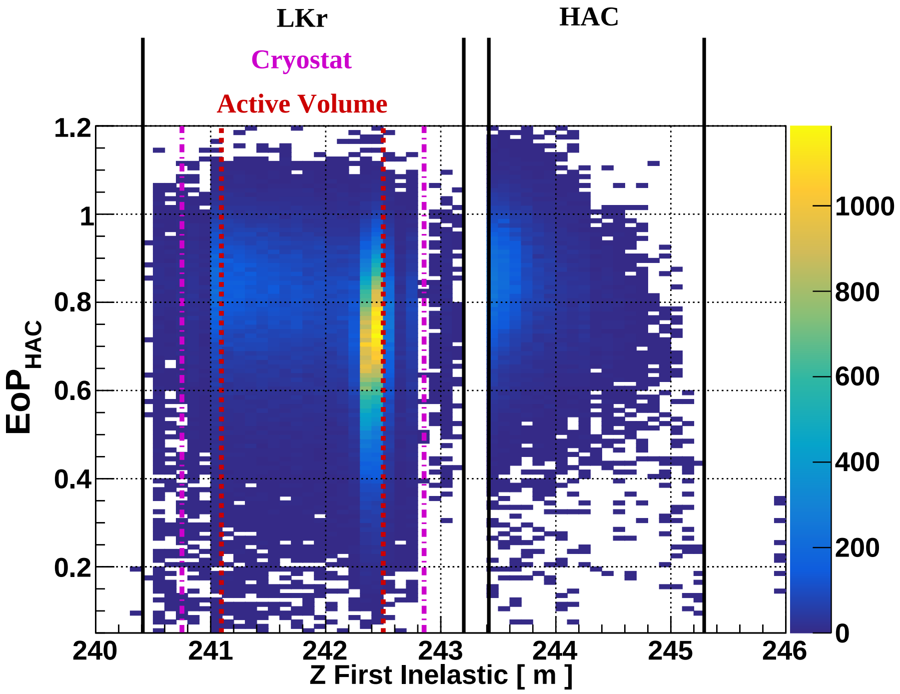

Figure 5.22 – Distribution of the EoP versus the coordinate of the first inelastic scattering of the pion for MC events. A clear enhancement in visible at the end of the active volume.

LKr active volume is passivated at analysis level. In events where the pion shower begins in the last 40 cm of the electromagnetic calorimeter active volume, the energy collected in this detector is replaced with the equivalent of events where the cascade begins inside the HAC. The comparison of the EoP spectrum for 30 GeV/c pions in the standard simulation, the tested condition and the data is presented in Figure 5.23. A significant improvement in the data/MC agreement is visible, thus validating the hypothesis about the origin of the data with a low EoP. On the other hand the amount of material needed to obtain a reasonable agreement between data and Monte Carlo is far too large (0.6 λ_{int} that correspond to 10 cm of iron) to be realistic. The real suspect for this effect is identified in the energy integration time window in the simulation which is set to 3 μs, leading to the reconstruction of energy from nuclear processes that in the data is lost.

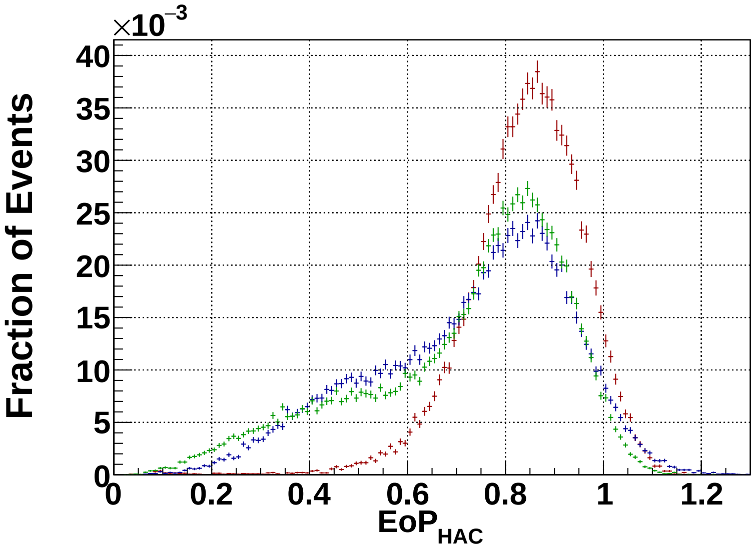

Figure 5.23 – Comparison of the EoP distribution for data in blue, MC in red and simulation with shorter LKr active volume in green.

A conservative cut on the distance between track extrapolation and cluster position is set at 30 mm in order to mitigate the impact of pion showers starting before the HAC on the calibration procedure. The energy lost in passive material before the hadron calorimeter is taken into account when fitting the EoP distributions by using a Crystal Ball function instead of a simple Gaussian.

Radial Dependency and Energy Losses in the Beam Pipe

The correction for MUV1 energy dependence of the radial impact position described in 5.3.1 is applied only in the data. The distribution of EoP, for events where more than 80% of the collected energy is deposited in the MUV1 and for momenta between 38 GeV/c and 40 GeV/c is showed in Figure 5.24 and the radial dependency is visible only in the data. A residual energy loss is visible both in data and MC for events at radii below 600 mm, due to energy losses within the beam tube. A correction for such energy losses is therefore needed in order to optimize the calibration. The correction for the energy losses inside the beam pipe is performed directly on data in order not to rely on the shower simulation. Pion showers with a impact radius at the MUV1 between 600 mm and 800 mm and releasing most of the energy inside the MUV1 are selected. The reconstructed profile of the shower obtained from the vertically and the horizontally oriented scintillators are combined into a two dimensional profile with a 6×6 cm^2 binning (1 strip × 1 strip). This spatial model of the energy deposit is shifted towards the beam tube in order to evaluate the fraction of the energy falling inside the beam tube area for different values of the distance.

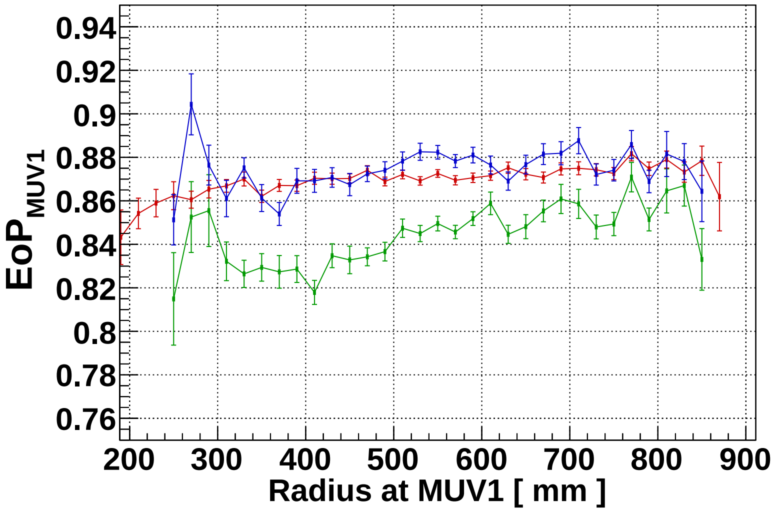

Figure 5.24 – Study of EoP dependency to impact radius to the beam pipe for pions releasing most of the energy in the MUV1. In red are simulated events, in green data before the correction, and in blue data after radial correction.

The EoP distribution versus the radial impact point is studied in bins of the reconstructed shower transverse size, shower width (SW), defined as:

$$SW = \sqrt{\frac{\sum E_{H,i} \cdot (x_i - \bar{x})^2}{E_H} + \frac{\sum E_{V,i} \cdot (x_i - \bar{x})^2}{E_V}} \tag{5.7}$$

where $E_{H/V,i}$ and x_i are respectively the energy and position of the horizontal (vertical) hit, $E_{H/V}$ and $\vec{x}$ are the energy in the horizontal (vertical) plane and the position of the reconstructed cluster. The mean of the EoP distribution in each 2 mm wide radial bin provides an estimate of the correction as shown in Figure 5.25. The correction for a certain value of shower width and radius is obtained as linear interpolation between the two nearest SW and radius points.

Since the detector geometries are very similar, the corrections for losses in the beam pipe obtained for the MUV1 are applied directly to the MUV2 by using the radius and shower width provided by the combination of the energy collected in the two modules of the HAC.

The two body decay nature of $K_{2\pi}$ events reflects in a correlation between pion momentum and radial impact position at the calorimeters as shown in Figure 5.26.

This allows to verify the impact of the beam losses correction on the data by looking to the fraction of reconstructed energy as function of the momentum (Figure 5.27). The EoP shows an improved stability in the momentum range $[50, 60]$ GeV/c. After 60 GeV/c the distance from the beginning of the beam tube drops below 15 cm and the energy correction is overestimated.

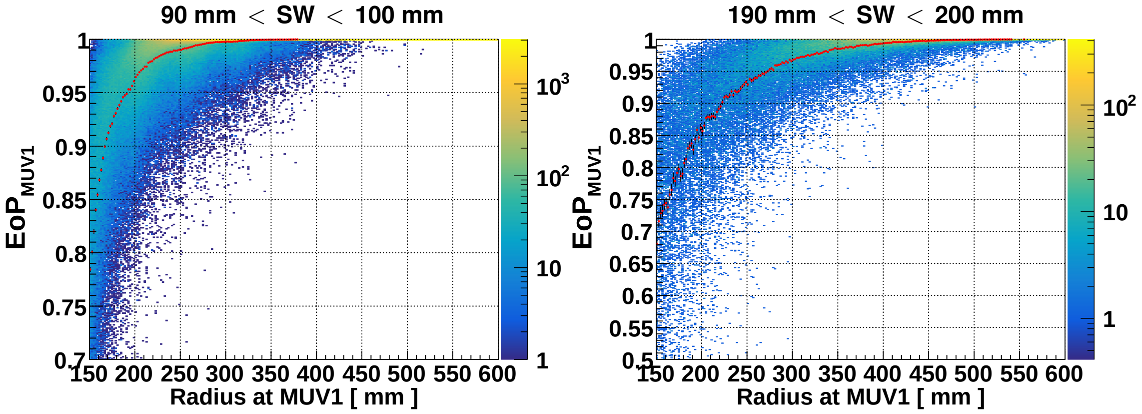

Figure 5.25 – Fraction of the energy released reconstructed in the MUV1 as a function of the radial impact position for showers of different shower widths (SW). The red points are the mean of the distribution in each bin.

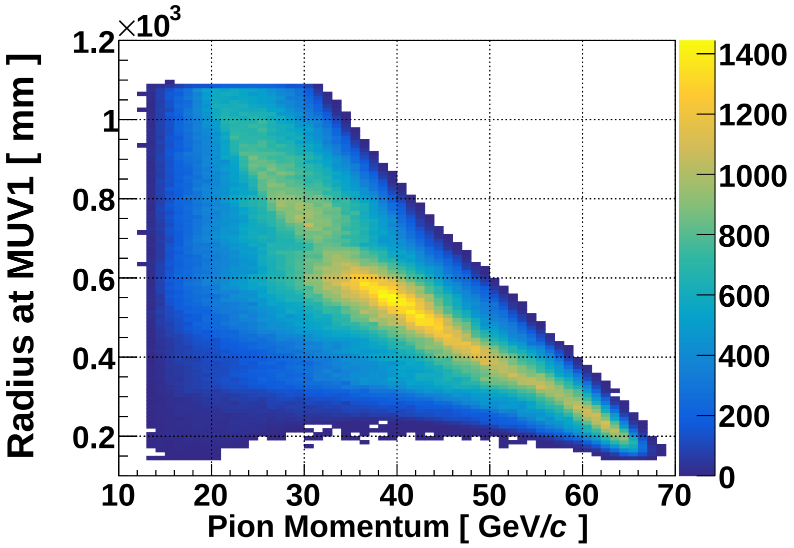

Figure 5.26 – Pion radial impact position as function of the momentum.

Visible Energy and Resolution Improvement

The fraction of visible energy can be parameterized as in Equation 5.4

$$\frac{E_{vis}}{E} = \epsilon_e \left[1 + \left(\frac{\epsilon_h}{\epsilon_e} - 1 \right) F_h(E) \right]$$

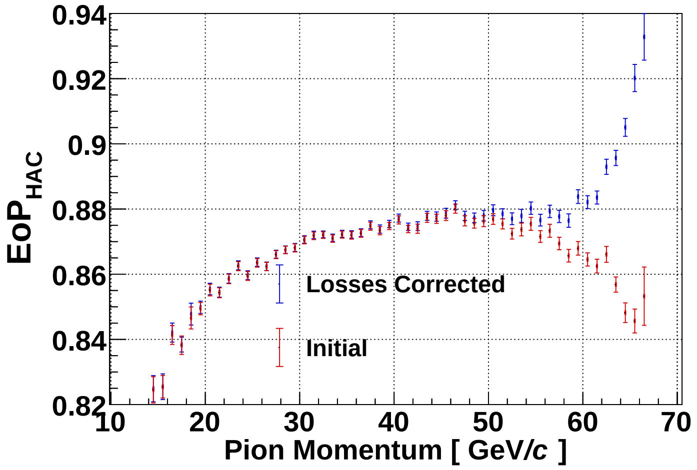

Figure 5.27 – HAC EoP before (red) and after (blue) correction for energy losses inside the beam pipe.

After the calibration of the electromagnetic energy response, it is possible to impose the efficiency of reconstructing the electromagnetic energy deposits to be $\epsilon_e = 1$. Calibrating the detector response to hadron showers corresponds to determine the reconstruction efficiency for hadronic energy deposits, ϵ_h, and the fraction of energy deposited by hadronic processes, $F_h(E)$, as a function of the particle energy. In a simplified assumption F_h depends only on the absorbing material and should therefore be almost identical between MUV1 and MUV2. The ratio ϵ_h/ϵ_e, instead, depends on the interplay between the active and the passive material of the calorimeter, hence is different between the two modules because of the different sampling fractions. Following these considerations the calibration parameters are evaluated separately for the two modules.

MUV1 A selection of pions fully stopped inside the MUV1 would provide a simple method to estimate the calibration parameter for this module, but that would bias the sample, since confining showers from high momentum pions inside a single module results in an enhancement of the electromagnetic component. Starting from the assumption that the difference between the calibration parameters of the two modules is relatively small, the MUV1 is calibrated by considering only showers with less than 30% of the energy in the MUV2 and treating the energy as if it was collected only by the front module.

The distribution of the visible energy for the MUV1 is shown in Figure 5.28.

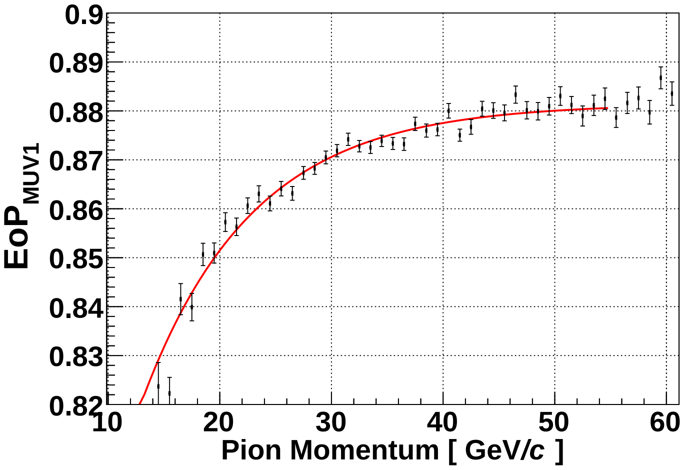

Figure 5.28 – Fraction of visible energy in MUV1. The red line shows the fit with Equation 5.8.

The fraction of visible energy is parameterized with the empirical function (shown in red in Figure 5.28)

$$\frac{E_{vis}}{E} = \epsilon_0 \cdot \left(1 - e^{-\frac{E+E_0}{E_c}}\right) \tag{5.8}$$

and obtaining the following values:

$$\begin{aligned} \epsilon_0 &= 0.8813 \pm 0.0008 \\ E_0 &= (14.5 \pm 2.2) \ \text{GeV} \\ E_c &= (10.4 \pm 0.7) \ \text{GeV} \end{aligned} \tag{5.9}$$

Correcting with this function, the result of the calibration is presented in Figure 5.29 for pion, on the left, and muon, on the right. While fixing correctly the energy scale for pions, the calibration overestimates severely the response to electromagnetic showers. Therefore an estimator of the fraction of energy deposited through hadronic processes is needed to limit this effect and improve the energy resolution.

A weight W is defined as :

$$W = \sqrt[4]{\sum_i \left(\frac{E_i}{E_{MUV1}}\right)^4} \tag{5.10}$$

where E_i is the energy collected in the channel i and E_{MUV1} is the cluster energy before any correction. The variable W is a measure of the lateral spread of the shower and provides a good estimate of the hadronic contribution.

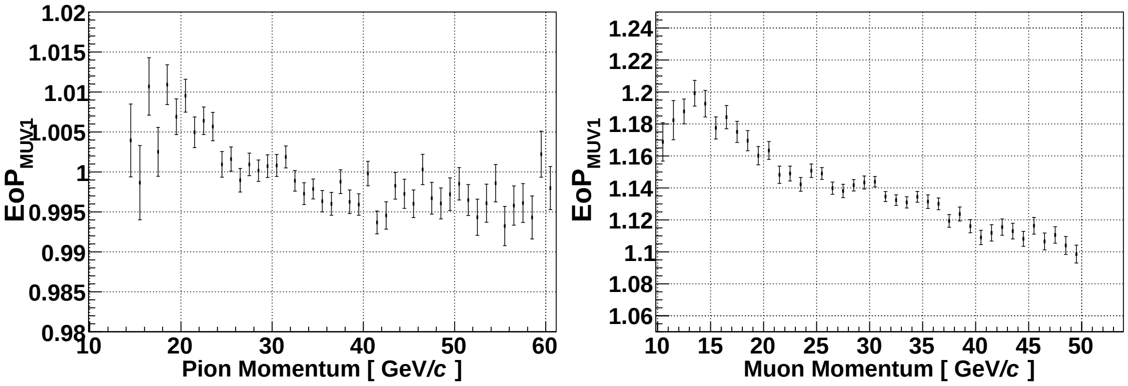

Figure 5.29 – Result of the visible energy correction on pions (left) and muons (right).

For fully electromagnetic showers most of the energy will be collected in only one channel per view resulting in $W \to 1$. Very large cascades, from hadrons, correspond to $W \to 0$. The forth power in the summation allows to enhance the separation power. Figure 5.30 shows the fraction of visible energy as a function of the weight parameter for different pion momenta.

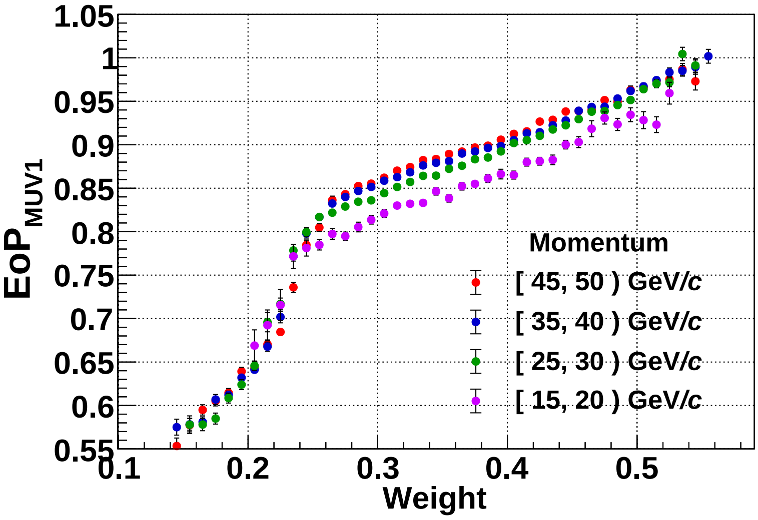

Figure 5.30 – EoP as a function of the weight parameter W in four momentum ranges.

Complementing the invisible energy correction with the information from the weight parameter, the calorimeter response to hadrons can be calibrated with smaller impact on the electromagnetic response.

The ratio between the energy, after the invisible energy calibration (Equation 5.8), and the pion momentum is then studied as a function of the weight parameter. The distribution, presented in Figure 5.31, is parameterized with the sum of a Fermi-

Dirac function and a first order polynomial:

$$\frac{E_{corr}}{E}(W) = a + \frac{b}{1 + e^{\frac{W+c}{d}}} + e \cdot W \tag{5.11}$$

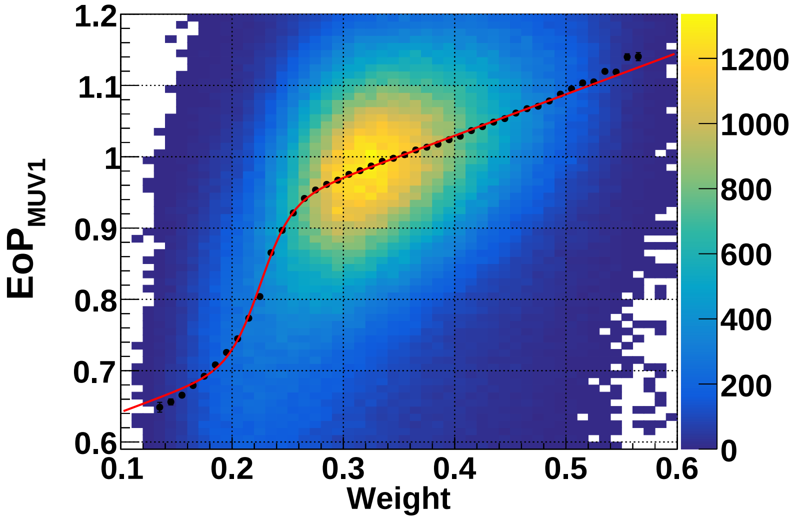

Figure 5.31 – Weight correction for MUV1 calibration. The red line shows the fit with Equation 5.11.

The fit results are:

$$\begin{aligned} a &= (5.89 \pm 0.02) \cdot 10^{-1} \\ b &= (2.05 \pm 0.02) \cdot 10^{-1} \\ c &= (22.65 \pm 0.06) \cdot 10^{-2} \\ d &= (1.26 \pm 0.04) \cdot 10^{-2} \\ e &= (5.86 \pm 0.04) \cdot 10^{-1} \end{aligned} \tag{5.12}$$

The result of the calibration is shown in Figure 5.32 for pions (left) and muons (right) respectively. The pion sample shows a perfect linearity of the calorimeter response for track momenta above 20 GeV/c with deviations limited to less than 2% for lower momenta. The reconstruction of the energy from muon showers is overestimated by up to 8%, reducing to 4% for momenta above 20 GeV/c.

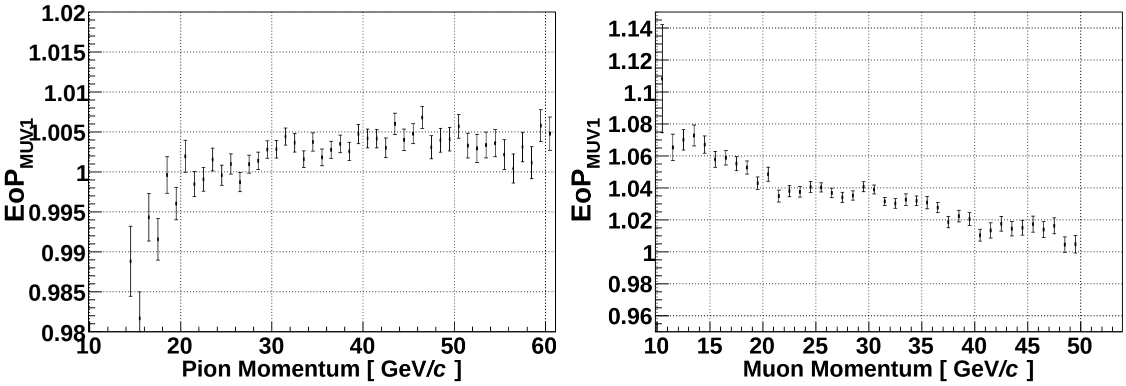

Figure 5.32 – Result of the energy calibration on pions (left) and muons (right).

MUV2 A direct application of the above procedure to the MUV2 is not feasible. Requiring the energy collected in the back module to be at least 70% of the total, reduces the number of usable pions to be less than 35000.

Therefore, a sample of pions with at least 40% of the energy collected in the MUV2 is considered. The fraction of visible energy is evaluated as the ratio between the energy seen in the MUV2 and the difference between the pion momentum and the energy collected in LKr and MUV1.

The fraction of visible energy in the MUV2 is shown in Figure 5.33. The distribution is fitted with Equation 5.8 to estimate the visible energy correction.

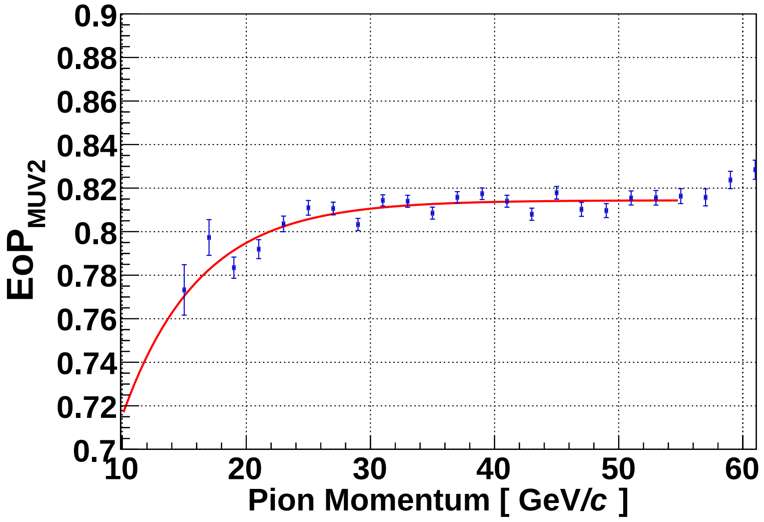

Figure 5.33 – Fraction of visible energy for the MUV2 detector. The red line shows the fit with Equation 5.8.

The fit yields:

$$\begin{aligned} \epsilon_0 &= 0.815 \pm 0.001 \\ E_0 &= (12 \pm 6)\ \text{GeV} \\ E_c &= (8 \pm 2)\ \text{GeV} \end{aligned} \tag{5.13}$$

The parameters E_0 and E_c defines the shape of the distribution and parameterize the fraction of the hadronic energy ($F_h(E)$) in the shower. Parameter ϵ_0 instead represents the ratio between electromagnetic and hadronic energy reconstruction efficiencies. As expected values of the $F_h(E)$ parameterization are in relatively good agreement in the two module (E_0 is 14.5 ± 2.2 (MUV1) and 12 ± 6 (MUV2), E_c is 10.4 ± 0.7 and 8 ± 2). The ratio of the reconstruction efficiencies, instead, is different: 0.881 in MUV1 and 0.815 in MUV2.
The MUV2 collects mostly the tail of showers starting in the MUV1, hence the estimate of the shower shape cannot leave aside the information in this module. In the approximation of a perfect geometrical alignment, two consecutive scintillators in the MUV1 cover the same area of one strip in the MUV2. The energy collected in these channels (two in MUV1 and one in MUV2) are summed into a single HAC channel energy (E_i^{HAC}). The weight is then defined, analogously to Equation 5.10 as:

$$W_{HAC} = \sqrt[4]{\sum_i \left(\frac{E_i^{HAC}}{E_{HAC}}\right)^4} \tag{5.14}$$

The correction for the weight parameter is evaluated drawing the ratio between the corrected MUV2 energy and the expected release in the detector as a function of W_{HAC} (Figure 5.34). Function in Equation 5.11 is again used to parameterize the correction with the following result:

$$\begin{aligned} a &= (1.00 \pm 0.02) \\ b &= (0.14 \pm 0.06) \\ c &= (0.52 \pm 0.02) \\ d &= (0.025 \pm 0.009) \\ e &= (-0.02 \pm 0.06) \end{aligned}$$

The result of the calibration is presented in Figure 5.35 for the pion and the muon samples, respectively on the left and right. The resulting non-linearity is within 1% for pions, while muon energies are overestimated by about 6% to 9%.

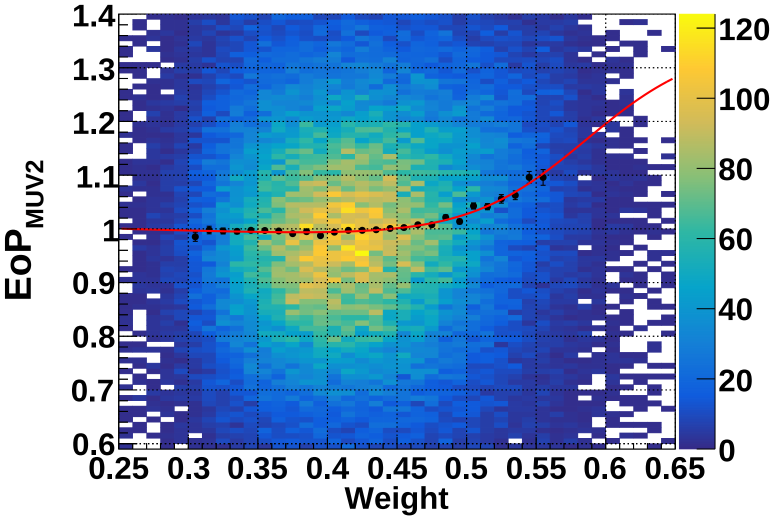

Figure 5.34 – Weight correction for MUV2 calibration. The red line shows the fit with Equation 5.11.

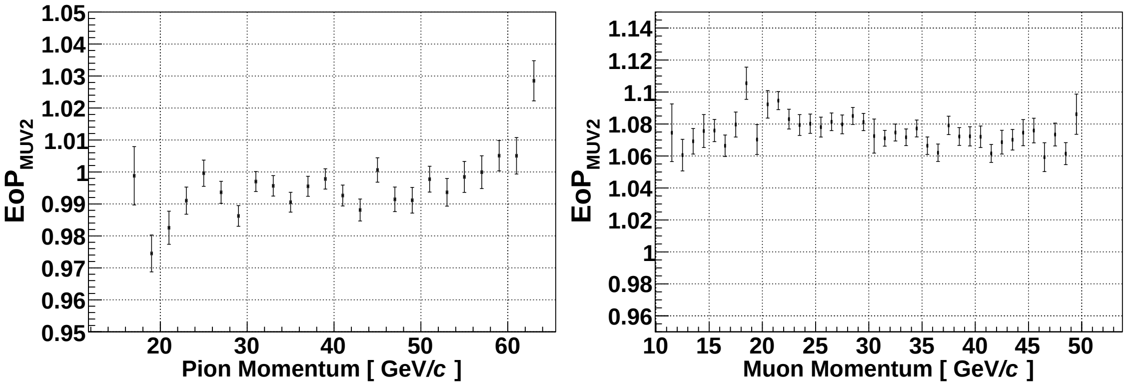

Figure 5.35 – Result of MUV2 energy calibration on pions (left) and muons (right).

Results

The HAC performances on pion energy reconstruction are evaluated with two different cuts on the distance between the reconstructed shower position and the track extrapolation. In the first sample the cut is placed at 3 cm, consistently to the calibration procedure, to mitigate as much as possible pions which release their energy in the passive material of the electromagnetic calorimeter. A looser cut at 20 cm is applied in the second sample, to ensure the correct track-cluster association.

The linearity of the hadron calorimeter to pion showers is within the percent level for the sample with a tighter cut on the distance, and within 3% for the second sample as shown in Figure 5.36. The difference in the result is due to events with the shower beginning inside the LKr, resulting in a slightly lower reconstructed energy.

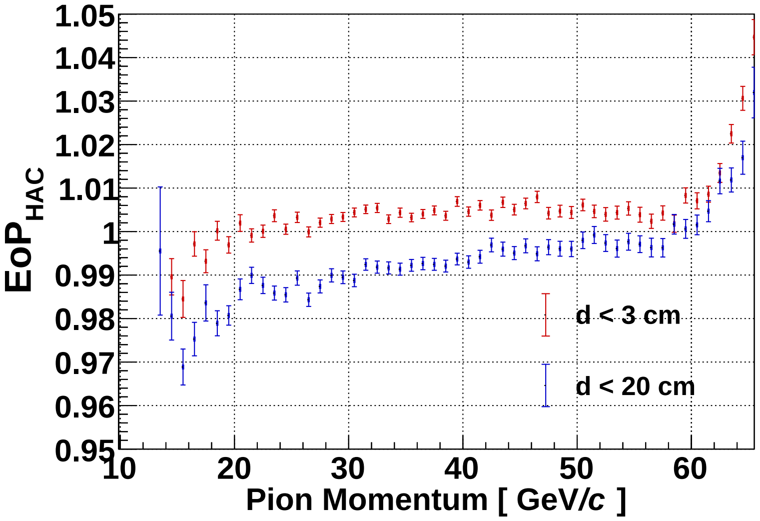

Figure 5.36 – Distribution of the ratio between HAC reconstructed energy and pion momentum after the calibration.

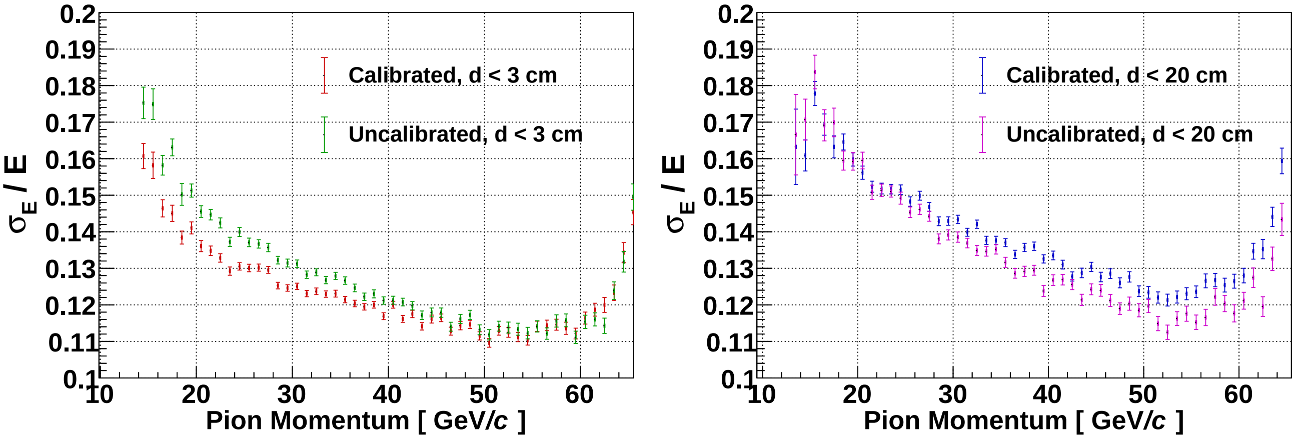

Figure 5.37 – HAC relative energy resolution before and after the calibration for two different distance cut.

The effect is clearly visible in the energy resolution (σ_E/E) before and after the calibration (Figure 5.37). The first sample shows a clear improvement of the energy resolution after the calibration, whereas the second shows a worse resolution at the higher momenta. Looking to the EoP distribution before and after the calibration in a certain momentum region, the improvement on the lower energy tail is clearly visible as shown in Figure 5.38.

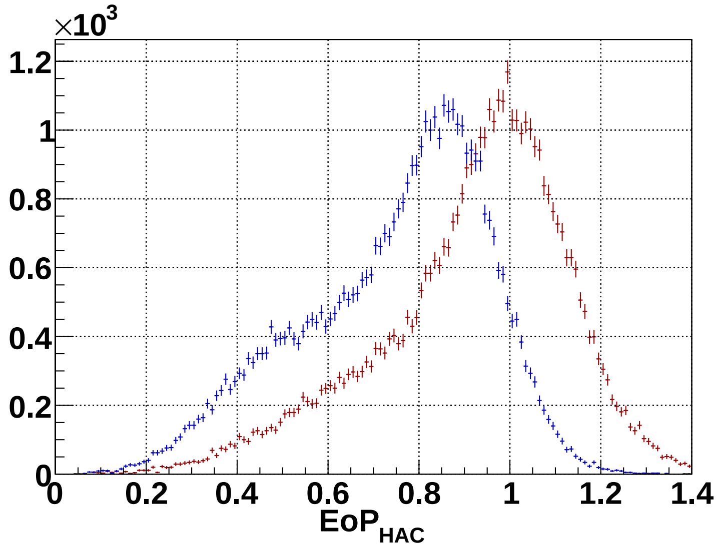

Figure 5.38 – Effect of the calibration on the EoP distribution for 30 GeV/c pions: blue before and red after correction.

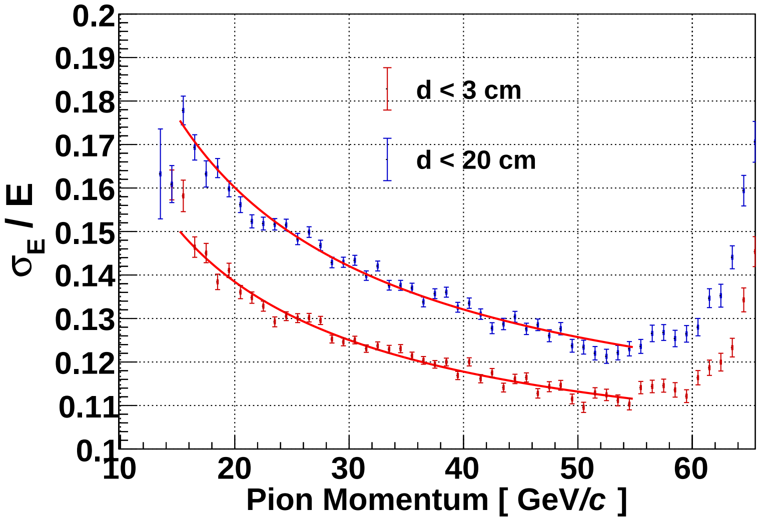

Figure 5.39 – Fit of the HAC relative energy resolution.

The energy resolution in the two samples is fitted with:

$$\frac{\sigma_E}{E} = a \oplus \frac{b}{\sqrt{E}} \oplus \frac{c}{E} \tag{5.15}$$

as shown in Figure 5.39.
The fit results are presented in Table 5.3:

- the constant term (a), related mostly to inhomogeneous response of the detector, is below the 10% level.

- parameter b, related to the sampling fluctuation (poissonian statistics), is comprised between 0.46 and 0.57. The two number are to be interpreted as lower and upper limits. Cascades with a strong electromagnetic component provide a better estimate of the pion impact position, instead a larger hadronic component determines a poorer space resolution. The sampling term of $0.46/\sqrt{E}$ is therefore probably driven by the electromagnetic component, whereas the scaling of $0.57/\sqrt{E}$ is strongly affected by events where part of the energy is lost before the HAC.

- the contribution of the noise, parameterized by c, to the energy resolution is negligible.

	$d < 3\,\mathrm{cm}$	$d < 20\,\mathrm{cm}$
Constant term a	0.093 ± 0.001	0.096 ± 0.001
Sampling term b	0.460 ± 0.005	0.572 ± 0.006
Noise term c	0	0
χ^2/Degrees of Freedom	55/37	68/37

Table 5.3 – Energy resolution fit results for two different values of cut on the distance between track extrapolation and reconstructed cluster position.

5.3.3 Comparison with Other Calorimeters

The performance of the NA62 hadron calorimeter are quite satisfactory. Table 5.4 compares the energy resolution of NA48 [31], NA62 and ATLAS Tile [42] Hadron Calorimeters. The energy resolution achieved in NA48, employing a similar hardware, is $0.69/\sqrt{E[\mathrm{GeV}]}$. This result was estimated with data collected in 1995, before the installation of the LKr calorimeter. At lower pion energies the HAC performs equally or better of the other detectors thanks to the smaller stochastic term. Starting from 30 GeV the high constant term results in a worse energy resolution.

Improvement of the HAC performances would not worth the effort because most of the pions start showering inside the LKr. Any future work to improve pion energy reconstruction should focus on the inter-calibration between LKr and HAC.

E [GeV]	Energy resolution σ_E/E			
	NA62		NA48	ATLAS
	d < 3 cm	d < 20 cm		
15	0.151	0.176	0.178	0.174
20	0.139	0.160	0.154	0.144
30	0.125	0.142	0.126	0.113
40	0.118	0.132	0.109	0.096
50	0.113	0.126	0.098	0.086

Table 5.4 – Comparison of NA62 HAC energy resolution to NA48 and ATLAS (Tile) Hadron Calorimeters.

5.3.4 Inter-calibration of Electromagnetic and Hadronic Calorimeters

The inter-calibration between the calorimeters is obtained by taking as a reference the NA31 procedure [43]. The fraction of visible energy cannot be estimated directly by showers fully contained in the LKr because the material in this detector accounts only for $1.7\lambda_i$. Moreover the very different structure and material composition of the electromagnetic calorimeter results in a different hadronic energy reconstruction efficiency depending at which depth in the LKr the pion starts showering and on its initial energy [44]. The EoP in the LKr – $E_{LKr}/\left(p_\pi - E_{HAC}\right)$ – is therefore studied as function of the fraction of energy collected by the HAC, $E_{HAC}/\left(E_{LKr} + E_{HAC}\right)$, in different bins of momentum (Figure 5.40). The distribution is then fitted with a

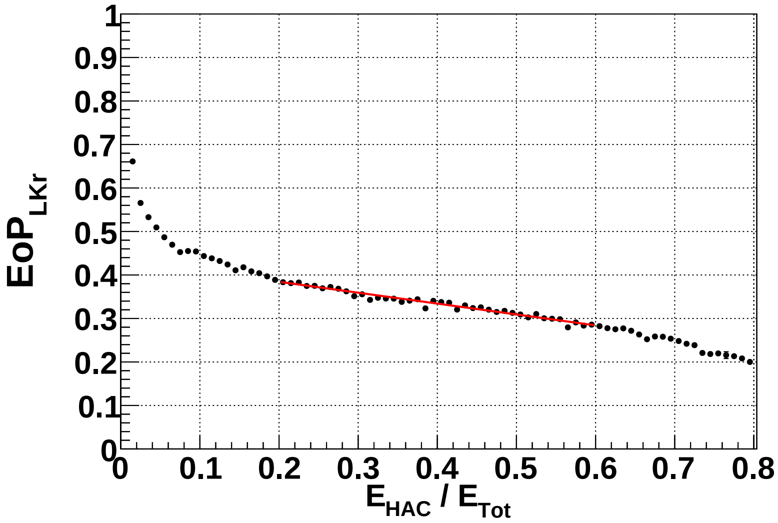

Figure 5.40 – Fraction of visible energy in the LKr as function of the fraction of energy collected in the HAC.

straight line in the region where the HAC collects between 20% and 60% of the total energy. The constant term of the fit represent the fraction of visible energy in the LKr and the slope the impact of the LKr on the global hadronic energy reconstruction efficiency. The obtain distribution of visible energy fraction as function of the pion momentum is fitted with Equation 5.8 (left of Figure 5.41, results in Table 5.5) and the distribution of the slopes with a straight line (Figure 5.41 right).

As final step the energy collected in the LKr is corrected using the RMS, transversal

ϵ_0	0.490 ± 0.001
E_0	(15.9 ± 0.6) GeV
E_C	(24.1 ± 0.5) GeV

Table 5.5 – Results of visible energy fit for the LKr.

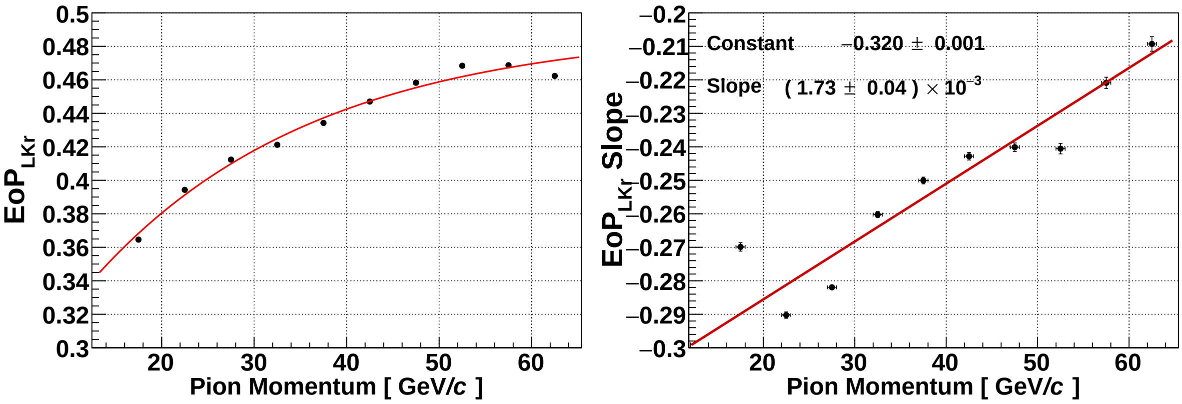

Figure 5.41 – LKr visible energy (left) and slope of the EoP as function of the pion momentum.

spread of the shower, as event-by-event estimator of the fraction of hadronic energy. The RMS of the shower is defined independently for the horizontal and the vertical size of the cascade (RMS_X and RMS_Y) as:

$$RMS_X = \sum_i E_i \cdot (x_i - \bar{x})^2 \tag{5.16}$$

where i runs over all the cells in a 5×5 square around the cluster seed, x_i and $\bar{x}$ are, respectively, the cell and the cluster positions. The RMS for the horizontal and vertical coordinates are then combined into a global RMS parameter:

$$RMS = \sqrt{RMS_X^2 + RMS_Y^2} \tag{5.17}$$

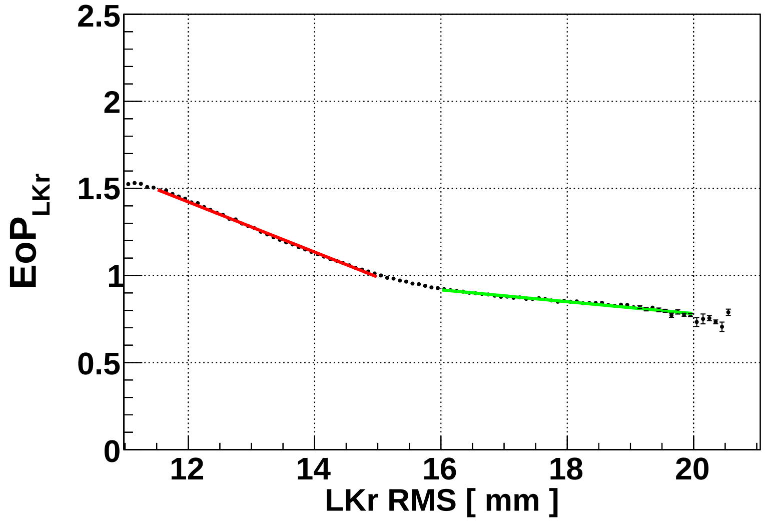

Figure 5.42 – LKr RMS correction.

The distribution of the EoP after the LKr visible energy scaling as function of the shower RMS is shown in Figure 5.42. The dependency is parameterized with two straight line, the first between 10 mm and 15 mm and a second after 16 mm. The correction is estimated in the region between the two lines extremes as the mean of the parametrizations weighted for the distance from the line end.

$$f(x) = \begin{cases} C1 + S1 \cdot x & x \leq 15 \\ C2 + S2 \cdot x & x \geq 16 \\ (C1 + S1 \cdot x) \times (16 - x) + (C2 + S2 \cdot x) \times (x - 15) & 15 < x < 16 \end{cases} \tag{5.18}$$

The obtained parameters are:

$$\begin{aligned} C1 &= 3.149 \pm 0.004 \\ S1 &= (-0.1439 \pm 0.0003)\,\mathrm{mm}^{-1} \\ C2 &= 1.463 \pm 0.007 \\ S2 &= (-0.0341 \pm 0.0004)\,\mathrm{mm}^{-1} \end{aligned}$$

The results of the inter-calibration are shown in Figure 5.43. The linearity of the detector response is preserved after the calibration within 3%. The improvement on the energy resolution is remarkable, reducing at 30 GeV from 35% to 25%. However the performance measured in the hadron calorimeter are far better. Hence any future improvement of the energy reconstruction should focus on the LKr and in the inter-calibration with the HAC.

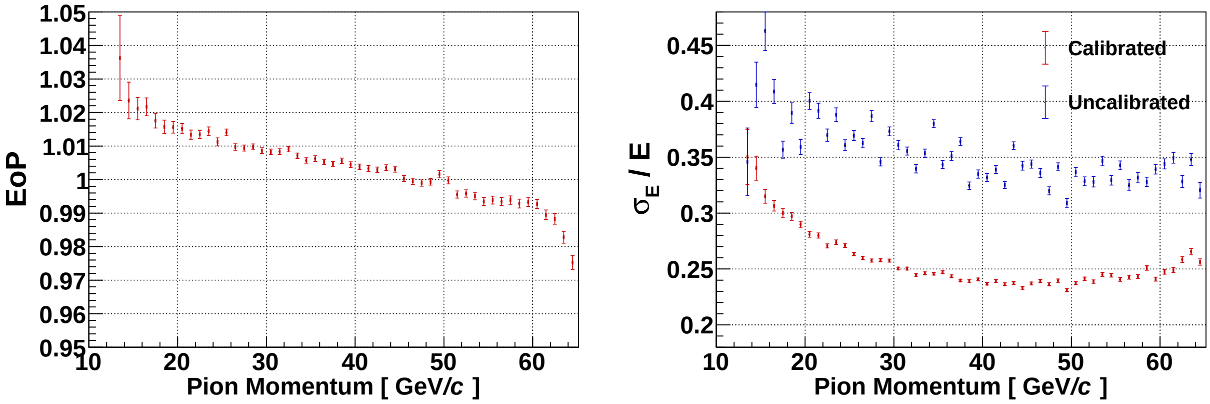

Figure 5.43 – Left: calorimeters EoP as function of the momentum after the calibration. Right: resolution of the reconstructed pion energy before (blue) and after (red) the calibration.

Chapter 6

Selection of a Pure Sample of μ^+, π^+, and e^+

The study of the calorimeter performance in particle identification (PID) requires the selection of two pure samples: a first, defined training sample, optimized to determine the selection cuts, and a second, the test sample, unbiased to verify the real performance of the defined analysis.

The main categories of particle from kaon decays are: pions, muons and electrons (positrons). The selection of the samples for these categories is performed on the leading kaon decays $K_{\mu 2}$ ($K^+ \to \mu^+ \nu_\mu$), $K_{2\pi}$ ($K^+ \to \pi^+ \pi^0$) and K_{e3} ($K^+ \to \pi^0 e^+ \nu_e$). The measurement of the $K^+ \to \pi^+ \nu \bar{\nu}$ branching ratio requires a factor 100 muon suppression from the calorimeters on top of the MUV3 veto. The selection of the training sample is therefore focused on the events surviving the requirement on the MUV3. The muon and pion contamination to the respective samples is to be kept below the percent level.

The test sample, instead, should allow to study the actual performance of the calorimeters PID standalone and in combination with the MUV3. The contamination of the samples is to be maintained as low as possible and at least below the 10^{-5} level for what concern the muon selection. The usage of MC simulations for the PID studies would allow to easily fulfill the requirements: the sample purity would be guaranteed and the statistics could be scaled up as much as needed. However the Monte Carlo simulation of hadronic showers is incomplete as pointed out in Section 5.3.2. Therefore, the selection of the samples is performed on data from the 2016A dataset:

- **Training Sample:** complete reconstruction output (non-filtered data) of runs 6587, 6614 and 6670.

- **Test Sample:** control trigger stream of runs 6371, 6582 and 6610 (`FilterPnn`)

The estimate of the background contribution to the selected samples is evaluated with Monte Carlo simulation of the following decays:

Decay	**Generated Events ($\times 10^6$)**
$K^+ \to \mu^+\nu_\mu$	81.8
$K^+ \to \mu^+\nu_\mu$ (decaying before GTK3)	195.6
$K^+ \to \pi^+\pi^0$	64.7
$K^+ \to \pi^+\pi^0$ (decaying before GTK3)	100.1
$K^+ \to \pi^0 e^+\nu_e$	36.6
$K^+ \to \pi^0\mu^+\nu_\mu$	18.4
$K^+ \to \pi^+\pi^+\pi^-$	40.7
$K^+ \to \pi^+\pi^0\pi^0$	7.8
$K^+ \to e^+\nu_e$	9.6
$\pi^+ \to \mu^+\nu_\mu$	5.9
$\pi^+ \to e^+\nu_e$	19.4

Table 6.1 – Table of simulated decay processes.

6.1 One-Track Selection (OTS)

The one-track selection (OTS) is the starting point for the selection of kaon decays with one charged particle in the final state. The selection proceeds as follows:

- identification of well-reconstructed tracks in the STRAW spectrometer and rejection of those forming good vertex with any other track
- association of the selected STRAW tracks with the CHOD and NewCHOD to obtain a precise time reference (STRAW time resolution is about 5 ns)
- matching of the tracks with remaining downstream detector
- determination and encoding of the event characteristics

For a better understanding of the selection, a short description of the STRAW track reconstruction procedure and of the vertex determination is provided.

STRAW Track Reconstruction The reconstruction of tracks in the STRAW spectrometer begins from the definition in each chamber of candidate space points, by grouping the hits in the different views. Track segments are then built combining the space points reconstructed in the two chambers before (1 and 2) and after

(3 and 4) the spectrometer magnet. A pattern recognition algorithm combines the reconstructed segments, evaluating the compatibility with the bending provided by the spectrometer magnet. Track candidates generated by the patter recognition algorithm are finally fitted with a recursive Kalman filter technique, considering the full 3-dimensional map of the measured MNP33 field. This step leads to the determination of the track parameters and to the estimate of a χ^2 variable representing the quality of the reconstructed track.

Determination of the Decay Vertex The reconstruction of the decay vertex in presence of two tracks, either two STRAW tracks or a beam track and a spectrometer track, is performed with the Closest Distance of Approach (CDA) technique. This algorithm propagate the track directions, determining analytically the position, in the three dimensional space, which minimizes their distance. This point is defined as the vertex of the event and the distance, referred as CDA, provides an estimate of the matching quality (in a decay the particles converge in a single point).

6.1.1 Selection of Single Particle Final States

The first step of the analysis consists in the selection of well-reconstructed tracks. Defined as well-reconstructed are tracks reconstructed using at least three out of the four STRAW chambers, respecting upper limits of $\chi^2 = 20$, and of $\Delta p = 30$ GeV/c of the difference between the momenta obtained by the fit and by the pattern recognition algorithms. In order to further reject spurious tracks arising from erroneous hit combinations, candidates built out of only three STRAW stations are required not to share more than one hit with a four-chambers track.

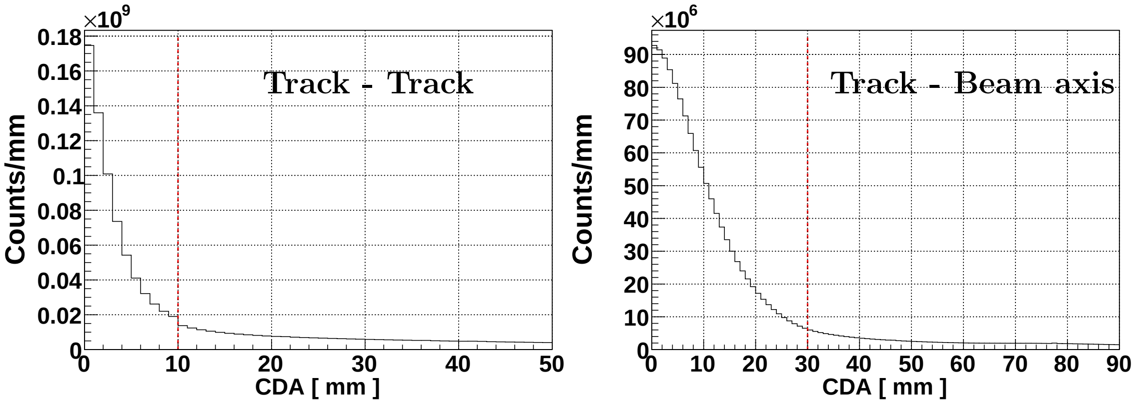

Figure 6.1 – Closest Distance of Approach for two reconstructed tracks (if at least two were reconstructed) on the left and for the tracks and the kaon beam axis on the right. The red lines show the selected cut values.

The condition of a single particle in the final state of the decay is obtained verifying that the track does not reconstruct a vertex with CDA<10 mm any other track (left of Figure 6.1). In case the test track is not classified as well-reconstructed, the CDAs of both tracks with respect to the beam axis is required to be smaller than 30 mm (right of Figure 6.1). This condition allows to reject most of the multi-track kaon decays, like $K^+ \to \pi^+\pi^+\pi^-$, with a considerably higher efficiency with respect to the requirement of only one reconstructed track in the event.

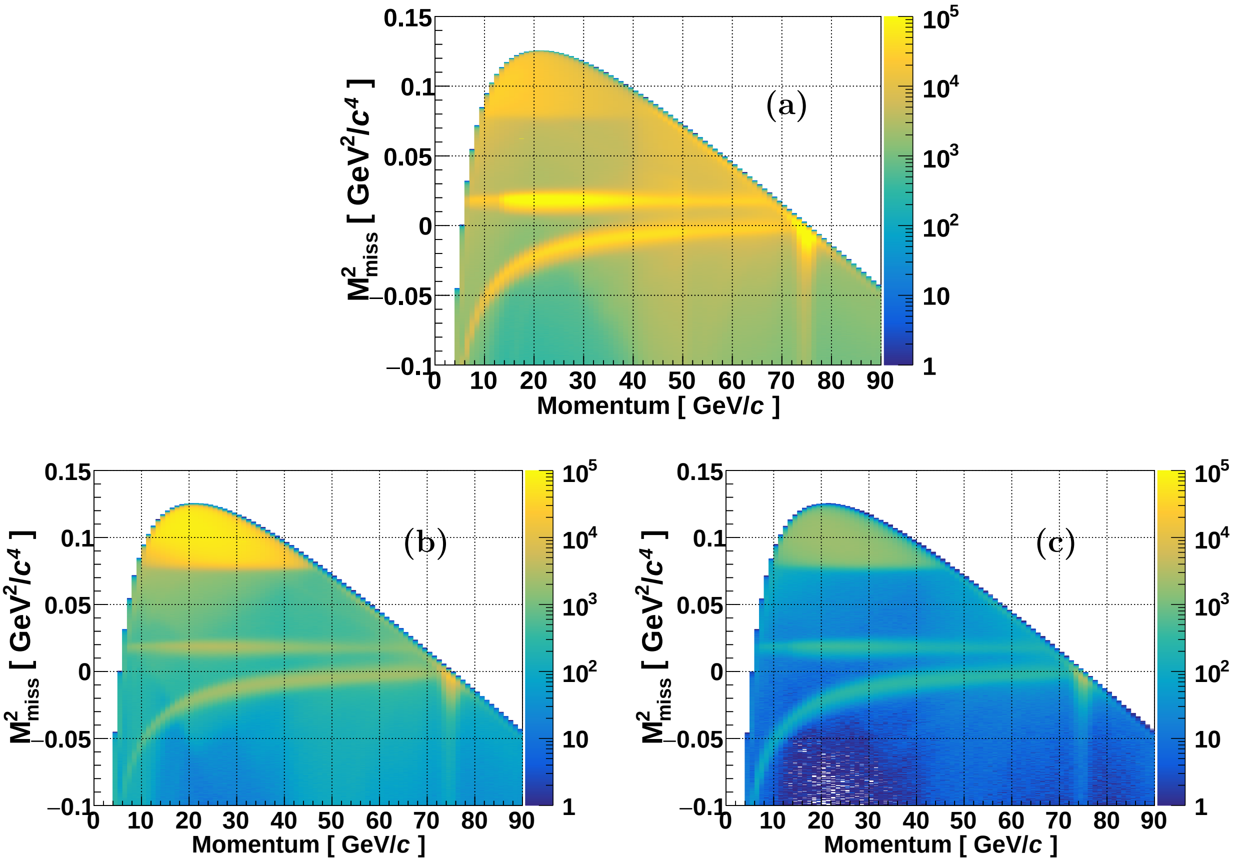

Figure 6.2 – Squared missing mass as function of the momentum for well-reconstructed tracks: (a) selecting as having CDA>10 mm with any other track; (b) for those rejected because having a CDA smaller than 10 mm with another well-reconstructed track; (c) for those rejected because having CDA<10 mm with a track not classified as well-reconstructed and both tracks having CDA<30 mm with respect to the beam axis.

The distribution of the squared missing mass $M^2_{miss} = (P_K - P_\pi)^2$, in the pion mass assumption and with the nominal beam parameters as kaon momentum, is shown in Figure 6.2: for events passing the selection (top) and in for those rejected (bottom). The effect of the selection is clearly visible in the different population of the $K^+ \to \pi^+\pi^+\pi^-$ ($K_{3\pi}$) region for $M^2_{miss} > 0.075$ GeV^2/c^4 for selected and

rejected events. The efficiency of the selection at this point is estimated to be about 94% by counting the number of events surviving the cut in the $K^+ \to \mu^+\nu_\mu$ band ($[-0.04, 0]$ GeV$^2/c^4$) in the momentum region between 15 GeV/c and 45 GeV/c.
The track charge is then required to be positive and its extrapolation is required to be within the geometrical acceptance of the RICH, the hodoscopes (CHOD, NewCHOD), the LKr, the HAC ,and the MUV3 and outside that of LAV12 (whose area partially overlaps with those of LKr and CHOD).

6.1.2 Association with Downstream Detectors

The second step of the selection is the matching of the selected tracks with the downstream detector signals. The matching is generally performed minimizing a discriminant defined as:

$$D = \sqrt{\left(\frac{T_{cand} - T_{ref}}{\sigma_T}\right)^2 + \left(\frac{X_{cand} - X_{extrapolated}}{\sigma_X}\right)^2} \tag{6.1}$$

where T_{cand} and X_{cand} are the time and two dimensional position of the reconstructed candidate in the matched detector, T_{ref} the reference time of the considered track and $X_{extrapolated}$ the extrapolated track impact point at the considered detector. The parameters σ_T and σ_X are an estimate of the matching time and space resolution, obtained from the distributions of the time difference and distance between the track and all the reconstructed candidate. The selected candidate is then required to be within a certain time and space distance in order to reject incorrect associations. Table 6.2 provides a summary of the parameters used for the association of the track with the downstream detectors.
The RICH does not provide the impact position. The center of the Cherenkov ring, however, is correlated with the direction of the crossing particle by

$$\begin{aligned} X &= p_x/p_z \times L_f \\ Y &= p_y/p_z \times L_f \end{aligned} \tag{6.2}$$

where L_f is the focal length, 17 m. Therefore the expected and reconstructed centers of the RICH rings are used instead of the impact positions.
The spatial coherence of the tested MUV3 signals is verified, taking into account the effect of multiple scattering, before the minimization of the discriminant by the usage of the `SpectrometerMUV3Association` tool [26]. The matching with the calorimeters (LKr and HAC) is performed using the `SpectrometerCalorimetersAssociation` tool described in Section 3.3.

Detector	T_{ref}	σ_T	σ_X	dT_{max}	dX_{max}
CHOD	STRAW	5 ns	10 cm	20 ns	10 cm
NewCHOD	STRAW	5 ns	10 cm	20 ns	10 cm
RICH	CHOD	1 ns	2.5 cm	3 ns	7.5 cm
MUV3	RICH/CHOD	2 ns	10 cm	5 ns	-

Table 6.2 – Parameters for the track-detector association.

After a successful matching of the track with the hodoscopes, the CHOD time (about 350 ps resolution) is used as reference time for the track. In case also a RICH candidate is found, the reference time is then changed to the ring time whose resolution is about 140 ps.
A track is selected only if:

- has a match with CHOD and NewCHOD;
- has an associated energy release in the LKr greater than 250 MeV;
- has a total associated energy (LKr+HAC without inter-calibration) larger than 1 GeV and smaller than 1.5 times the track momentum (in NA62 the contribution of the particle mass to the energy is usually negligible).

About 87% of the tracks have a match with both CHOD and NewCHOD, and 90% of those survive the requirements on the energy collected in the calorimeters.

6.1.3 Event Flagging

In order to simplify the selection of physics samples, the event is assigned several flags describing its peculiar characteristics:

- RICH particle identification;
- Kaon tagging;
- In-time beam activity (CHANTI);
- Matching with reconstructed beam tracks (GTK);
- Photon vetoes (LKr, LAV, SAV);
- Reconstruction of $\pi^0 \to \gamma\gamma$ with the LKr.

RICH Particle Identification The particle identification inside the RICH is performed with the help of a standard tool (`SpectrometerRICHAssociation` [26]), providing an interface to a likelihood analysis of the event. The momentum of the track, measured by the spectrometer, is used to compute the expected radius of the Cherenkov ring under different mass hypotheses – electron, muon, pion and kaon. The compatibility of the recorded RICH configuration to the tested hypothesis is expressed by a likelihood. In case the obtained value is larger than 0.75 the flag of the corresponding particle flavour is set. This method provides a good separation for momenta below 30 GeV/c, but results in tracks having multiple associated flavours at higher momenta, since the differences between the rings from electrons, muons and pions approach the limit of the detector resolution. The efficiency for selecting pions, muons and electrons as a function of the momentum is shown in Figure 6.3.

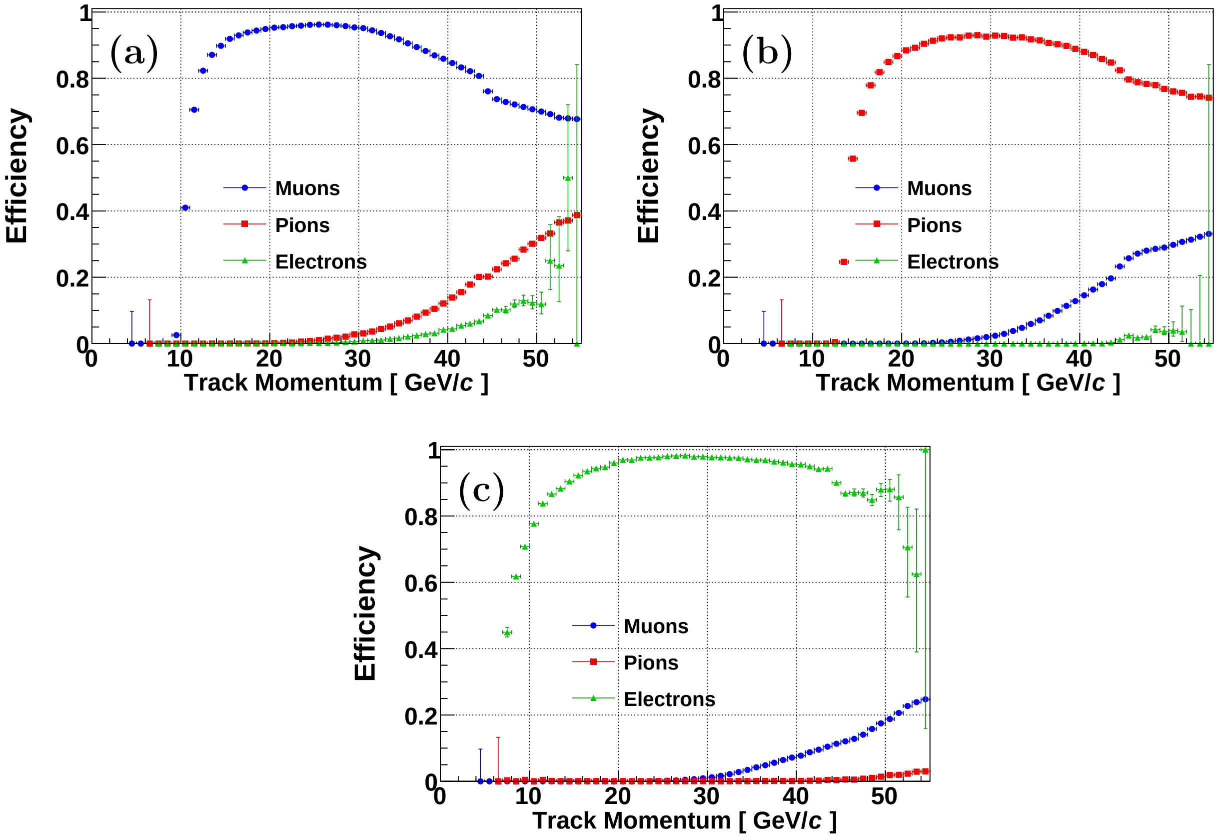

Figure 6.3 – RICH efficiencies for muons (blue), pions (red) and electrons (green) when requiring muon (a), pion (b) or electron (c) identification from the selected training samples (Sections 6.2, 6.3 and 6.4).

Kaon Tagging The identification of a kaon in the event is performed independently to the matching with a beam track in the GTK.

A signal in the KTAG is defined as a kaon candidate when it originates from the coincidence of at least 5 sectors. The candidate is accepted if the its time is within 2 ns from the track reference time (RICH or CHOD as previously described).

In-time Beam Activity The three stations of the GTK represent a small, but not-negligible, source of background due to the scattering of beam particles on the silicon. In particular inelastic scattering of a kaon on the last GTK station may produce several charged particles out of which only one enters the apparatus mimicking a kaon decay. These events are rejected by vetoing signals in the CHANTI in a 5 ns time window around the track reference time.

Matching with Reconstructed Beam Tracks The high intensity of the NA62 beam results in a large multiplicity of hits recorded by the GTK. Among the several tracks that can be reconstructed out of these hits, only few originate from a particle. The GTK reconstruction (as performed in `GigaTrackerEvtReco` [26]) requires the momenta and directions of the tracks to be compatible with the nominal beam parameters (momenta in $[72, 78]$ GeV/c, and directions, with respect to the z-axis, after TRIM5 in $[0.9, 1.6]$ mrad and in $[-0.3, 0.4]$ mrad respectively for the x and y components). Further quality cuts, applied in the analysis, are $\chi^2 < 8$ for time compatibility of hits in the three GTK stations and $\chi^2 < 20$ for the track fit (hit position with respect to fit position) as shown in Figure 6.4.

The matching between STRAW and GTK tracks is based on the minimisation of

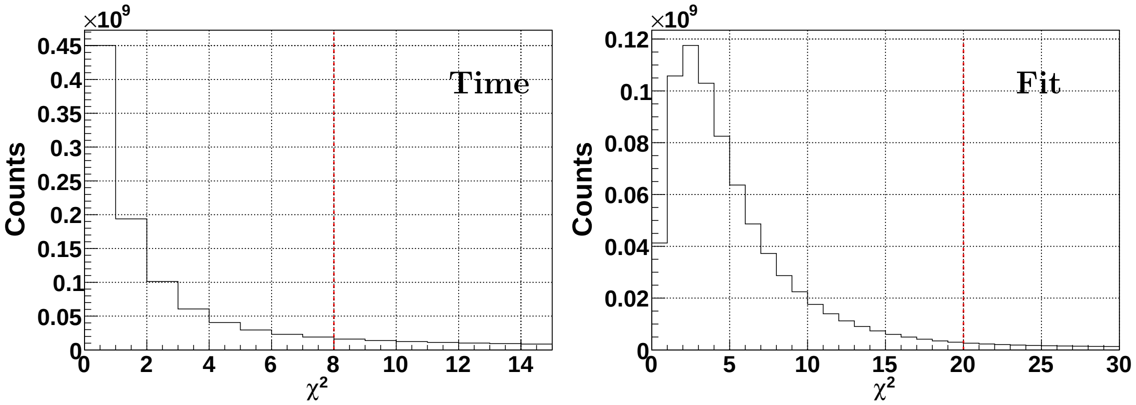

Figure 6.4 – Distribution of the χ^2 parameters expressing the time compatibility of the hits in the GTK stations (left) and the quality of the track fit (right). The red lines show the selected cut values.

the discriminant

$$D = \sqrt{\left(\frac{T_{GTK} - T_{ref}}{\sigma_T}\right)^2 + \left(\frac{CDA}{\sigma_{CDA}}\right)^2} \tag{6.3}$$

with T_{GTK} the GTK track time, T_{ref} the reference time of the track in the downstream detectors (CHOD or RICH time), $\sigma_T = 1$ ns a guess of the matching time resolution, CDA the closest distance of approach between GTK and STRAW tracks, and $\sigma_{CDA} = 25$ mm a guess of the GTK-STRAW CDA resolution. The discriminant D of the selected track is required to be smaller than 4.
The resolution improvement on the kinematic variable M^2_{miss} is clearly visible in figure 6.5. About 63% of the selected STRAW track have an associated GTK track. In the selection of the samples for the PID studies, events missing the GTK association are rejected.

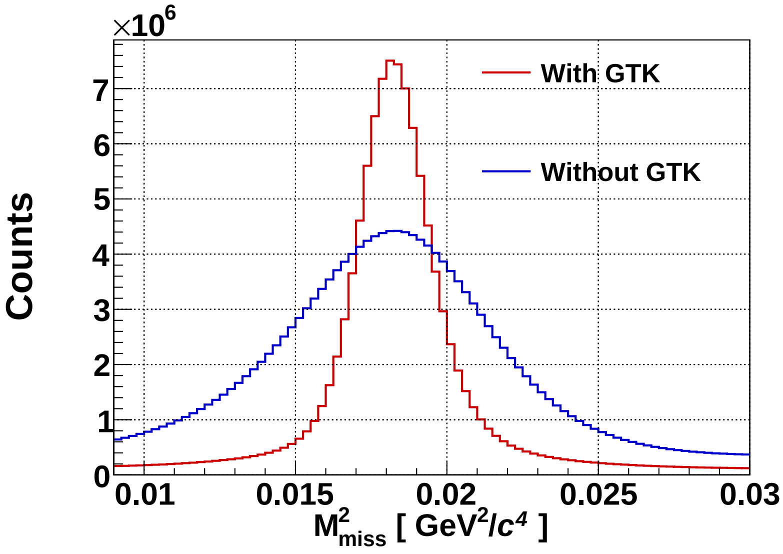

Figure 6.5 – Distribution of M^2_{miss} around the $K_{2\pi}$ peak evaluated with the GTK and with the nominal beam parameters.

Photon Vetoes Detection of photons is a crucial task in order to measure the $K^+ \to \pi^+\nu\bar{\nu}$ decay branching ratio, therefore the NA62 is equipped with several detector devoted to this task.

LAV The Large Angle Veto (LAV) performs the detection of photons emitted at large angle with respect to the beam axis ($[8, 50]$ mrad). Signals from the LAV are analysed using the `LAVMatching` tool [26]. The flag for photons in the LAV is set if at least two lead glass blocks have signals within 5 ns from the track reference time.

SAV The Small Angle Veto system (SAV) extends the coverage for photons inside the beam pipe. The readout of these detectors is performed both by TDC-based readout and CREAM boards. In the first case data are analysed similarly to those from the LAV using the `SAVMatching` tool [26]. A veto is produced if any of the channels has a signal within 5 ns from the track reference time. The information collected with the CREAMs allow to perform the reconstruction of the energy released in the detectors. If an energy deposit of at least 750 MeV is recorded within 15 ns the event is flagged as having photons in the SAV.

LKr The electromagnetic calorimeter provides the largest contribution in gammas detection. The flag for photons in the LKr is set if a reconstructed cluster is found within 15 ns from the track reference time, at least 30 cm away from the expected track impact position, and with an energy of at least 1.5 GeV.
The clustering procedure in the standard reconstruction is inefficient at the level of about 0.5%. Therefore, all in-time hits with at least 40 MeV and not belonging to any reconstructed cluster are used to perform a new clustering. In case the sum of the energy from hits inside a circle of 10 cm radius is larger than 1 GeV the LKr photon flag is set.

Reconstruction of $\pi^0 \to \gamma\gamma$ with the LKr Several kaon decay channels have neutral pions in the final state. The LKr offers an effective tool to reconstruct π^0s by looking for the photons of the $\pi^0 \to \gamma\gamma$ decay ($Br\,(\pi^0 \to \gamma\gamma) = 98.2\%$ [12]).
A combination of two LKr clusters is considered to be a π^0 candidate if:

- the distance between each cluster and the track impact position is at least 30 cm
- both clusters are associated with an energy deposit larger than 3 GeV
- both clusters are within 15 ns from the reference track time
- the time difference between the two clusters is smaller than 5 ns

The 4-momentum of each photon forming the candidate is reconstructed as:

$$P_\gamma = \left(E_{LKr}, E_{LKr} \frac{\vec{X}_{LKr} - \vec{X}_{Vertex}}{|\vec{X}_{LKr} - \vec{X}_{Vertex}|} \right) \tag{6.4}$$

where $\vec{X}_{LKr}$ and $\vec{X}_{Vertex}$ are the 3-dimensional positions of the LKr cluster and of the vertex between the track and the beam axis, and E_{LKr} is the energy associated to the cluster. The 4-momentum of the neutral pion is the sum of the two gamma momenta:

$$P_{\pi^0} = P_{\gamma_1} + P_{\gamma_2} \tag{6.5}$$

The distribution of the reconstructed invariant mass is shown in Figure 6.6. Only candidates with an invariant mass compatible with the nominal π^0 mass of 135 MeV/c^2 [12] within 10 MeV/c^2 are selected as well-reconstructed π^0.

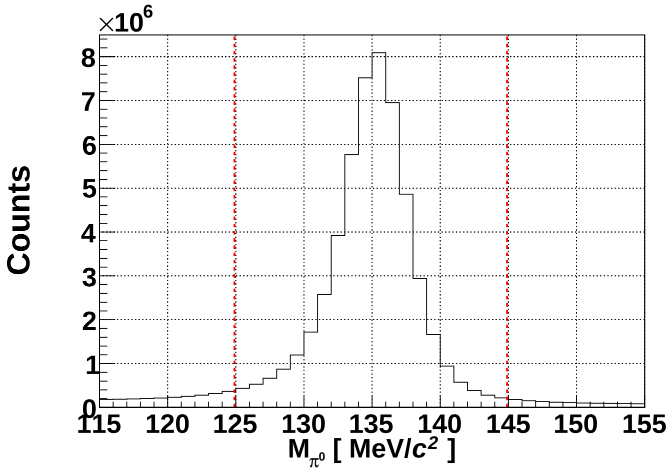

Figure 6.6 – Invariant mass of the reconstructed π^0 candidates. The red lines shows the cut values. Data for the training samples construction after the track matching with the downstream detectors. All trigger masks are included.

6.1.4 Common Requirements for the Selection of Kaon Decays

The reconstruction of any kaon decay (with only one track in the final state) begins with some common requirements on the event topology.

The reconstructed vertex position is required to be inside the fiducial volume. The definition of the fiducial volume varies in case the vertex is reconstructed using as kaon direction the nominal beam parameters (beam axis) – like in Section 5.3.2 and 5.3.1 – or the matched track in the GTK as described in Table 6.3.

	x [mm]		y [mm]		z [m]		CDA [mm]
	min	max	min	max	min	max	
GTK	−50	150	−20	20	105	165	$< 30^*$
Beam axis	−50	150	−20	20	120	165	< 30

* this cut is not effective due to the GTK resolution and may be tightened to 3 mm.

Table 6.3 – Fiducial region definitions.

The event is then required to have a tagged kaon and no in-time beam activity detected by the CHANTI.

Figure 6.7 shows how the distribution of the squared missing mass changes between the initial single track selection (a), applying the fiducial region cuts (b), and the kaon identification (c) in a minimum bias sample (Control Trigger). The two leading kaon decays, $K_{\mu 2}$ and $K_{2\pi}$, are clearly visible. The requirements on the decay vertex and on the kaon identification allows to strongly suppress the background due to elastic scattering of beam particle on the last station of the GTK (orange) and from beam pions decaying into muons (red).

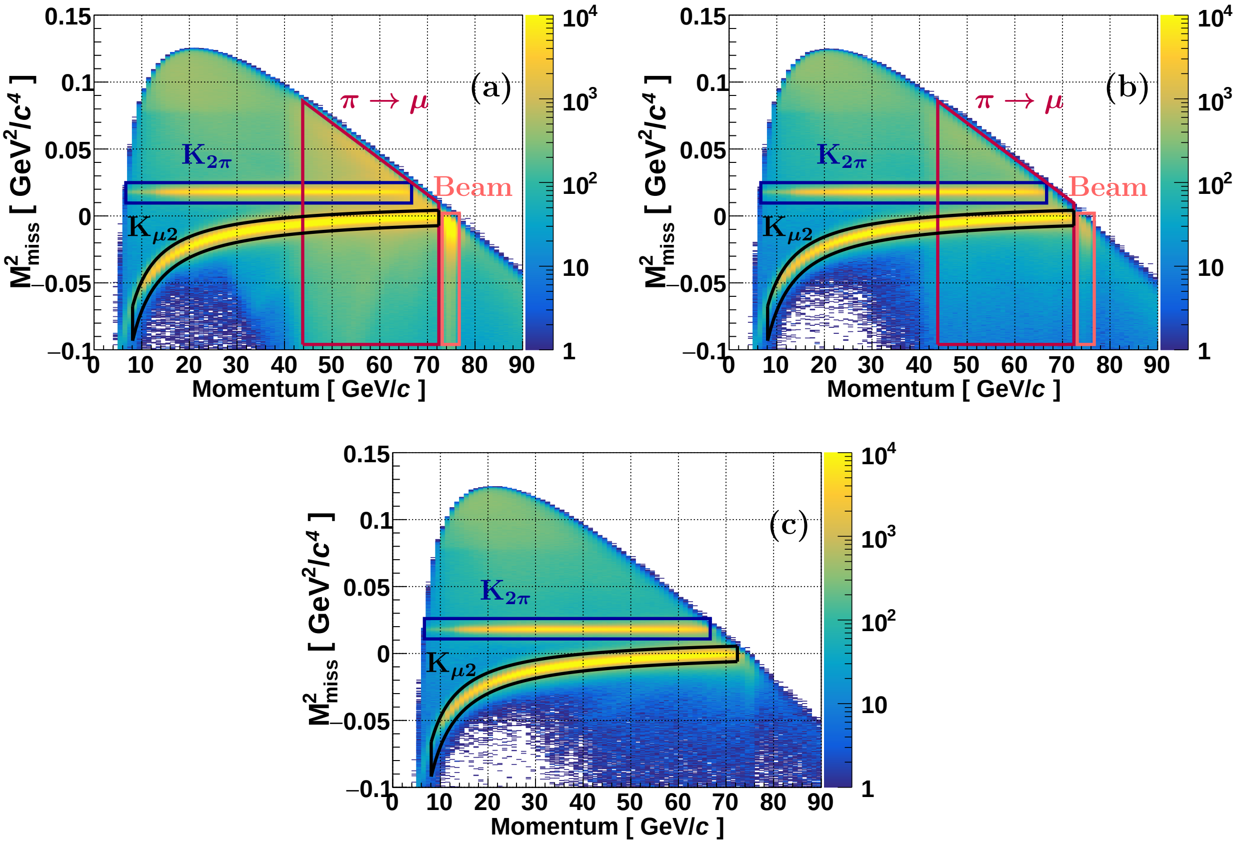

Figure 6.7 – Distribution of M^2_{miss} (evaluated using the GTK information) as function of the track momentum: after the single track selection (a), requiring the vertex inside the fiducial region (b) and with the kaon identification (c). The main kaon decays as well as the beam pions decay and scattering on the last GTK station are shown by coloured boxes.

6.2 Muons

The selection of a pure muon sample is based on the reconstruction of $K^+ \to \mu^+\nu_\mu$ ($K_{\mu 2}$) events. The signature of the $K_{\mu 2}$ decay is the presence of only one detectable particle in the final state, the muon. The first step of the selection, after the pre-selection described in Section 6.1.4, is therefore the rejection of events with signals in any of the photon veto detectors.

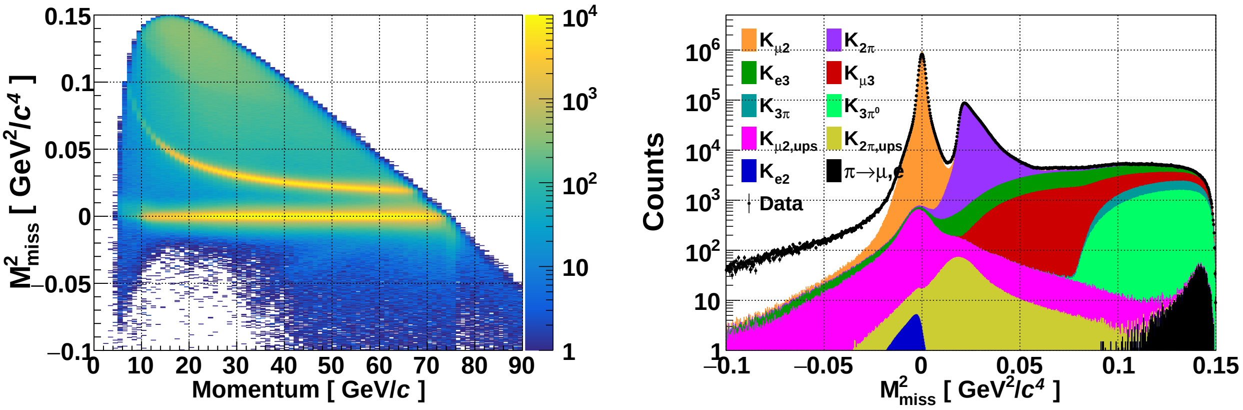

Figure 6.8 – Distribution of squared missing mass (M^2_{miss}) under the $K_{\mu 2}$ assumption at the beginning of the selection: on the left as function of the track momentum, on the right comparison with MC simulation.

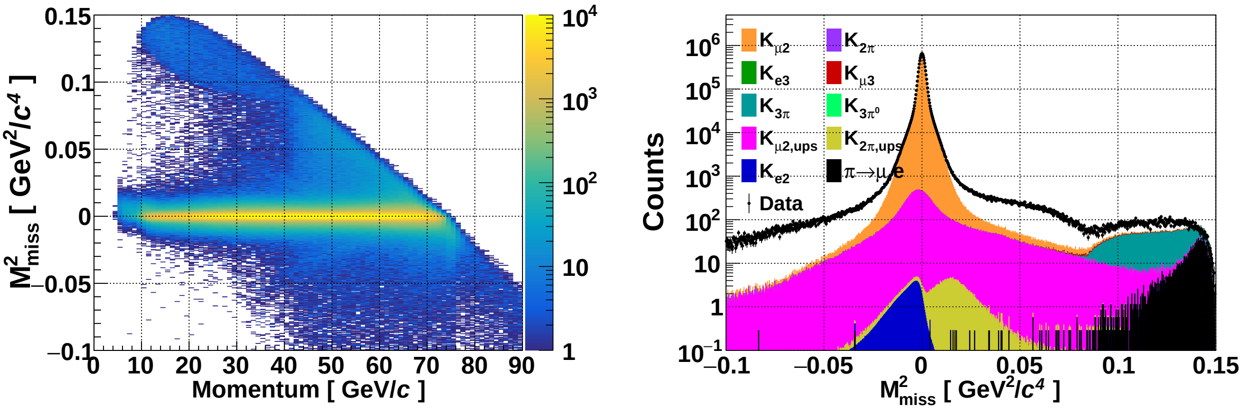

Figure 6.9 – Distribution of M^2_{miss} in the muon hypothesis after rejecting events with signals in any of the photon veto detectors. On the left as function of the track momentum. On the right comparison with MC simulation.

Figures 6.8 and 6.9 show the distributions of the squared missing mass in the muon track assumption ($M^2_{miss} = (P_K - P_\mu)^2$) at the beginning of the selection (equivalent to Figure 6.7 (c)) and after the photon veto together with the comparison with MC simulation. The simulation includes all major kaon decays in the fiducial region, $K_{\mu 2}$, $K_{2\pi}$, K_{l3} ($K^+ \to \pi^0 l^+ \nu_l$ with $l = e, \mu$), K_{e2} ($K^+ \to e^+ \nu_e$), $K_{3\pi}$ and $K_{3\pi^0}$, as well as $K_{\mu 2}$ and $K_{2\pi}$ decays upstream the last GTK station and the decay of beam pions. The disagreement between data and Monte Carlo is related to an erroneous matching with a GTK track due to beam particles crossing the detector close in time.

The main sources of non-muon background in the samples are from K_{e2} and upstream $K_{2\pi}$ decays. A better discrimination of these decay channels can be achieved by reconstructing the invariant muon mass squared. The missing momentum in signal events is carried by the neutrino, whose 4-momentum P_ν is, therefore, given by the difference between kaon and muon track three-momenta, assuming the neutrino massless. The squared muon mass in the assumption of a $K^+ \to \mu^+ \nu_\mu$ decay is hence:

$$m_\mu^2 = (P_K - P_\nu)^2 \tag{6.6}$$

Requiring the reconstructed m_μ^2 to be compatible within $0.004\,\mathrm{GeV}^2/c^4$ with the squared nominal mass ($0.0129\,\mathrm{GeV}^2/c^4$ [12]) allows to strongly reduce the background in the muon sample as shown in figure 6.10.

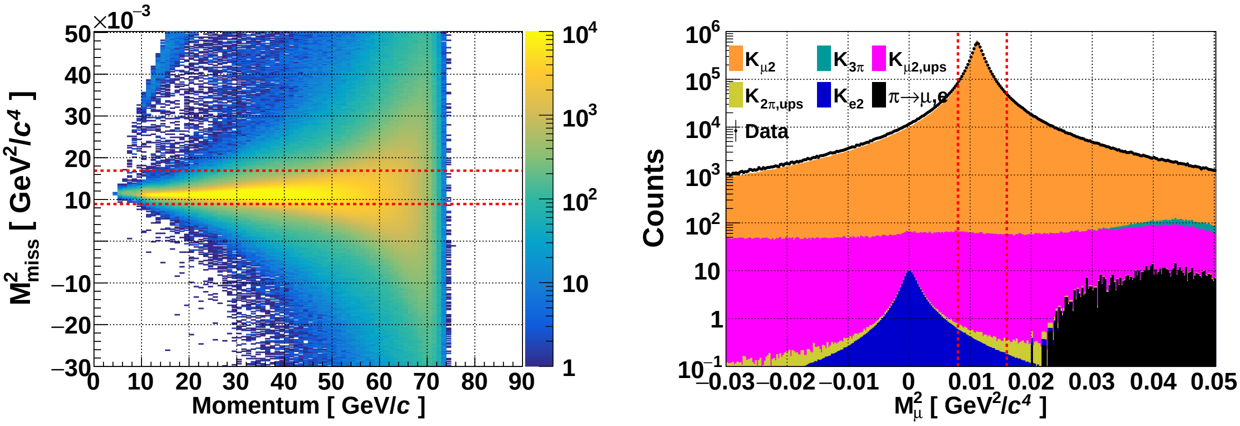

Figure 6.10 – Reconstructed muon mass as function of the track momentum (left) and comparison with Monte Carlo simulation (right). The red lines indicate the cut values.

The composition of the sample at this stage of the selection is reported in Table 6.4. The largest amount of spurious events comes from $K_{\mu 2}$ decays upstream of the GTK, adding however muons to the sample and do not need to be considered as background.

The most relevant background sources – processes leading in the final state to a non-muon track – are the K_{e2} and the upstream $K_{2\pi}$ decays, accounting in total for about 2×10^{-6} of all the events.

Decay	Generated MC ($\times 10^6$)	Selected MC	Content
$K_{\mu 2}$	81.8	29.1×10^6	~ 1
$K_{\mu 2,ups}$	195.6	42882	$(2.65 \pm 0.01) \times 10^{-4}$
K_{e2}	19.4	201767	$(1.465 \pm 0.003) \times 10^{-6}$
$K_{2\pi,ups}$	100.1	1124	$(7.3 \pm 0.2) \times 10^{-7}$
$K_{2\pi}$	64.7	8	$(1.1 \pm 0.4) \times 10^{-7}$
$K_{3\pi}$	40.7	5	$(3.0 \pm 1.4) \times 10^{-8}$
$K_{\mu 3}$	18.4	2	$(1.6 \pm 1.1) \times 10^{-8}$
K_{e3}	36.6	1	$(6 \pm 6) \times 10^{-9}$

Table 6.4 – Composition of the $K_{\mu 2}$ sample after the m_μ^2 cut.

The RICH efficiency to detect (or reject) muons, shown in figure 6.3, is estimated at this stage of the selection.

The last step of the selection is the particle identification with the RICH. The test sample is at this point completely defined and contains more than 1.8×10^6 selected events. The training sample is, instead, cleared from muons leaving signals in the MUV3. This operation does, almost, not reduce the background, but remove a large fraction of the muons. However, the remaining muons are those that the calorimeters are supposed to reject.

The analysis of control trigger events for the training sample counts only 1.5×10^5 selected events. In order to achieve a sufficient statistics the data collected with the physics trigger masks 0 and 1 are also included, resulting in a total of 3×10^6 selected muons. The momentum spectrum of the muons in the training sample is shown in fig 6.11 for events in the the Control (left) and and the Physics (right) trigger streams. The drop around 50 GeV/c in the physics trigger data is related to the STRAW algorithm applied at the L1 trigger (see Section 4.2.2). The contamination of the train and test samples has been estimated to be below 10^{-6} and 10^{-5} respectively, as reported in Table 6.5.

Background	Test Sample	Training Sample
Electrons (K_{e2})	$(5.52 \pm 0.02) \times 10^{-7}$	$(3.3 \pm 0.9) \times 10^{-5}$
Pions ($K_{2\pi,ups}$)	$(2.99 \pm 0.15) \times 10^{-7}$	$(4.5 \pm 0.8) \times 10^{-5}$

Table 6.5 – Background contribution to the muon training sample with data from control trigger only.

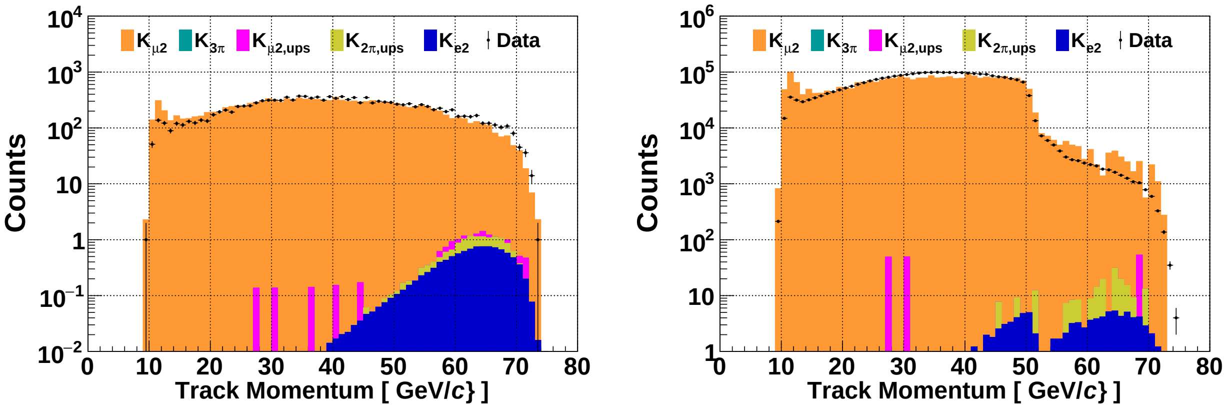

Figure 6.11 – Composition of the muon sample after the MUV3 veto as function of the track momentum. On the left for events in the control trigger stream, on the right for those in the physics trigger.

6.3 Pions

The selection of the pion sample is based on the reconstruction of $K_{2\pi}$ events. This process is a two-body decay whose final state can be fully reconstructed in NA62. The selection starts from the common requirements for a kaon decay described in Section 6.1.4. Figure 6.12 shows the distribution of M^2_{miss} in the pion-track assumption and its composition from MC simulation.

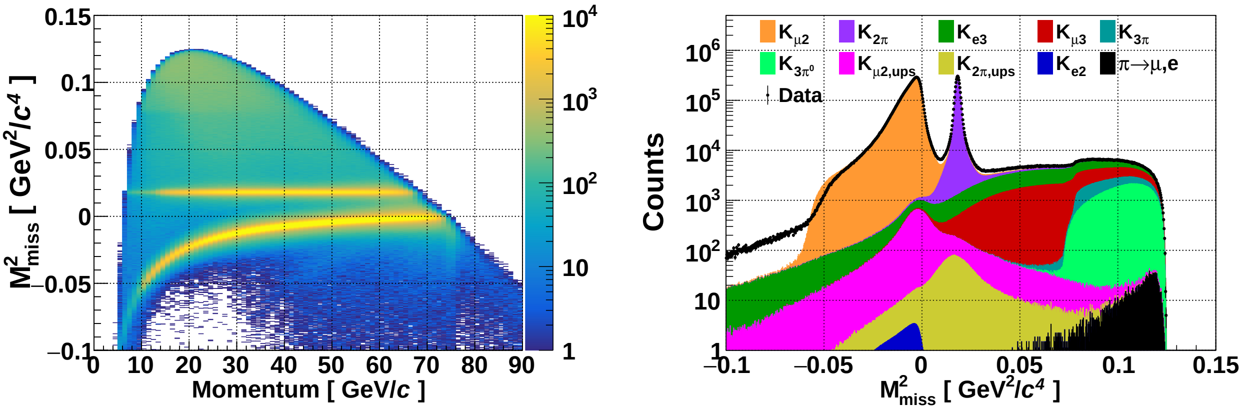

Figure 6.12 – Distribution of invariant missing mass M^2_{miss} after the common kaon decay requirements (6.1.4) on the left as function of the track momentum, on the right comparison with MC simulation.

The first stage of the selection performs the topological reconstruction of the event requiring: one track, one neutral pion and nothing else. Therefore, events with exactly one well-reconstructed π^0 and no signal in any of the large and small angle vetoes – LAV and SAV – are selected.

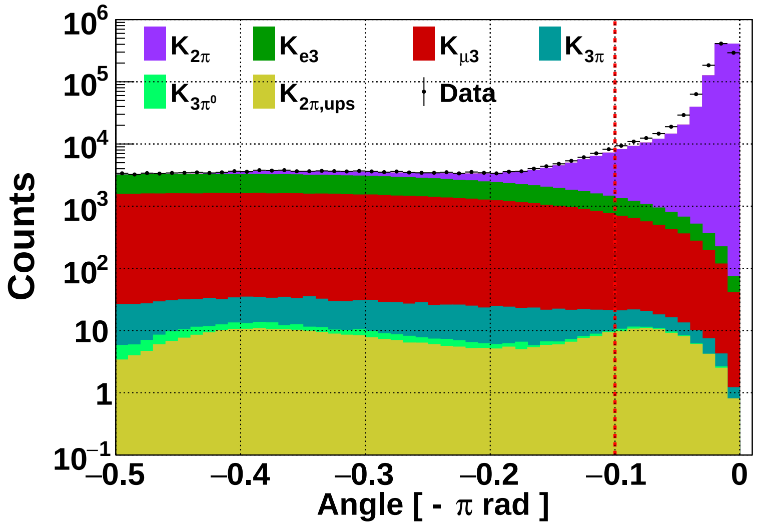

Figure 6.14 – Angle (minus π) between π^+ and π^0 in the kaon rest frame. The red line identifies the cut value.

Figure 6.13 shows the effect of this requirements: $K_{\mu2}$, K_{e2}, and beam pions decays are practically fully rejected.

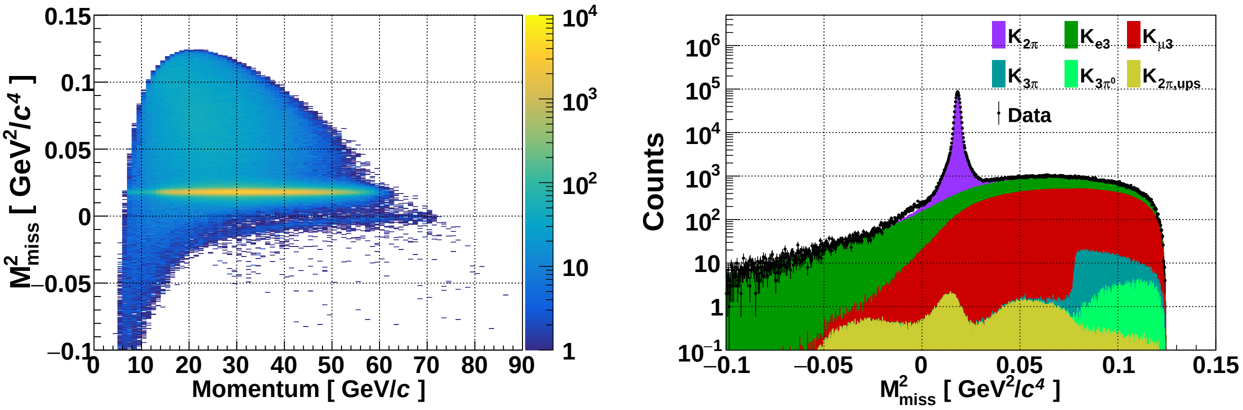

Figure 6.13 – Distribution of M^2_{miss} after requiring the topological reconstruction of the event. On the left as function of the track momentum. On the right comparison with MC simulation.

The following step of the selection verifies the consistency of the kinematic variables with the $K^+ \to \pi^+\pi^0$ decay. The π^+ and the π^0 are required to be emitted back-to-back (within 100 mrad) in the kaon rest frame (Figure 6.14). The reconstructed kaon four-momentum, $P_K = P_{\pi^+} + P_{\pi^0}$, is then required to be compatible with the one measured with the GTK ($|\vec{p}_K|$ within 2 GeV/c and $p_\perp$ within 20 MeV/c) and with an invariant mass within 20 MeV/c^2 of the nominal kaon mass of 493.7 MeV/c^2 [12]. Figure 6.15 shows the distribution of M^2_{miss} after these requirements on the kinematics. The sample composition at this stage of the selection is reported in Table 6.6.

Decay	Generated MC ($\times 10^6$)	Selected MC	Content
$K_{2\pi}$	64.7	9.44×10^{-6}	~ 1
K_{e3}	36.6	21603	$(9.90 \pm 0.07) \times 10^{-4}$
$K_{\mu 3}$	18.4	15687	$(9.48 \pm 0.08) \times 10^{-4}$
$K_{2\pi,ups}$	100.1	11271	$(5.43 \pm 0.05) \times 10^{-5}$

Table 6.6 – Composition of the $K_{2\pi}$ sample.

The RICH efficiency in selecting (rejecting) pions is estimated at this stage of the selection. The pion sample is further refined to reject background from K_{e3} and $K_{\mu 3}$ decays by requiring the pion identification with the RICH. The only sizeable contamination of the final sample is from electrons and is estimated as $(1.0 \pm 0.2) \times 10^{-6}$.

About 2.5×10^5 pions are selected for the test sample. The train sample, composed of data from control and physics mask 0 trigger streams, counts 2.6×10^6 pions.

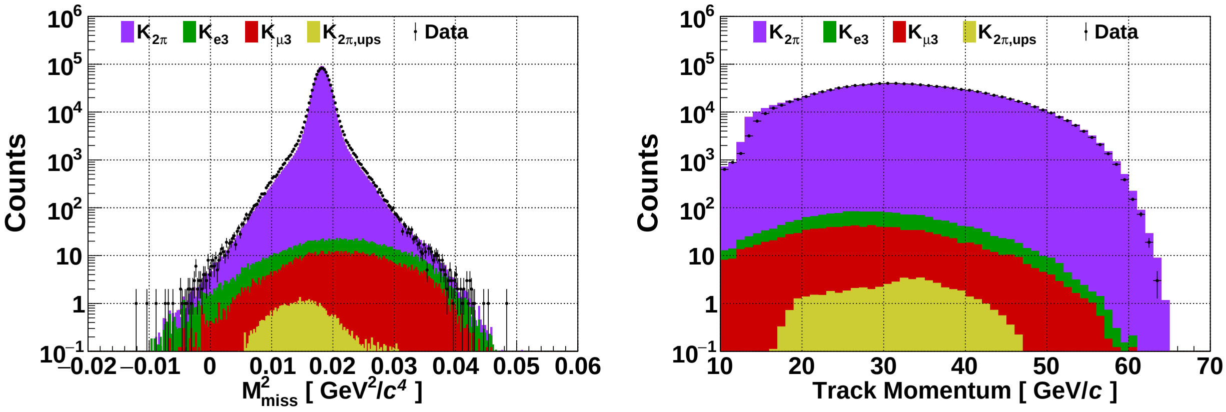

Figure 6.15 – Composition of the pion sample: as function of the invariant missing mass (M^2_{miss}) on the left and of the track momentum on the right.

6.4 Electrons

The selection of a pure electron sample is based on the reconstruction of K_{e3} decays. The initial stages of the selection are common to the selection of the pion sample. Since the topology – one track, a reconstructed π^0 and nothing else – is identical for the two processes.

In order to suppress muons from the $K_{\mu 3}$ decay, events with signals in MUV2 and MUV3 are rejected. The requirement on the MUV2 – whose information are then included in the training process – does not bias the training sample: the total material budget of LKr and MUV1 accounts for about 60 radiation lengths X_0, therefore the probability that an electron reaches the MUV2 is absolutely negligible.

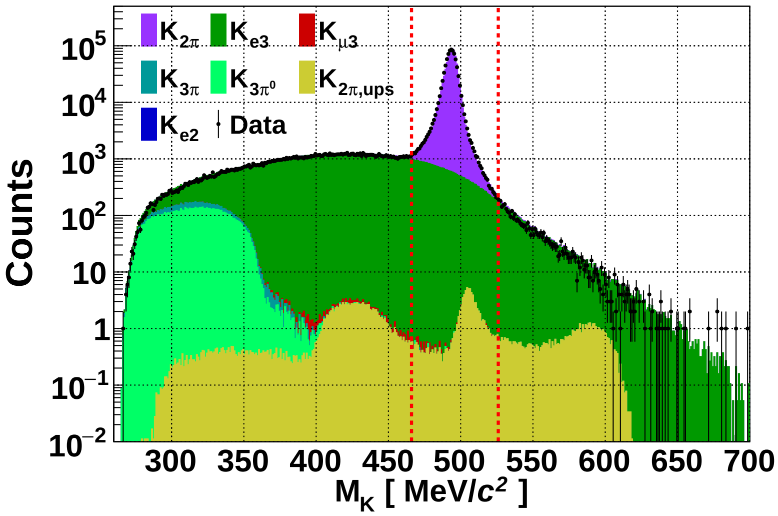

Figure 6.16 – Reconstructed Kaon mass in the hypothesis of $K^+ \to \pi^+\pi^0$ event. The red lines highlight the cut values.

The selection is refined by applying constraints to the reconstructed event kinematics. The kaon mass, reconstructed in the $K^+ \to \pi^+\pi^0$ assumption, is required to be at least 30 MeV/c^2 away from the nominal value [12] (Figure 6.16). The sum of track and π^0 momenta is then required to be lower in module by at least 5 GeV/c and up to 40 GeV/c respect to the GTK measurement, and with a transverse component mismatch of at least 30 MeV/c.

Figure 6.17 (left) shows the distribution of the kinematic variable $M^2_{3\pi^0} = (P_K - P_{\pi^0} - P_{\pi^+})^2$, describing the squared missing mass in the assumption of a $K^+ \to \pi^+\pi^0 X$ decay. The peak at the squared neutral pion mass shows a relevant background contribution of pions from the $K_{3\pi^0}$ decay.

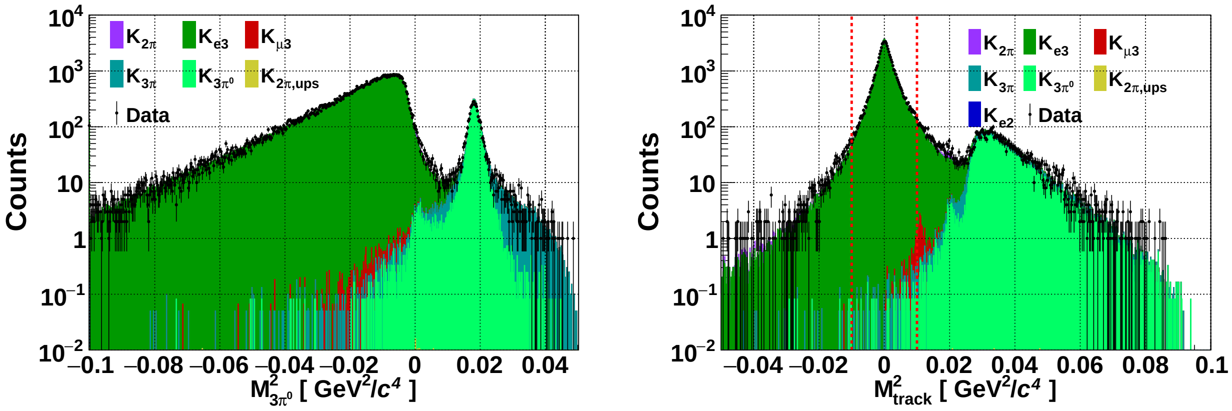

Figure 6.17 – Distribution of $M^2_{\pi^0}$ (left) and M^2_{track} (right) with background contribution from MC simulation. The red lines show the selection cuts.

Better handling of this and of the others backgrounds in the sample is provided by the reconstruction of the track squared mass. In the assumption that the missing momentum, $\vec{p}_{miss} = \vec{p}_k - \vec{p}_{track} - \vec{p}_{\pi^0}$, is carried by a massless particle, the neutrino, the squared invariant mass of the particle is $M^2_{track} = (P_K - P_{\pi^0} - P_{miss})^2$. Figure 6.17 shows the distribution of M^2_{track}. The request $|M^2_{track}| < 0.01$ GeV$^2/c^4$ results in the sample composition reported in Table 6.7.

Decay	Generated MC ($\times 10^6$)	Selected MC	Content
K_{e3}	36.6	1.35×10^6	~ 1
$K_{2\pi}$	64.7	238	$(4.09 \pm 0.26) \times 10^{-4}$
$K_{\mu3}$	18.4	80	$(7.9 \pm 0.9) \times 10^{-5}$
$K_{3\pi^0}$	7.8	80	$(5.9 \pm 0.7) \times 10^{-5}$
$K_{3\pi}$	40.7	38	$(4.6 \pm 0.8) \times 10^{-5}$

Table 6.7 – Composition of the background to the K_{e3} sample after kinematic requirements.

The RICH electron selection (rejection) efficiency is evaluated at this point of the selection. The selection is finalized by requiring $M^2_{miss} > 0.025$ ($K_{2\pi}$ and the RICH electron identification. The contamination of the sample is estimated to be below 5×10^{-5}, almost equally divided between muons ($(1.9 \pm 0.8) \times 10^{-5}$) and pions ($(2.5 \pm 0.8) \times 10^{-5}$).

The test sample counts 15×10^4 selected electrons. In order to achieve a sufficient statistics the training sample is selected using data in the control and mask 1 trigger streams. Figure 6.18 shows the momentum spectrum for events selected in the control (left) and in the physics trigger (right). The simulation fails to reproduce the physics trigger effect due to a defect in the LKr L0 firmware (see Section 4.2.1).

The background estimate is therefore performed with a data-driven method.

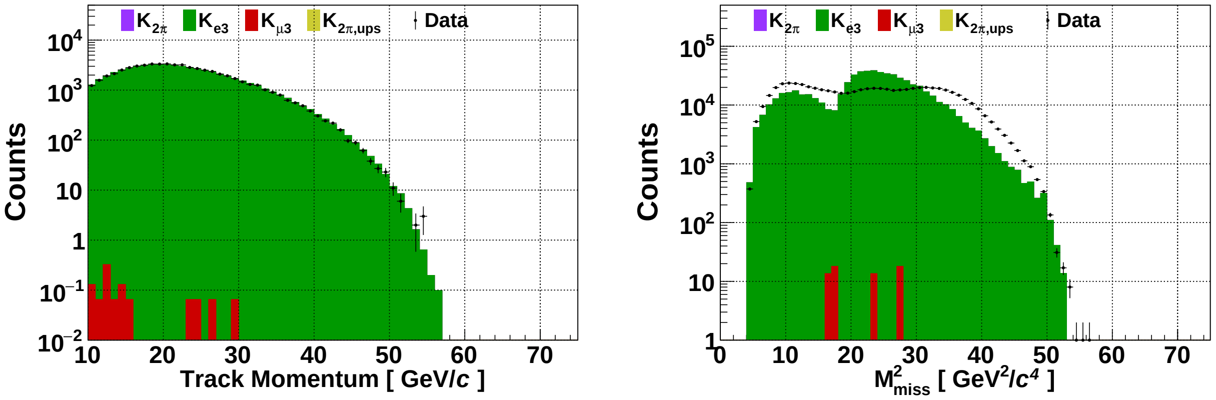

Figure 6.18 – Distribution of the track momentum for events passing all the selection requirements in the data collected by the control (left) and the physics trigger (Mask 1, right).

6.4.1 Data-driven Estimation of the Background

The main sources of background to the electron sample are decays with the same topology as the signal: one track and one reconstructed π^0. However, the energy degradation in the LKr follows different processes for muons, pions and electrons, Therefore the physics trigger is expected to affect differently K_{e3}, $K_{\mu3}$, and $K_{2\pi}$ events. The pion and muon contamination of the electron sample selected from the trigger mask 1 is obtained weighting the results from the control trigger by the ratio of the trigger efficiencies ($K_{2\pi}/K_{e3}$ and $K_{\mu3}/K_{e3}$).

The selection stage where the squared invariant mass of the particle is evaluated (right of Figure 6.17) is used as starting point for the evaluation of the trigger efficiencies, using control trigger events. Instead of cutting on M^2_{track}, the RICH particle identification is applied to select either electrons, muons or pions, enhancing the respective signals in the M^2_{track} distribution. The trigger efficiency is then estimated verifying how many of the selected events are flagged by the L0TP as satisfying the mask 1 trigger requirements.

The evaluation of the trigger efficiency for the $K_{2\pi}$ and $K_{\mu3}$ processes requires a large amount of data since it has to be performed on the events passing most of the K_{e3} selection. The control trigger events in the complete 2016A dataset (filtered with `FilterPnn` [26]) are analysed.

The K_{e3} trigger efficiency is evaluated as $(8.11 \pm 0.06)\,\%$ based on 19781 out of 243989 events passing the trigger selection.

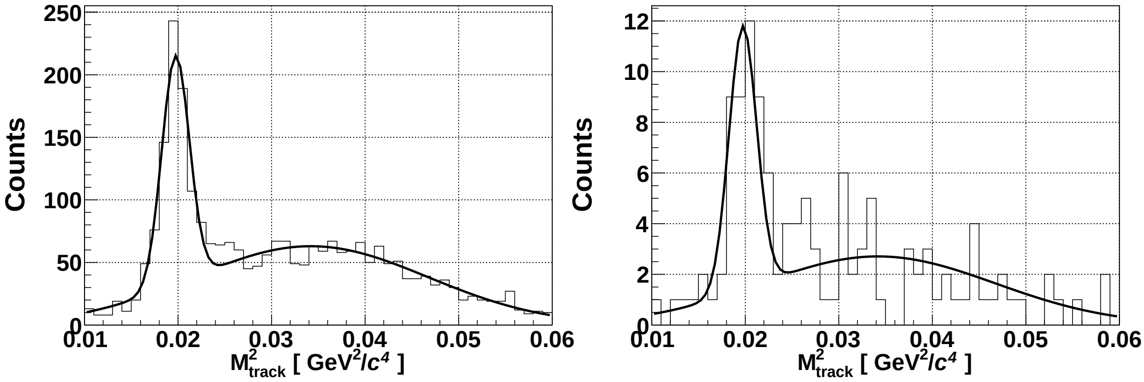

Figure 6.19 – Distribution of m^2_{track} after RICH pion identification for the determination of the mask 1 trigger efficiency for $K_{2\pi}$ events. On the left for all selected events in control trigger, on the right for those flagged also as passing the mask 1 trigger requirement.

In the estimation of the $K^+ \to \pi^+\pi^0$ trigger efficiency, the background from $K^+ \to \pi^+\pi^0\pi^0$ has to be taken into account. The distribution of M^2_{track} after the RICH pion identification is shown in figure 6.19. The distribution for the control trigger events is fitted with the sum of two gaussians, one describing the pion mass peak and the second the three pion signal. The distribution for events flagged for the physics trigger is fitted with the same two gaussians leaving only the normalization as free parameters. The trigger efficiency is therefore obtained as the ratio between the integral of the gaussians describing the $K^+ \to \pi^+\pi^0$ peak, leading to $(5.8 \pm 0.9)\,\%$.

The $K_{\mu3}$ trigger efficiency determination must take into account the background from K_{e3} events passing the RICH muon identification. The distribution of m^2_{track} in this case is shown in figure 6.20. The distribution is fitted, analogously to the $K_{2\pi}$ case, with two gaussian (one parametrizing the right side of the electrons peak and the second for the muon signal) and leaving only the normalization as free parameter in the case of events passing also the physics trigger. The trigger efficiency is estimated as $(15.3 \pm 2.2)\,\%$.

The expected contamination of the electron sample is therefore:

- Muons ($K_{\mu3}$): $(3.6 \pm 1.0) \times 10^{-5}$
- Pions ($K_{2\pi}$): $(1.7 \pm 0.6) \times 10^{-5}$

The obtained estimate is valid in the assumption that the shape of the M^2_{track} distribution is not affected by the trigger requirements. Therefore, in each background channel, the amount of events falling under the electron peak scales with those in the characteristic background mass peak equally in the control and mask 1 trigger datasets.

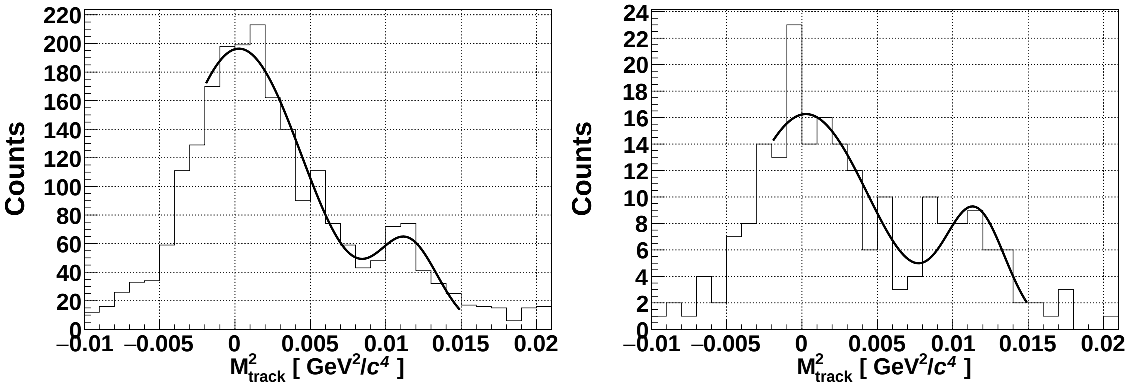

Figure 6.20 – Distribution of m^2_{track} after RICH muon identification for the determination of the mask 1 trigger efficiency for $K_{\mu 3}$ events. On the left for all selected events in control trigger, on the right for those flagged also as passing the mask 1 trigger requirement.

Chapter 7

Particle Identification with the NA62 Calorimeters

In any high energy physics experiment particle identification is one of the crucial and most challenging task. NA62 does not represent an exception. In particular the measurement of the $K^+ \rightarrow \pi^+ \nu \bar{\nu}$ branching ratio requires a muon suppression of about 10^7, to be achieved by the combined information of RICH (10^2), MUV3 (2×10^2) and calorimeters LKr and HAC (5×10^2).

A muon-pion separation factor of 500 from pure calorimetric information requires a classification of the energy deposits in the calorimeters based on the reconstructed shower shape and energy. A classic cut-and-count approach can reach the required discrimination, but at the price of a large pion inefficiency. The optimization of the cut values is, indeed, complex due to correlations among the many variables needed to describe the cascade.

In the described scenario the Boosted Decision Trees (BDT) technique provides a perfect tool to tackle the muon-pion discrimination problem efficiently. Moreover, the BDT method allows to easily extend the muon-pion separation to a particle identification task, applicable to any analysis performed in NA62.

The decays of particles in the NA62 beam and detector generate almost exclusively muon, pions and electrons (intended as both e^+ and e^-). The particle identification is hence a three-classes classification problem.

7.1 The Boosted Decision Trees Technique

Algorithms based on machine learning are acquiring a larger relevance in everyday life: from picture optimization software to digital assistants we already rely on artificial intelligence.

In physics analysis the application of machine learning is still limited, due to the difficulties in controlling the decisional path followed by such algorithms. However, classifier methods like multilayer perceptron neural networks or Boosted Decision Trees become of common use.

Several software packages provide an interface to machine learning techniques. The presented work makes use of the TMVA framework [45] (v 4.2.0 integrated in ROOT v 6.12.04 [35]).

7.1.1 Decision Trees

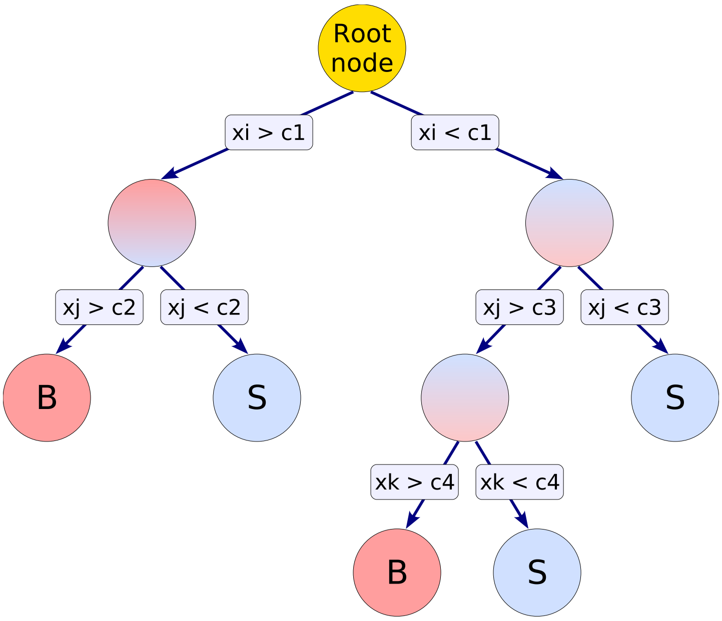

Figure 7.1 – Example of decision tree [45]. The initial sample, in the top yellow node, contains both background and signal events. The data follow different paths according to the values of the x_i, x_j, and x_k variable (compared to the cut values $c_1 ... c_4$). The destination node, called leaf, provides the event classification as background (B) or signal (S).

The Boosted Decision Trees (BDT) technique is based on the weighting of several cut analyses, called decision trees.

Decision trees (DT) are known since long time and represent probably the best representation of the human rational thinking: a complex problem, like the classification of an event as signal or background, is sub-divided in consecutively smaller tasks.
The response of a DT is evaluated as shown in Figure 7.1. Starting from a root node, the event parameters x_i, x_j, and x_k (generally referred to as discriminating variables) are compared to the reference values c_1, c_2, c_3 and c_4. The event is then routed, following the result of the comparisons, through the branches of the tree until a pure signal or pure background node, a leaf, is reached providing the event classification.
The construction of a decision tree, usually referred as training, requires a set of already classified events: the training sample. Starting from the root node the discriminating variable providing, locally, the best separation between signal and background is chosen to perform the split of the events. In an iterative procedure the splitting of the nodes proceeds until all the events end in a leaf containing only signal or background.

7.1.2 Decision Tree Forests

The very simple and intuitive development of decision trees has the drawback of being extremely sensitive to statistical fluctuation of the training sample, leading to over-fitting problems and non-reproducibility of the results. The choice of the variable providing the best signal-background separation is strongly influenced by the statistical fluctuation in the training sample, determining a completely different tree development and performance depending on the dataset employed for the training. Moreover, the development of the DT to pure signal (background) leafs is steered in some branches by a very small amount of training events that may not represent correctly the underlying signal and background characteristics. This effect is known as over-fitting: the decision tree learns to recognise patterns which are not real.
The impact of the presented instabilities of DTs can be reduced by interrupting the node splitting procedure when the amounts of events in node is too small. The leafs are not any more pure signal or background node, but the classification is defined by the dominant category.
A more effective approach to the decision tree instabilities is obtained by a simple statistical method. The classification of an event (as signal or background) can be seen as equivalent to the assessment of a physical quantity. In this perspective, the response of a DT is analogous to the outcome of a single experimental measurement. Like the precision of the final estimate improves with the number of measurements

performed, in the same way the classification of a event becomes more reliable combining the response of several different decision trees. For a large number of DTs, built with independent training samples, the impact of statistical fluctuations on the final response compensates, leading to a stable classifier. The ensemble of a large number of decision trees is usually referred to as a forest. The response of a forest is obtained as a majority vote among the decision trees.

7.1.3 Boosting: Boosted Decision Trees

The construction of a decision tree forest requires as many independent training samples as the number of trees to be built, demanding large amount of data for the training procedure.

The boosting technique allows to use a single training sample to build a decision tree forest. Limiting the growing of the single DT reduces, as previously mentioned, the over-fitting probability, but leads also to misclassified events already at the training stage. In the sequential training of the decision trees composing the forest, boosting algorithms vary the weight of the events in the training sample according to a, so-called, loss function $L(F, y)$, based on the comparison of the response of the already built trees (F) and the real classification of the event (y). The weight of misclassified events is, therefore, enhanced with respect to the one of those correctly classified, obtaining after the training of each tree a correction to the forest response. The response of each DT is then weighted, according to the boost applied to the training sample, in order to obtain the final response.

The practise of building decision tree forests exploiting boosting algorithms is generally referred to as Boosted Decision Trees (BDT) technique.

Boosting algorithms are supposed to work better with weak classifier (classification methods providing a limited separation power), the growing of decision trees in the BDT technique is therefore generally interrupted after few level of splitting.

In the following two boosting algorithm are briefly described: AdaBoost as one of the most commonly used, and the Gradient boost implemented in the TMVA package and employed in this work. The provided description is valid for the application of the boosting to any classification method, the word classifier is therefore to be intended as decision tree in the BDT case.

AdaBoost One of the most common algorithm for boosting is the Adaptive Boost (AdaBoost), which is represented by the loss function:

$$L(F, y) = e^{-F(\vec{x})y} \tag{7.1}$$

where $\vec{x}$ represents the vector of discriminating variables in an event, $F(\vec{x})$ is the classifier and y the label – signal $(+1)$ or background (-1) – of the tested event. The concept behind this algorithm is to correct the misclassification error of the trained classifier in the next iterations by increasing exponentially, e^{α_i} where $\alpha_i = -F(\vec{x}_i)y$ is called boosting factor, the relevance of misclassified events and contemporary reducing it for those correctly classified.

In this algorithm the weight of a classifier i in the final decision is determined by the classification error $(1-\epsilon)$ of the previous $i-1$ as:

$$W_i = \ln\left(\frac{1-\epsilon_{i-1}}{\epsilon_{i-1}}\right) \tag{7.2}$$

The AdaBoost algorithm allows to construct strong classifier, but is significantly sensitive to the contamination of the training sample. Indeed, background events in the signal training sample (and vice versa) obtain quickly very large weights driving the training process.

Gradient Boost The weakness of the AdaBoost algorithm in presence of contamination in the training sample can be cured by using a different loss function. The TMVA package provides a boosting algorithm for decision trees based on the binomial log-likelihood loss function:

$$L(F,y) = \ln(1 + e^{-2F(\vec{x})y}) \tag{7.3}$$

which is supposed to achieve performance equivalent to the Adaptive Boosting beside improving the robustness against mislabelled events.

The boost of the loss function in Equation 7.3 is obtained using the Functional Gradient Descendent technique (a complete description of the Functional Gradient Descendent technique and boosting in general can be found in [46]).

The TMVA implementation of this method trains each tree as a regression tree. Instead of the signal or background classification, the tree is trained to provide as response a value of log-likelihood for each event. Each tree is expected to correct the log-likelihood estimate provided by the preceding, having as target response for an event the difference between the (normalized) sum of the trained trees and the expected result for the considered event $(+1$ for signal and -1 for background). The response of the final classifier is then provided by the sum of the single tree log-likelihoods, normalized in the range $[-1, 1]$.

Multiple category classification The Gradient Boost of decision trees implemented in the TMVA package provides, also, a simple extension of the classification to an arbitrary number of categories (MultiClass analysis). The classification of events in to a number N of categories is subdivided in N signal-background discrimination tasks. The probability of an event to belong to each of the tested classes is obtained as the likelihood of the single discrimination analysis – exponential of the sum of each tree log-likelihood output – normalized to the likelihood of all the analysis.
The MultiClass analysis is used for the development of the particle identification algorithm.

7.2 Basics of Electromagnetic and Hadronic Showers

The interactions of muons, pions and electrons with matter involve different processes, each with its own peculiarity. As leptons, muons and electrons interact only electromagnetically, leading to ionization and electromagnetic cascades. Pions, instead, induce mostly hadronic showers dominated by QCD and nuclear processes.
In the following a short description of electromagnetic and hadronic shower development and characteristics is provided.

7.2.1 Electromagnetic Showers

The development of electromagnetic cascades follows few well-known processes. High energetic particles interact mainly through Bremsstrahlung ($e^{\pm} \to e^{\pm}\gamma$) and pair production ($\gamma \to e^{+}e^{-}$). At lower energies charged particles ionize and produce thermal excitation of the crossed material, through the collision with the atoms and the molecules. Photons, instead, loose energy through the photoelectric effect and the Compton scattering.
Two important parameters in the description of electromagnetic showers are the critical energy ϵ and the radiation length X_0. The critical energy ϵ for a charge particle in matter is defined as the energy at which the ionization and the bremsstrahlung cross sections are equal. The radiation length X_0 represents the mean path between two interactions travelled by an electron in material.
In a simplified model a shower of an electron with energy $E \gg \epsilon$ starts with the emission of a bremsstrahlung photon of energy $E/2$ at the first radiation length X_0

of the material. At a depth of $2X_0$ the initial electron produces a second photon and the previously emitted γ converts into an electron-positron pair. The particle content of the shower therefore increases by a factor two after each X_0 until the particle energies fall below the critical energy (where the energy is lost mostly by ionization and photoelectric/Compton scattering). The maximum population of the shower is reached at a depth of $X_0 \log_2 (E/\epsilon)$.

The transverse size of the shower is determined by multiple scattering of the produced electrons and positrons at the high energy regime and by photons and electrons emitted in photoelectric and Compton scattering events (isotropic emission processes). The Molière radius, defined as the ratio X_0/ϵ between the radiation length and the critical energy for electrons, describes the radius of a cylinder containing 90% of the shower energy. Molière radii for absorber materials used in calorimeters are typically of a few cm. Electromagnetic cascades are therefore quite narrow and the lateral shape does not depend on the energy of the incident particle.

The large difference in mass between muons and electrons reflects in the critical energy. The critical energy for electrons in iron is 21.68 MeV, while for muons is 347 GeV [12]. Muon interactions at energy scales used in NA62 ($[10, 75]$ GeV/c) are hence dominated by ionization processes. However electromagnetic cascades can be induced by the emission of a bremsstrahlung photon carrying a large fraction of the muon energy or by direct pair production ($\mu^\pm \to \mu^\pm e^+ e^-$). Figure 7.2 shows the cross sections for different energy loss processes as function of the fraction of energy transfer and for different muon energies.

7.2.2 Hadronic Showers

Hadronic cascades develop via the strong interaction, leading to the production of a large number of hadronic shower particles and to the breaking of the nuclear bindings within the atoms.

A large fraction of the hadrons produced in a hadronic shower are pions. Hadronic processes are charge independent, therefore in average the same amount of π^+, π^-, and π^0 is produced. While charged pions induce further hadronic interactions, π^0s decay almost instantaneously into two photons, which start electromagnetic cascades. Since the cross section for hadron production increases with energy, the average amount of energy transferred from the hadronic to the electromagnetic regime also increases with the incident particle energy.

The energy remaining in the hadronic domain is then released by slow protons and neutrons through ionization, scattering, thermal excitation, or lost in breaking nuclear bindings or late photo-nuclear emissions.

Analogously to the radiation length for electromagnetic cascades, the interaction length (λ_i) describes the mean free path of a hadron produced in a shower. The amount of material in units of λ_i needed to contain a shower depends logarithmically on the energy. However, since the scale of λ_i is considerably larger than X_0 (in iron $\lambda_i \sim 10X_0$), hadron showers extend over a much larger volume.

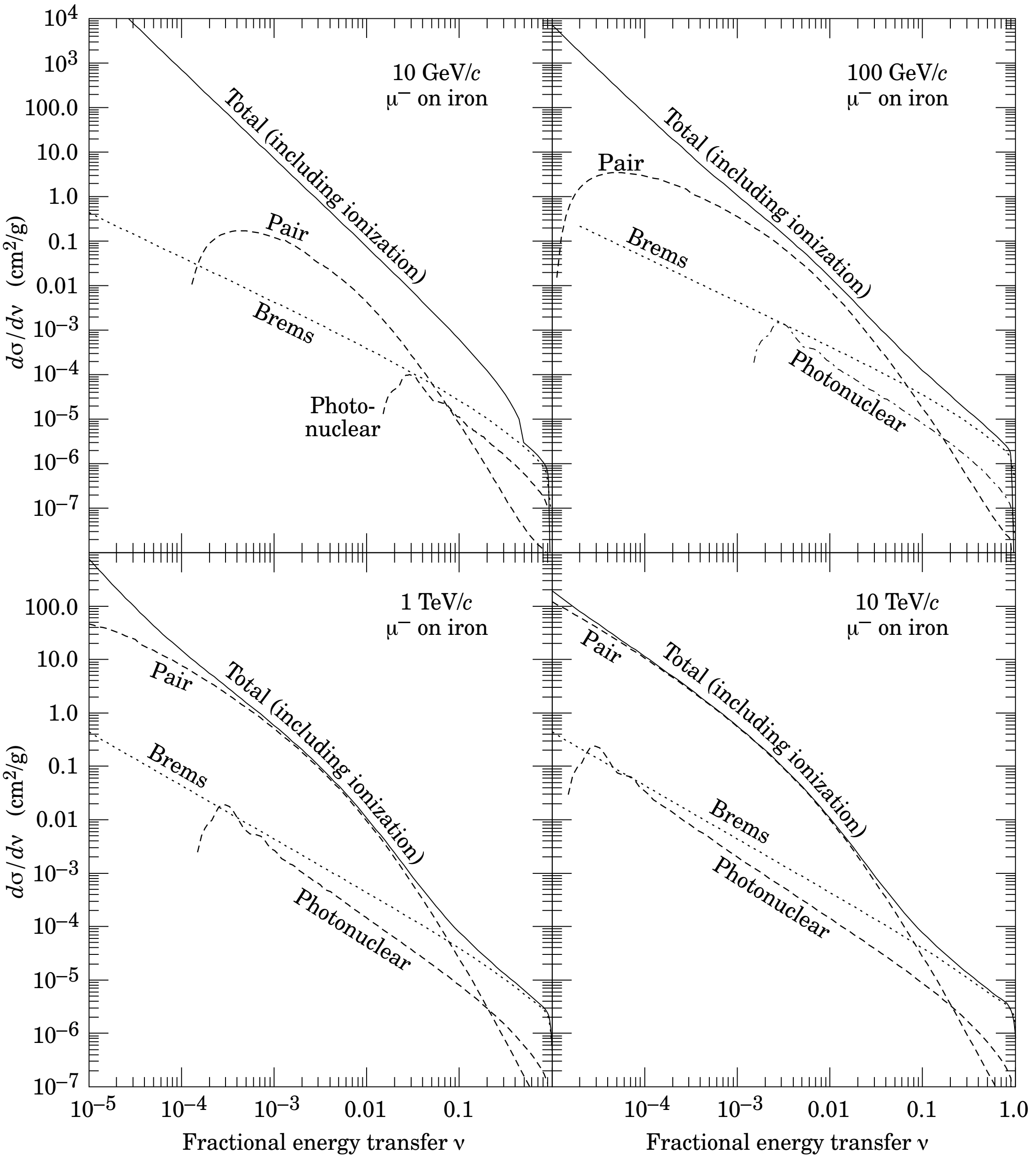

Figure 7.2 – Cross sections of different energy loss processes for different muon energies as function of the fraction of energy transfer [40].

The lateral development of the shower is different to the electron case and dependent on the energy: cascades from high energy hadrons have a larger electromagnetic contribution, resulting in narrower showers. Since the width of the shower is correlated with the mean free path, hadron cascades are significantly wider than electromagnetic showers.

7.3 Discriminating Variables

The variables employed in the particle identification are chosen by taking into account the characteristics of electromagnetic and hadronic showers.
Different aspects of the cascade reconstructed in the calorimeters are considered:

- the ratio E/p between the energy in the calorimeters and the track momentum measured by the STRAW.
- the longitudinal development of the showers.
- the transverse shape of the energy deposits.
- the distance between track extrapolation and the reconstructed shower position.

Some of these shower characteristics, like the longitudinal and transverse development of the shower, have an energy dependency which could be exploited. The absolute energy deposit in the calorimeters was however not used in the BDT algorithm to avoid indirect selection of the different kinematics of different charged particles.

Ratio E/p between the energy in the calorimeters and the track momentum The comparison between energy collected in the calorimeters and track momentum measured by the STRAW is the most effective variable for the discrimination between pions, muons and positrons.
The first variable considered is the ratio between the energy collected in the LKr and the track momentum (EoP_{LKr}). Figure 7.3 (left) shows the distribution of EoP_{LKr} for the three classes of particles: electrons are concentrated in the region around $EoP_{LKr} = 1$, muons have prevalently only small fraction of the energy reconstructed with a tiny tail toward the higher energies, and pions are spread in the region $EoP_{LKr} \in [0.1, 0.8]$ with a small peak at very low energy deposits produced

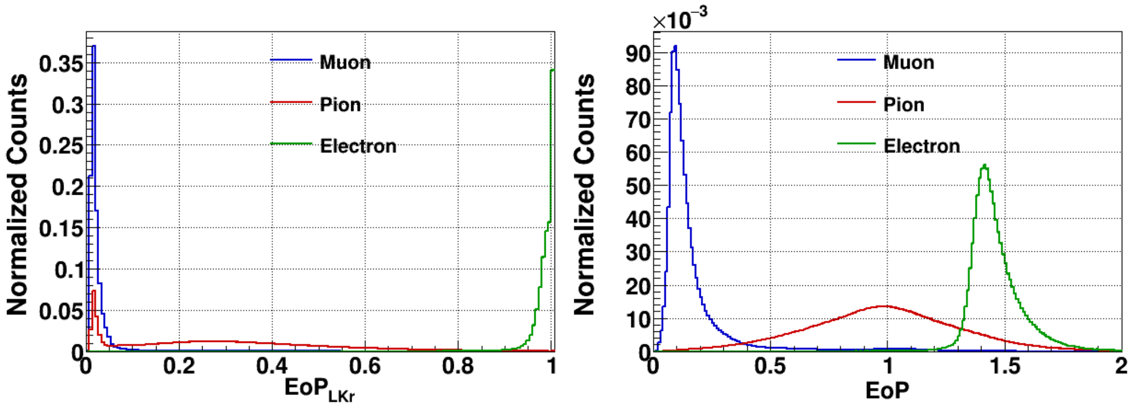

Figure 7.3 – Ratio E/p between the energy in the calorimeters and the track momentum measured by the spectrometer. On the left only the energy collected by the LKr is considered (EoP_{LKr}), while on the right the calibrated hadronic energies of LKr and HAC (EoP) is shown.

by ionization.

The second parameter considered is the ratio EoP between the total hadronic energy reconstructed in the calorimeters (LKr and HAC) and the track momentum. In this case pions distribute following a wide gaussian centered on 1, muons cover the region of lower EoP values, and positrons are shifted toward $EoP \sim 1.5$ (due to the hadronic inter-calibration between LKr and HAC) as shown on the right of Figure 7.3.

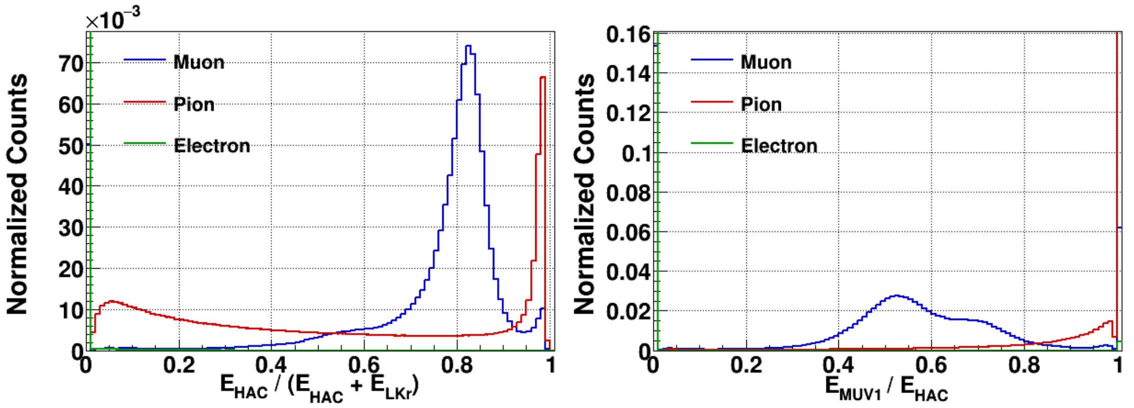

Figure 7.4 – Longitudinal development of the showers. On the left contribution of the HAC to the total energy collected in the calorimeters. On the right ratio between energy collected in the MUV1 with respect to the total energy in the HAC.

Longitudinal development of the shower The NA62 calorimeters do not provide any information about the longitudinal development of the shower inside each module. However the segmentation in electromagnetic (LKr) and hadronic (MUV1

and MUV2) sections provides a sampling of the collected energy in about 1.7, 5.2 and 8.7 interaction lengths. The sharing of the energy among the modules provides, therefore, an important discriminating variable. Positrons start showering immediately when entering the LKr and deposit, most of the time, the energy exclusively in this detector. Pion cascades extend over several interaction lengths, hence involving an energy deposit in at least two modules. Energy releases from muons beyond the ionisation happens through Bremsstrahlung and direct pair production. The cross sections for these processes is proportional to the amount of material expressed in terms of X_0. Despite the large difference in the number of interaction lengths λ_i, LKr, MUV1 and MUV2 accounts for about the same number of X_0s ($27X_0$ for the LKr and about $34X_0$ for MUV1 and MUV2). Therefore the probability that a muons generates an electromagnetic cascade is almost the same for all the the modules. The shower is then mostly contained in the module where it starts.
The variables employed in the energy sharing description are two:

- the fraction of the energy in the calorimeters collected by the HAC (on the left of Figure 7.4).
- the fraction of the HAC energy collected by the MUV1 (on the right of Figure 7.4, assumes a value of -1 in case no energy is reconstructed in the HAC).

Transverse shape of the energy deposit The transverse development of electromagnetic and hadronic cascades is very different. Electromagnetic showers are easily predictable and present a characteristic narrow gaussian-like shape. Hadron cascades, instead, have a wider lateral extension with an exponential fall from the center to the side of the shower. The large fluctuation in the amount of energy released electromagnetically reflects in a large variety of shower profiles, determining also sub-structures due to displaced π^0s production.
The description of the transverse shape in the reconstructed cascade is obtained by the following variables (shown in Figure 7.5):

- **LKr:**
    - **RMS:** as defined in Equations 5.16 and 5.17, this variable describes the transversal spread of the shower.
    - **Seed-Cluster energy ratio:** the energy ratio between what recorded in the most energetic cell and what collected in the reconstructed cluster.
    - **Cells-Energy ratio:** ratio between the number of cells and the energy of the LKr cluster.

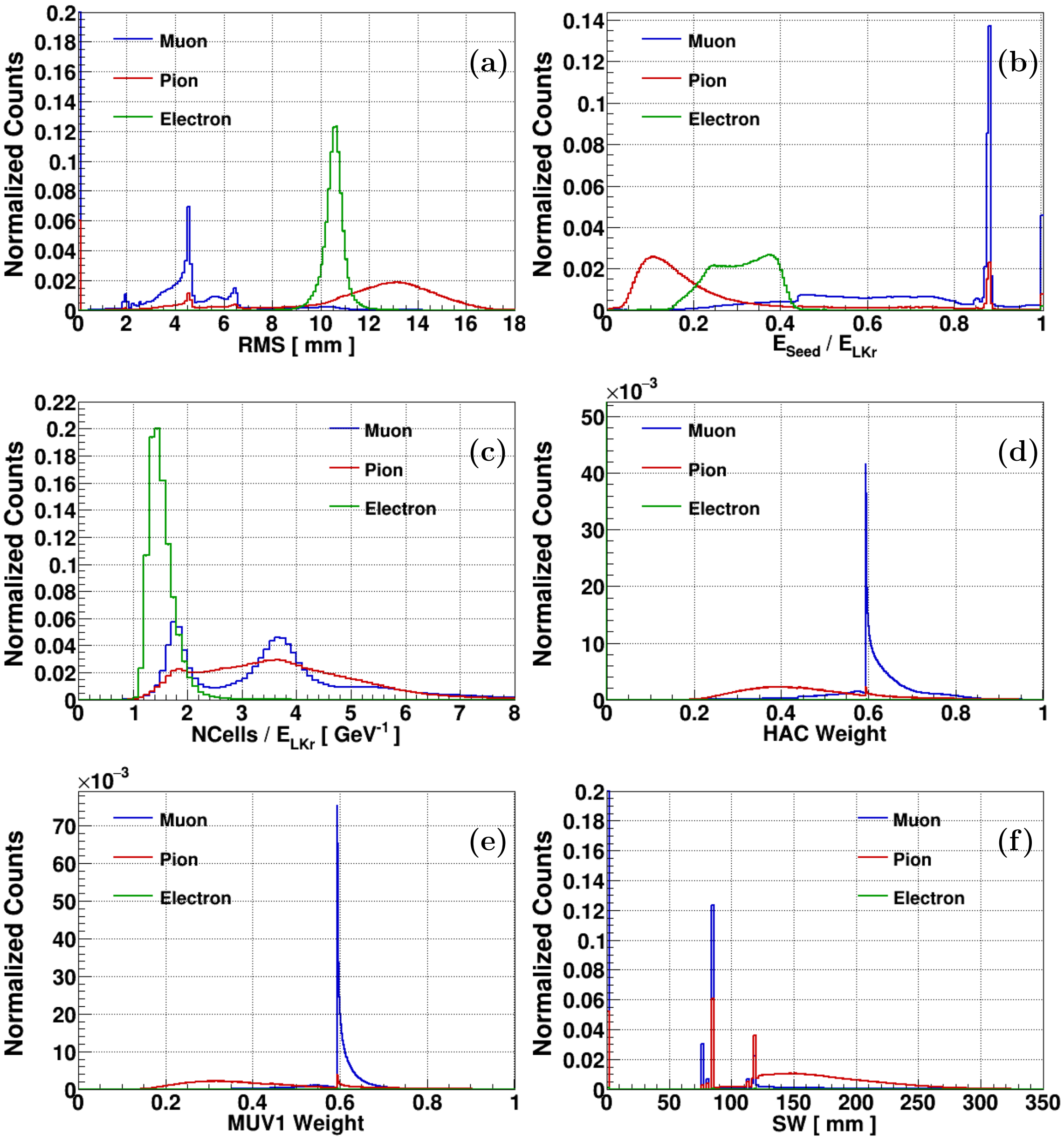

Figure 7.5 – Transverse shape of the energy deposit: (a) RMS of the LKr cluster; (b) ratio between seed and cluster energies in LKr; (c) ratio between number of cells and energy of the LKr cluster; (d) weight parameter of the HAC cluster; (e) weight parameter of the MUV1 cluster; (f) width of the shower in the HAC.

- **HAC:**
  - **MUV1 Weight:** the spread of the energies collected in the channels of the HAC front module (Equation 5.10). The variable assumes a value of −1 in case no energy is found in MUV1.
  - **HAC Weight:** extension of MUV1 weight to the complete HAC. The

definition of the variable is in Equation 5.14. The variable assumes a value of -1 in case no energy is found in any of the two HAC modules.

- **HAC Shower Width:** defined in Equation 5.7 for the MUV1. The shower width is evaluated combining the energy collected in the two modules of the HAC (following the same procedure as for the HAC Weight) and describes the lateral spread of the shower. The variable assumes a value of -1 in case no energy is found in any of the two HAC modules.

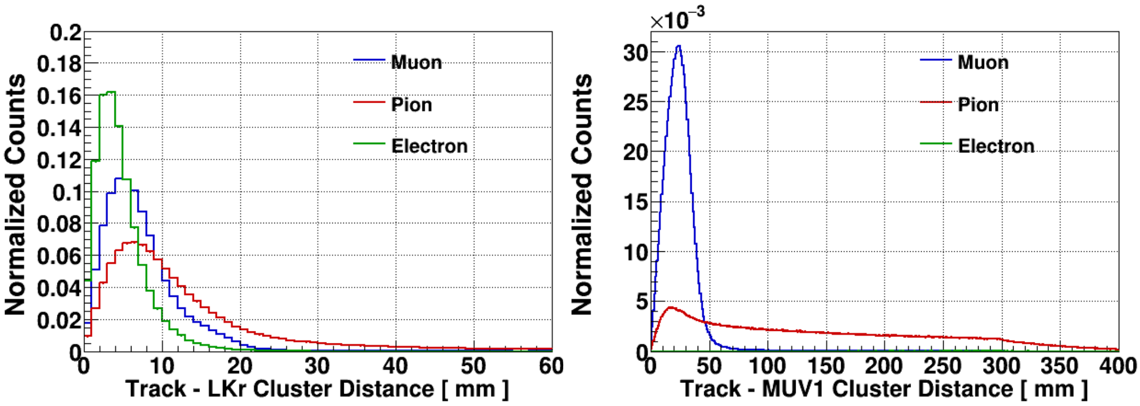

Figure 7.6 – Distance between track extrapolation and reconstructed shower position: at the LKr on the left, at the MUV1 on the right.

Distance between track extrapolation and reconstructed cascade The distance between the reconstructed cascade positions and the expected track impact point at the front face of the calorimeters provides further discrimination power.

The characteristics of the processes involved in muon, pion and positron interaction with the calorimeters material results in a different reconstruction of the cascade position. As described in Section 7.2 the impact of multiple scattering on electromagnetic and hadronic showers is consistently different. Electrons have narrow showers and them position can be determined very precisely. However, the reconstructed position correspond to the track extrapolation at the depth where the shower maximum is reached – i.e. roughly 35 cm (45 cm) for 10 GeV (50 GeV) electrons – determining an offset with respect to the track extrapolation at the entrance of the LKr.

Hadronic cascades are instead prone to multiple scattering effects. The reconstructed position of the shower in the calorimeters is, therefore, much less precise. Since pions reach in most of the cases the HAC, the reconstructed position in the LKr is mostly located after the center of the detector. Instead, the HAC absorbs almost every impinging pion and the reconstructed position is therefore related to the depth at

which most of the energy has been deposited.
Muons in most of the cases do not produce any shower inside the calorimeters, but ionize the material. The energy deposit by ionisation can be considered as uniform along the path. The reconstructed muon position coincide, therefore, to the track extrapolation at the center of the active material.
The BDT algorithm considers the distance between the track extrapolation and reconstructed position in:

- **LKr:** the fine transverse segmentation of the LKr allows to distinguish the offsets in the different particle categories (left of Figure 7.6).
- **MUV1:** the largest fraction of the energy in the hadron calorimeter is collected by the MUV1. Combining the spatial information of the front and back modules would therefore worsen the resolution (the transverse segmentation in the MUV2 is 12 cm instead of 6 cm like in the MUV1), while adding an almost negligible contribution to the separation power. In the track-MUV1 distance the different precision in the position reconstruction of muon and pion events is clearly visible. A non-physical value for the distance of -1 is used in case no energy is found in the MUV1 (right of Figure 7.6).

7.4 Training Configurations

The TMVA framework provides a large freedom in the selection of the Boosted Decision Trees algorithm settings. The analysis type used for the particle identification task is the `MultiClass` analysis, namely the task of determining the compatibility of a input event to several (more than two) categories. In such configuration the boosting method for the BDT algorithm is fixed to the Gradient algorithm described in Section 7.1.3.
The optimal BDT configuration is obtained by varying the following training parameters (names as defined in the TMVA framework):

- `NTrees`: represents the number of decision trees built in the forest. In the `MultiClass` configuration, the problem is subdivided in as many signal-background classification tasks as the number of considered categories. The number of trees specified is therefore multiplied by the number of defined classes (in this case three).
- `MaxDepth`: the maximum number of split steps built in each decision tree.

- `MinNodeSize`: provides a simple, but powerful, tool to avoid the over-training problem. It defines the minimum fraction (in percent) of the initial statistics needed in a node in order to continue the growing of the tree.
- `Ncuts`: at each node splitting all the input variables are tested to verify which one provides the best signal-background separation. This parameter defines how many points in the variable range have to be tested to find the maximum signal-background discrimination.

The variation of the described parameters results in a change of the BDT algorithm performance. As benchmark of the performance the distribution of the muon efficiency as function of the pion efficiency is chosen. This distributions are obtained by varying the lower cut on the probability that the tested particle is a pion provided by the algorithm (the description of the technique is in Section 7.1.3).
The effect of each parameter variation is studied independently to the others.

7.4.1 MaxDepth Parameter Optimisation

The theory of boosting suggests that the best performance is achieved by combining weak classifiers rather than strong ones. Therefore, the growing of each decision tree in the forest should be constrained to a limited number of node splits. The TMVA team suggests to limit this depth to a value of 3 [45]. However, studies performed within the MiniBooNe collaboration [47] showed better performance with larger tree sizes than smaller ones.
The dependency of the performance on the `MaxDepth` parameter is verified for three different values – 3, 5, and 10 – in forests counting 50, 150, and 300 trees. The other parameters are kept to the values suggested by the TMVA user guide (`MinNodeSize` $= 5\%$ and `Ncuts` $= 20$).
Figure 7.7 shows the results of the test. Only the method with 50 trees benefits of the increase of the maximal tree depth from 3 to 5, worsening when increasing further to a value of 10. For larger forests there is almost equivalence between a parameter value of 3 or 5, but the training fails[1] in the `MaxDepth` $= 10$ case.
A simpler tree structure allows faster processing of the data and is less prone to over-fitting problems, therefore the `MaxDepth` $= 3$ configuration is chosen as optimal condition.

---

[1] Since the structure of a decision trees is quite simple, a failure of the training is not foreseen. However the gradient boosting provided by the TMVA framework – only option for the discrimination between several classes – transforms the decision trees into pseudo-functions (regression trees) that in some training configurations provide a Not-a-Number (*NaN*) error as response. In this case the train is defined as failed.

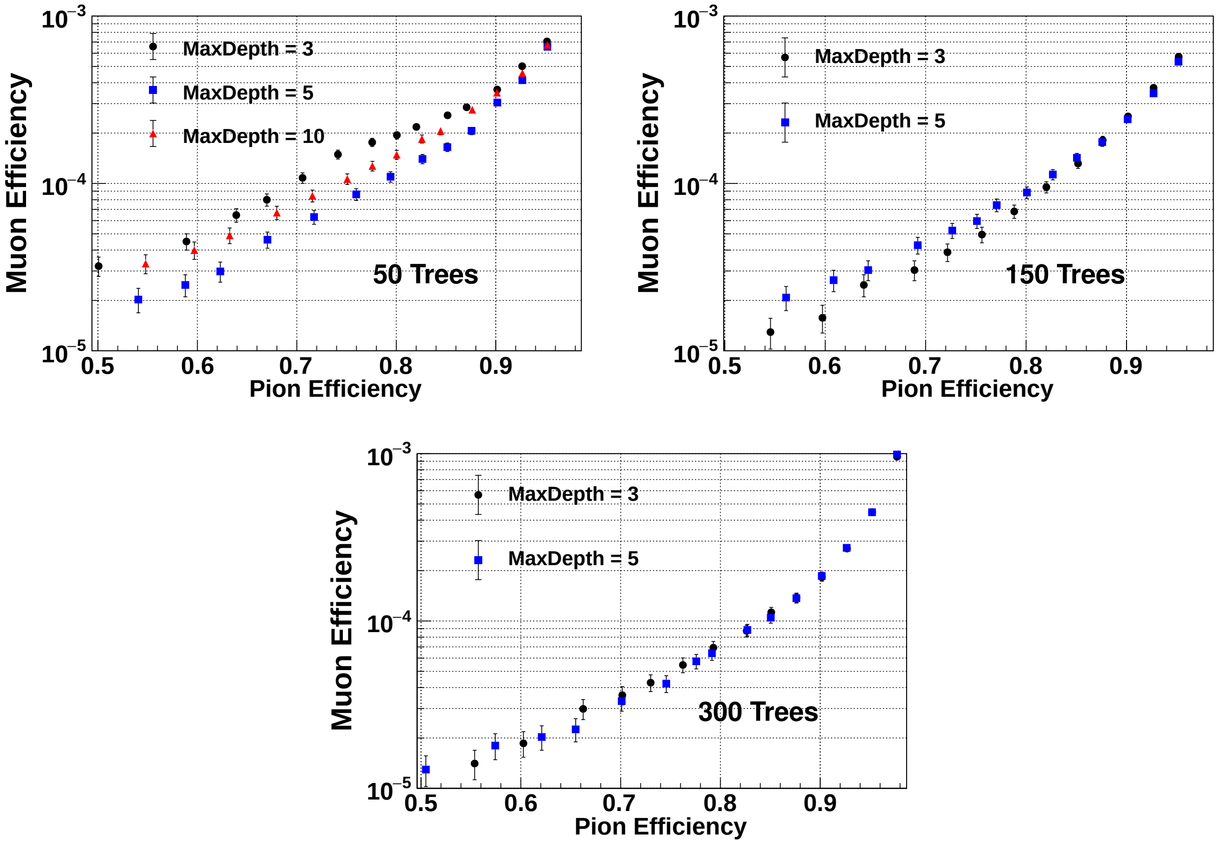

Figure 7.7 – Muon efficiency as a function of the pion efficiency when varying the `MaxDepth` parameter for forests with 50, 150 and 300 trees.

7.4.2 Impact of the Parameter MinNodeSize

The parameter `MinNodeSize` is useful to avoid over-fitting of the training sample by imposing a minimum fraction of the training signal and background events in a node to proceed in the growing of the tree.

An increase of the required `MinNodeSize` is expected to provide stronger protection against over-training, but also to reduce the classifier performances because of the smaller flexibility of the algorithm.

The classification capability is tested for four values of the `MinNodeSize` parameter – 1%, 2.5%, 5%, and 10% – applied to forests of 50, 150, 300 and 500 trees.

The test results are shown in Figure 7.8. Values of 1%, 2.5% and 5% provide similar performances, while the 10% configuration reaches similar results only in the method with 300 trees. However, the training in the case of `MinNodeSize` = 1% fails for the forests of 300 and 500 trees. In the latter case also the 10% configuration leads to a training failure.

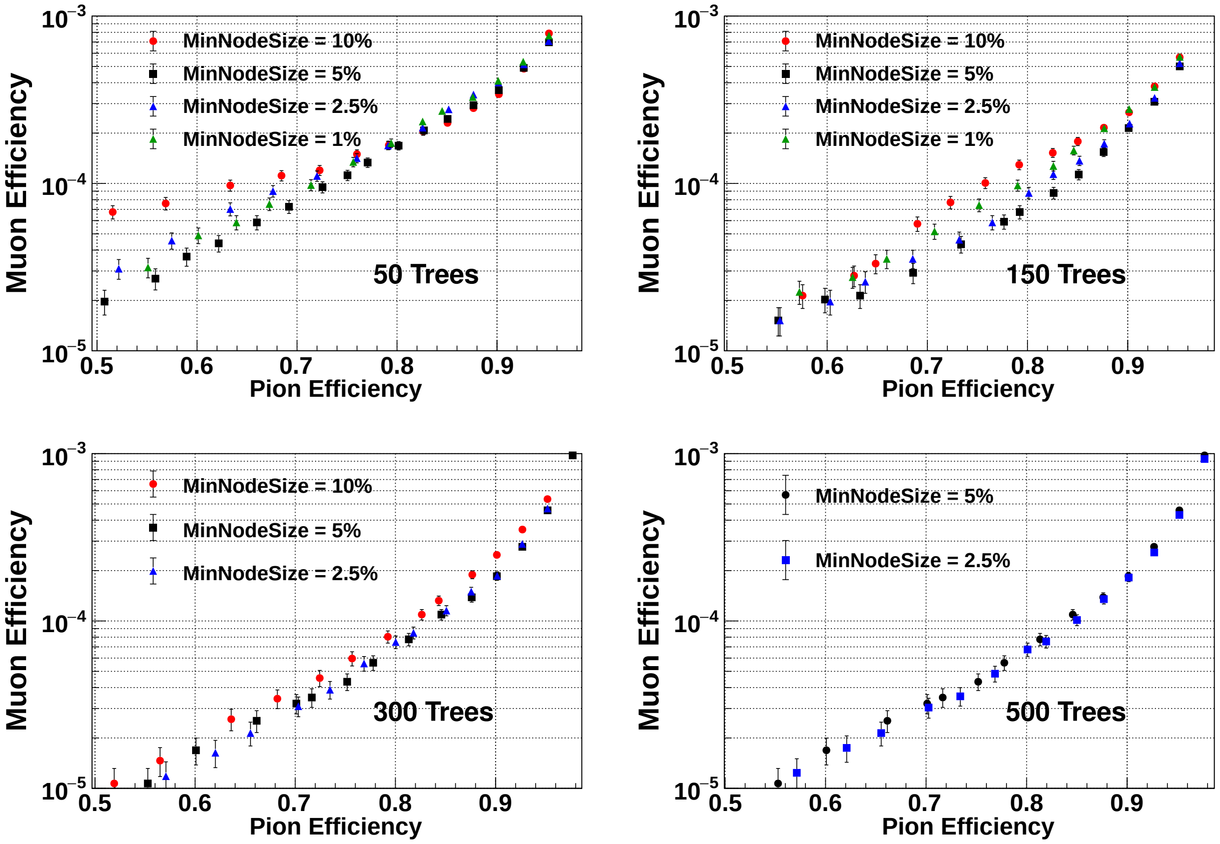

Figure 7.8 – Muon efficiency as function of the pion efficiency when varying the `MinNodeSize` parameter for forests with 50, 150, 300, and 500 trees.

The value `MinNodeSize` = 5%, provides a better protection against statistical fluctuation in the training sample without introducing any significant degradation of the performance (with respect to the 2.5% option) and is therefore chosen as working condition.

7.4.3 Quantization of the Cut Value (Ncuts)

The growing of a decision tree implies to determine the best separating variable and the optimal cut value at each node. This determination is performed by defining a number of test points (`Ncuts`) within the working range of the considered variable and looking for the one providing the largest separation. A small number of test points guarantees a faster training, but may result in sub-optimal performance. A finer segmentation provides a more accurate determination of the optimal separation point, but is more easily affected by statistical fluctuations in the training sample. The variation of the BDT algorithm performance is tested for five values of the segmentation – 20, 50, 100, 200, and 500 – with different forest sizes (50, 150, 300, and 500 trees). The optimized values `MaxDepth` = 3 and `MinNodeSize` = 5% are used.

Figure 7.9 shows the comparison of the tested configurations. The performance of the classifier does not appear to be considerably affected by the segmentation of the variables range (except for the forest with 50 trees where `Ncuts` = 100 provides significantly better results). However for larger forests, 300 and 500 trees, the finer segmentation results in an unstable training configuration: `Ncuts` = 200 fails the training in both the case, `Ncuts` = 500 in the 200 trees forest.

The value `Ncuts` = 100 is defined as working condition because provides, within statistical uncertainty, the best performance in all the tested configurations.

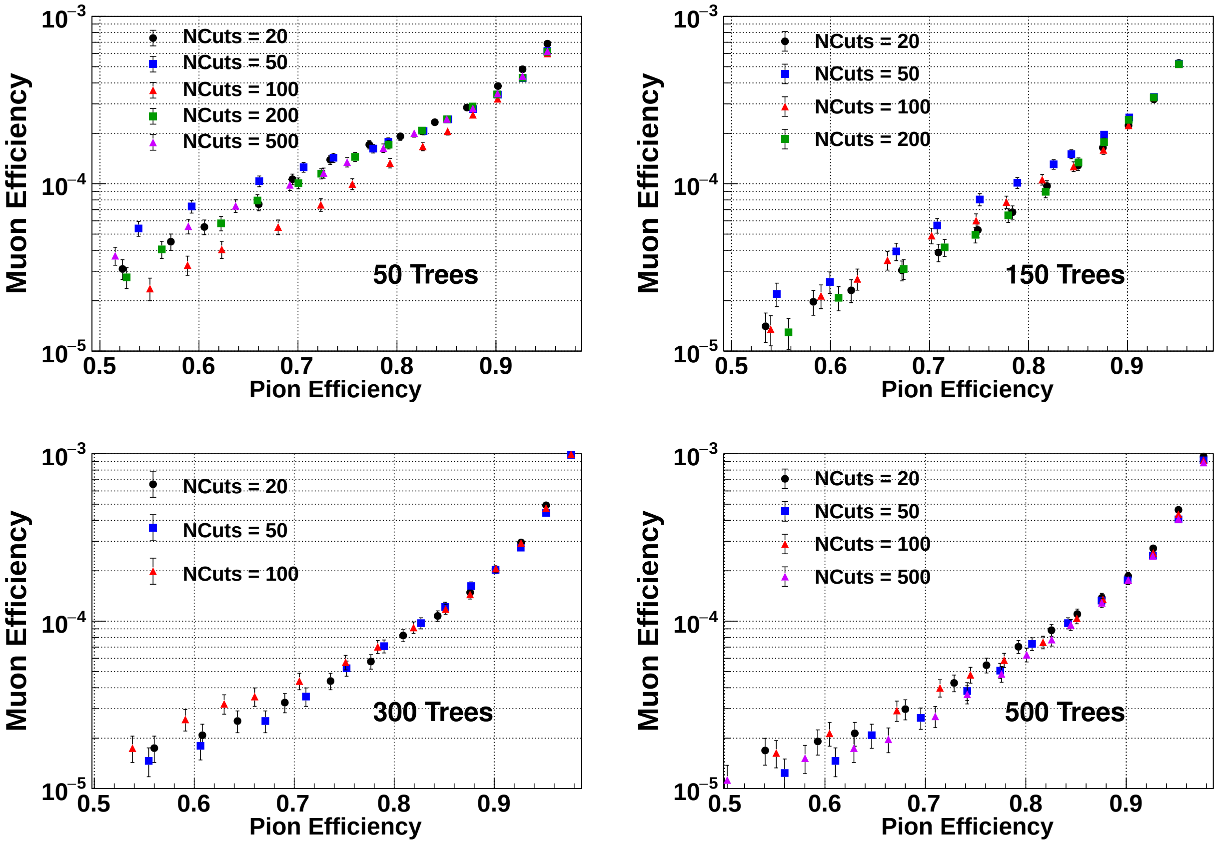

Figure 7.9 – Muon efficiency as function of the pion efficiency when varying the `Ncuts` parameter for 50, 150, 300 and 500 trees forests.

7.4.4 Forest Size Optimization

The optimal forest size is determined by comparing the muon-pion efficiencies distribution with the $K^+ \to \pi^+ \nu \bar{\nu}$ measurement constaints: track momentum in $[15, 35]$ GeV/c and MUV3 veto. Figure 7.10 (left) shows the comparison of the performance provided by four forest sizes: 50, 150, 300, and 500 trees. The variations of the method performance are small compared with the statistical uncertainties of the measured muon efficiency. However the classifier implementing 50 decision trees provides a systematically worse muon rejection and can therefore be excluded. The largest forest tested seems, instead, to provide the best results but the small difference compared to the uncertainty does not allow to identify the best configuration. Larger statistics and a more reliable test sample – with respect to the performance expected in the $K^+ \to \pi^+ \nu \bar{\nu}$ analysis – is provided by the performing the test sample selection on data collected directly by the physics trigger (Mask 1)[2].

Figure 7.10 (right) shows the dependency of the classifier performance to the forest size. The muon suppression is clearly worse because a large fraction of the MUV3 rejection is already obtained at trigger level.

The statistical uncertainty is now negligible, the forest with 150 trees provides slightly worse results. The classifiers implemented with 300 and 500 decision tree provide equivalent results. In the approach of keeping the BDT algorithm faster, the `NTrees` = 300 configuration is chosen as final working condition.

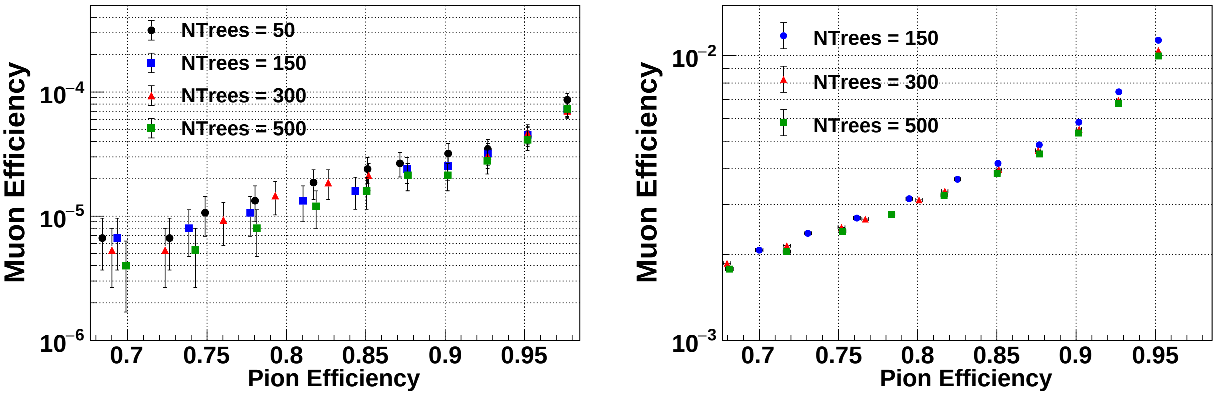

Figure 7.10 – Muon efficiency as function of the pion efficiency, including MUV3 veto contribution, for different forest sizes: on the left for the Control Trigger data and on the right for the data from the physics trigger mask 1.

---

[2] In the optimisation of the others parameters it has been considered preferable to use an unbiased sample to optimize the performance for general analysis.

7.5 Particle Identification Performance

The particle identification capabilities of the trained Boosted Decision Trees algorithm are reviewed in the following. The results are presented in the form of efficiency of the selected particle versus that of the considered background in the track momentum range $[10, 70]$ GeV$/c$ – the evaluation is performed in steps of 1×10^{-3} of the classifier probability response and, for better visualization, reported in steps of about 2.5% of the signal efficiency for pion and positron identification. The efficiency dependence on the track momentum is also shown for a minimum cut on the (considered) signal probability ($P(\pi/\mu/e)$) at 0.8.

Pion Identification The selection of pions using the BDT algorithm – with the MUV3 veto not applied – allows to achieve a background efficiency of about 5×10^{-3} for electrons and at the 10^{-4} level for muons, while keeping the pion efficiency at 90% as shown in Figure 7.11.

Figure 7.12 shows the efficiency as function of the momentum for pion, muon and positron when requiring the classifier probability for the pion category above 80%. The strong variation of the pion efficiency at the lower track momenta, below 30 GeV$/c$, is related to the worse hadronic energy resolution as shown in Chapter 5 Figure 5.43.

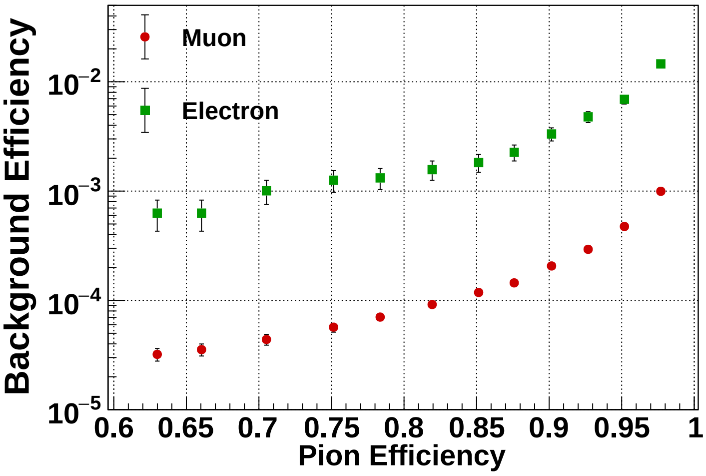

Figure 7.11 – Muon and electron efficiencies as function of the pion efficiency.

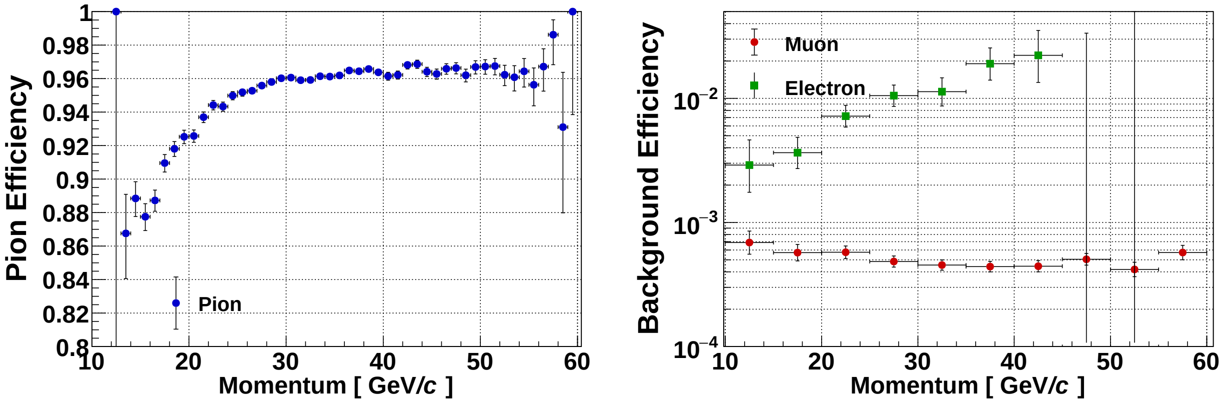

Figure 7.12 – Pion, muon and electron efficiencies as function of the momentum for $P(\pi) > 0.8$.

Muon Identification The selection of muon signals can be performed very efficiently with the trained classifier. For 99% of the muons passing the selection cut, the pion rejection factor is about 10^3 and that for electrons above 10^4 (the estimate is limited by the size of the test sample: about 15000 electrons) as shown in Figure 7.13. The muon efficiency is very stable with respect to the track momentum, while the pion rejection shows a mirrored behaviour compared to the efficiency in the selection case (Figure 7.14). The rejection of pions is limited by the $\pi^+ \to \mu^+$ decays happening at the entrance of the calorimeters.

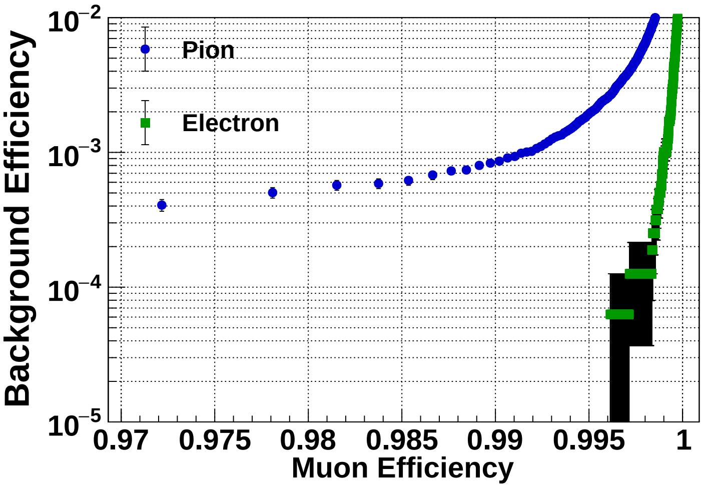

Figure 7.13 – Pion and electron efficiencies as function of the muon efficiency.

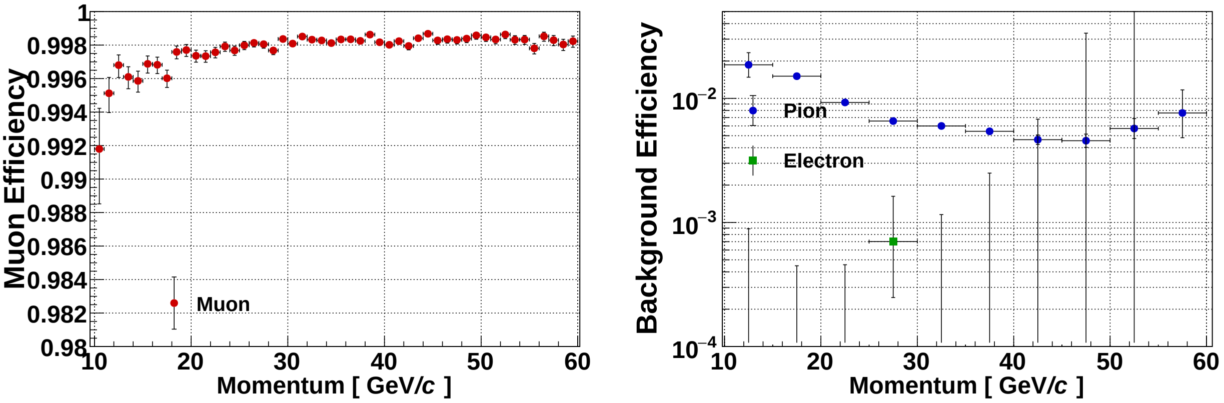

Figure 7.14 – Muon, pion and electron efficiencies as function of the momentum for $P(\mu) > 0.8$.

Electron Identification The electron-muon separation is one of the tasks the BDT algorithm can perform best. The muon efficiency approaches the value of 2×10^{-6}, touching the limit of the sample purity estimated in Section 6.2, already at a positron efficiency of 95%. The pion rejection is, instead, more complicated. Hadronic showers have a fraction of energy released electromagnetically which strongly varies on a event-by-event basis. Moreover the charge exchange process $\pi^+ + n \rightarrow \pi^0 + p^+$ and the $\pi^+ \rightarrow e^+\nu$ decay, produce purely electromagnetic cascades. This effect is clearly visible in Figure 7.15 as the pion efficiency reaches 10^{-3} at 85% of electron efficiency and then decreases very slowly.

Figure 7.16 shows the efficiency as function of the momentum for signal and backgrounds when requiring a classifier probability above 80%.

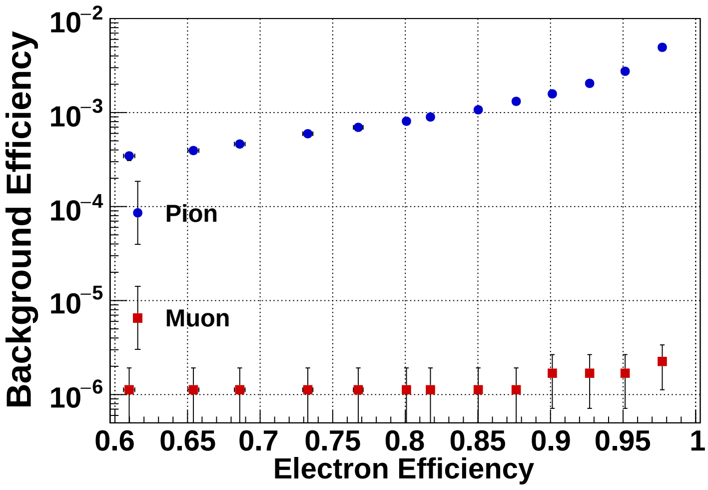

Figure 7.15 – Muon and pion efficiencies as function of the electron efficiency.

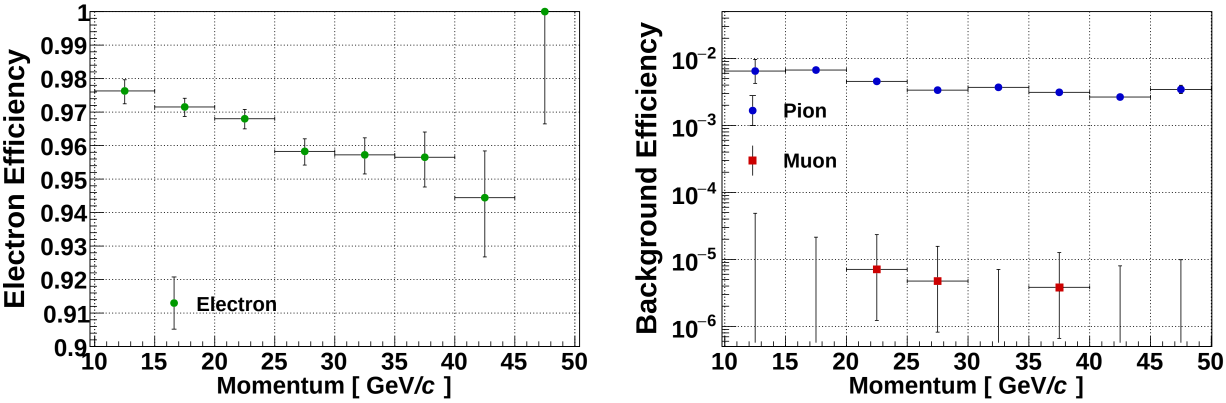

Figure 7.16 – Electron, muon and pion efficiency as function of the momentum when requiring $P(e) > 0.8$.

7.6 Muon-Pion Separation for the $K^+ \to \pi^+\nu\bar{\nu}$ Measurement

The main goal of the NA62 experiment is the measurement of the $K^+ \to \pi^+\nu\bar{\nu}$ branching ratio.

In the analysis, the $K^+ \to \pi^+\nu\bar{\nu}$ signal region is defined for pion momenta in the range $[15, 35]$ GeV/c, with a online muon rejection provided by the MUV3. The combined effect of MUV3 and calorimeters is expected to provide a muon rejection of about 10^5 at a pion efficiency of 90%.

7.6.1 MUV3 Veto Optimization

The muon rejection provided by the MUV3 is not optimal when requiring a spatial match. The deflection of the particle trajectory when crossing the material can be considerably large, in particular in case of large energy deposits in the iron in front of the MUV3. Figure 7.17 shows the distribution of the time difference between RICH and MUV3 in the muon test sample, after the MUV3 veto described in Section 6.1.3. A clear accumulation of events with an in-time signal in the fast muon veto is found. The muon rejection is therefore improved by requiring no signal in the MUV3 within 5 ns from the reference event time, without any spatial requirement.

The residual inefficiency of 2×10^{-3} is mainly due to muons travelling through the detector within the gap between two scintillators.

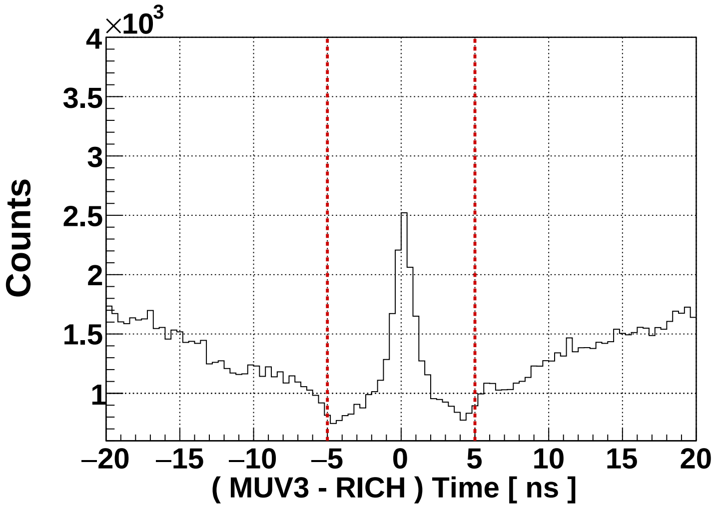

Figure 7.17 – Time difference between RICH and, not previously matched, MUV3 signals. The red lines show the cut values.

7.6.2 Results

The combined effect of MUV3 and calorimeters is clearly visible in the muon-pion separation, for particles in the momentum range $[15, 35]$ GeV$/c$, shown in Figure 7.18 as muon versus pion efficiency. A muon rejection of about 10^5 is achievable with a pion efficiency between 85% and 90%, perfectly in agreement with the design performance.

Figure 7.19 shows the pion and muon efficiencies as function of the lower cut on the pion signal probability $P(\pi)$ obtained from the BDT algorithm.

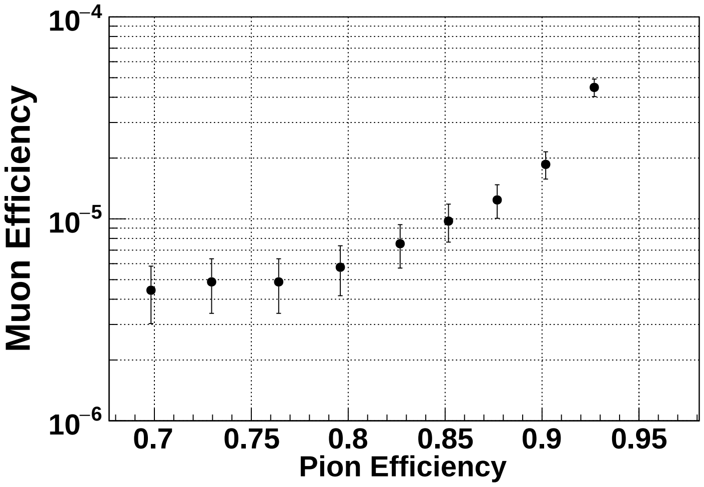

Figure 7.18 – Muon efficiency as function of the pion efficiency for the $K^+ \to \pi^+\nu\bar{\nu}$ measurement.

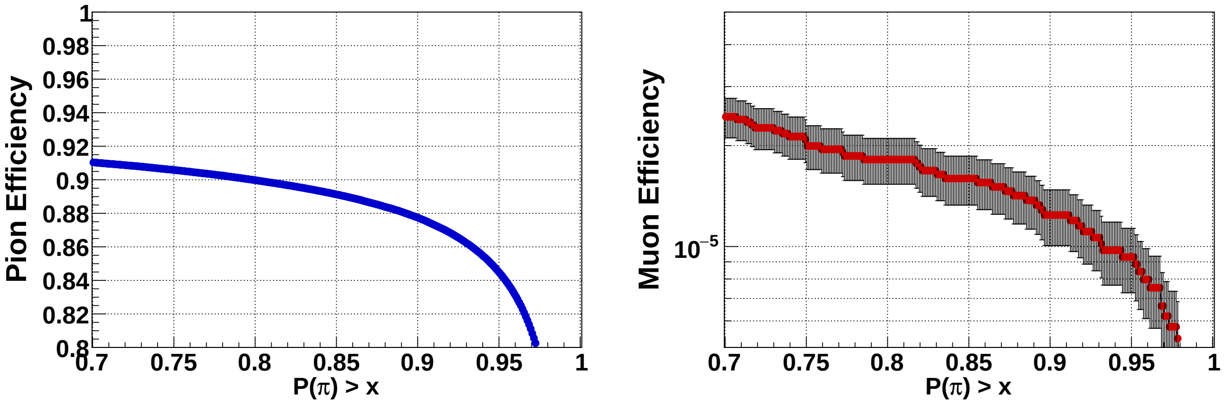

Figure 7.19 – Pion and muon efficiencies as function of the required lower limit on the classifier response for the pion identification probability.

Despite the muon-pion separation is mainly devoted to the suppression of the $K^+ \to \mu^+\nu_\mu$ background, pions from $K^+ \to \pi^+\nu\bar{\nu}$ have a different momentum distribution with respect to those from $K^+ \to \pi^+\pi^0$. The muon-pion separation has therefore to be estimated as function of the track momentum. Figure 7.20 shows pion and muon efficiencies as function of the track momentum for the cut $P(\pi) > 0.8$. The discrimination performance is slightly worse for particles of lower momenta (below 20 GeV/c) with a pion efficiency between 80% and 90% and about 4×10^{-5} muon efficiency. However in this region the kinematic separation between the $K_{\mu 2}$ and the $K^+ \to \pi^+\nu\bar{\nu}$ signal region provides a better protection against the muon background. At larger track momenta both pion efficiency and muon rejection improve reaching values of about 91% and 1.1×10^{-5} respectively.

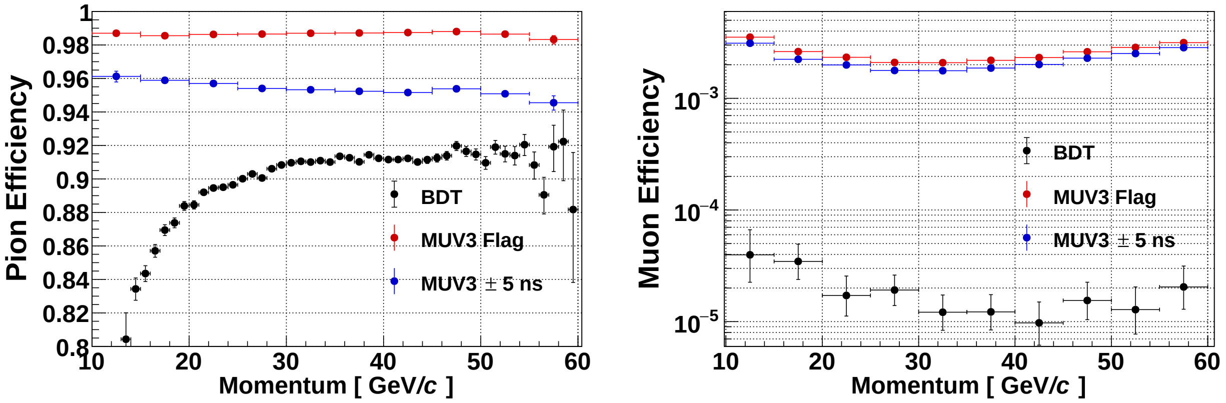

Figure 7.20 – Pion and muon efficiencies as function of the momentum after applying a MUV3 veto and with the pion identification with the calorimeters ($P(\pi) > 0.8$).

Conclusion

The NA62 experiment, currently acquiring data at CERN, aims to measure the $K^+ \to \pi^+\nu\bar{\nu}$ branching ratio with 10% precision, probing the Standard Model (SM) validity up to energy scales of hundreds TeV. The branching ratio of this process is extremely tiny, as it is predicted by the SM to be $(8.4 \pm 1.0) \times 10^{-11}$, and its measurement requires a strong suppression of the background. In particular, the $K^+ \to \mu^+\nu_\mu$ decay represent one of the major sources of background for the measurement. Hence, an efficient particle identification system for the μ-π discrimination is a crucial requirement for NA62. The calorimeters provide a leading contribution in this task.

The calibration of the energy response of the calorimeters is a crucial step to achieve the ultimate particle identification performance. A novel technique for the calibration of the hadron calorimeter (HAC) response at the electromagnetic scales has been developed, exploiting stopped high energy muons. After the full hadronic calibration, the HAC response to pions shows remarkable performance in terms of linearity and energy resolution. A preliminary inter-calibration for hadronic showers involving both the electromagnetic and the hadron calorimeters has been determined, based on the procedure employed in the NA31 experiment. The calorimeter response shows a significant improvement with respect to the original configuration. However, advances in this context are feasible and would surely worth the time investment.

A particle identification algorithm combining the information about energy and shape of the showers detected by the calorimeters has been developed exploiting the Boosted Decision Trees technique. The free parameters of the algorithm have been tuned in order to achieve the best performance in the μ-π separation for the $K^+ \to \pi^+\nu\bar{\nu}$ branching ratio measurement. The obtained performance satisfies the design requirement of the experiment: 90% pion efficiency for a 10^5 muon suppression factor, when used in combination with the MUV3 veto. Moreover, the algorithm showed excellent discrimination capabilities for the selection of muons and electrons.

Bibliography

[1] M. K. Gaillard, P. D. Grannis, and F. J. Sciulli. "The Standard model of particle physics". In: *Rev. Mod. Phys.* 71 (1999), S96–S111.

[2] S. L. Glashow, J. Iliopoulos, and L. Maiani. "Weak Interactions with Lepton-Hadron Symmetry". In: *Phys. Rev.* D2 (1970), pp. 1285–1292.

[3] A. J. Buras et al. "$K^+ \to \pi^+ \nu\overline{\nu}$ and $K_L \to \pi^0 \nu\overline{\nu}$ in the Standard Model: status and perspectives". In: *JHEP* 11 (2015), p. 033.

[4] F. Mescia and C. Smith. "Improved estimates of rare K decay matrix-elements from Kl3 decays". In: *Phys. Rev.* D76 (2007), p. 034017.

[5] A. J. Buras et al. "Can we reach the Zeptouniverse with rare K and $B_{s,d}$ decays?" In: *JHEP* 11 (2014), p. 121.

[6] J. K. Ahn et al. "Experimental study of the decay $K^0_L \to \pi^0 \nu\overline{\nu}$". In: *Phys. Rev.* D81 (2010), p. 072004.

[7] A. V. Artamonov et al. "Study of the decay $K^+ \to \pi^+ \nu\overline{\nu}$ in the momentum region $140 < P_\pi < 199$ MeV/c". In: *Phys. Rev.* D79 (2009), p. 092004.

[8] T. Yamanaka et al. "The J-PARC KOTO experiment". In: *Progress of Theoretical and Experimental Physics* 2012.1 (2012), 02B006.

[9] K. Shiomi. "Status of the J-PARC KOTO experiment". In: *Journal of Physics: Conference Series* 800.1 (2017), p. 012022.

[10] M. Kobayashi and T. Maskawa. "CP Violation in the Renormalizable Theory of Weak Interaction". In: *Prog. Theor. Phys.* 49 (1973), pp. 652–657.

[11] N. Cabibbo. "Unitary Symmetry and Leptonic Decays". In: *Phys. Rev. Lett.* 10 (1963), pp. 531–533.

[12] M. Tanabasi et al. "2018 Review of Particle Physics". In: *Phys. Rev.* D.98 (2018), p. 010001.

[13] L. Wolfenstein. "Parametrization of the Kobayashi-Maskawa Matrix". In: *Phys. Rev. Lett.* 51 (1983), p. 1945.

[14] A. J. Buras, F. Schwab, and S. Uhlig. “Waiting for precise measurements of $K^+ \to \pi^+\nu\bar{\nu}$ and $K_L \to \pi^0\nu\bar{\nu}$”. In: *Rev. Mod. Phys.* 80 (2008), pp. 965–1007.

[15] V. G. Luth. “Determination of the CKM matrix element |V(cb)| from semileptonic B decays”. In: *Proceedings, 32nd International Conference on High Energy Physics (ICHEP 2004): Beijing, China, August 16-22, 2004*. 2004, pp. 883–887.

[16] R. Aaij et al. “Precision measurement of the B^0_s-$\bar{B}^0_s$ oscillation frequency with the decay $B^0_s \to D^-_s\pi^+$”. In: *New J. Phys.* 15 (2013), p. 053021.

[17] J. K. Ahn et al. “A new search for the $K_L \to \pi^0\nu\bar{\nu}$ and $K_L \to \pi^0 X^0 decays$”. In: *Progress of Theoretical and Experimental Physics* 2017.2 (2017), p. 021C01.

[18] M. Moulson et al. “Prospects for an experiment to measure BR($K_L \to \pi^0\nu\bar{\nu}$) at the CERN SPS”. In: *J. Phys. Conf. Ser.* 800.1 (2017), p. 012037.

[19] R. Marchevski. “First NA62 Results on $K^+ \to \pi^+\nu\bar{\nu}$”. In: Presentation at 53nd Rencontres de Moriond Electroweak, La Thuile, Italy, 2018.

[20] A. Ceccucci et al. *NA62 Technical Design Report*. 2010. URL: `http://na62.web.cern.ch/na62/Documents`.

[21] E. Cortina Gil et al. “The beam and detector of the NA62 experiment at CERN”. In: *Journal of Instrumentation* 12.05 (2017), P05025.

[22] G. Lanfranchi. “Search for Hidden Sector particles at NA62”. In: *PoS* EPS-HEP2017 (2017), p. 301.

[23] *Figure produced by Silvia Martellotti.*

[24] B. G. Taylor. “Timing distribution at the LHC”. In: 8th Workshop on Electronics for LHC Experiment, Colmar, CERN-LHCC-G-014, 2002.

[25] ALICE Collaboration. URL: `http://alicetrigger.web.cern.ch/alicetrigger/alice_main.htm`.

[26] *NA62 Analysis Framework documentation.* URL: `https://na62-sw.web.cern.ch/sites/na62-sw.web.cern.ch/files/doxygen/index.html`.

[27] D. C. Carey. “TURTLE (Trace Unlimuted Rays Through Lumped Elements): A computer program for simulating charged particle beam transport systems”. In: FERMILAB-NAL-064, 1971.

[28] J. Allison et al. “Recent developments in Geant4”. In: *Nuclear Instruments and Methods in Physics Research Section A: Accelerators, Spectrometers, Detectors and Associated Equipment* 835 (2016), pp. 186–225.

[29] C. Gatti. “Monte Carlo simulation for radiative kaon decays”. In: *European Physical Journal C* 45 (2006), pp. 417–420.

[30] J. R. Batley et al. “Empirical parameterization of the $K^+ \to \pi^+\pi^0\pi^0$ decay Dalitz plot”. In: *Phys. Lett.* B686 (2010), pp. 101–108.

[31] V. Fanti et al. “The Beam and detector for the NA48 neutral kaon CP violations experiment at CERN”. In: *Nucl. Instrum. Meth.* A574 (2007), pp. 433–471.

[32] G. Ruggiero et al. “NA62/P-326 Status Report”. In: CERN-SPSC-2007-035, 2007. URL: `https://na62.web.cern.ch/na62/Documents/spsc-2007-035.pdf`.

[33] A. Ceccucci et al. “The NA62 liquid Krypton calorimeter’s new readout system”. In: *Journal of Instrumentation* 9.01 (2014), p. C01047.

[34] *Figure produced by Rainer Wanke.*

[35] I. Antcheva et al. “ROOT - A C++ framework for petabyte data storage, statistical analysis and visualization”. In: *Computer Physics Communications* 180.12 (2009), pp. 2499–2512.

[36] D. Soldi. “The FPGA-based first level trigger for the NA62 Experiment at CERN SPS.” PhD Thesis, Università degli Studi di Torino. 2017.

[37] M. Mirra. “Search for invisible dark photons from π^0 decays at NA62”. In: Presentation at 53nd Rencontres de Moriond QCD, La Thuile, Italy. 2018.

[38] L. Peruzzo. “Search for $\pi^0 \to$ invisible decay at NA62”. PhD Thesis, Johannes-Gutemberg-Universität Mainz. To be published.

[39] C. W. Fabjan and F. Gianotti. “Calorimetry for particle physics”. In: *Rev. Mod. Phys.* 75 (2003), pp. 1243–1286.

[40] D. E. Groom, N. V. Mokhov, and S. I. Striganov. “Muon stopping power and range tables 10-MeV to 100-TeV”. In: *Atom. Data Nucl. Data Tabl.* 78 (2001), pp. 183–356.

[41] T. Skwarnicki. “A study of the radiative CASCADE transitions between the Upsilon-Prime and Upsilon resonances.” PhD Thesis, INP, Cracow. 1986.

[42] P. Adragna et al. “Testbeam studies of production modules of the ATLAS Tile Calorimeter”. In: *Nuclear Instruments and Methods in Physics Research Section A: Accelerators, Spectrometers, Detectors and Associated Equipment* 606.3 (2009), pp. 362–394.

[43] G. Dietrich. “Aufbau, Kalibration und Test des Hadronkalorimeters für das NA31 am CERN.” PhD Thesis, Universität Dortmund. 1986.

[44] R. Wigmans. “Calorimetry”. In: *Scientifica Acta* 2.1 (2008), pp. 18–55.

[45] A. Hoecker et al. “TMVA - Toolkit for Multivariate Data Analysis”. In: *ArXiv Physics e-prints* (2007).

[46] R. E. Schapire and Y. Freund. *"Boosting: Foundations and Algorithms"*. The MIT Press, 2012.

[47] H. Yang, B. Roe, and J. Zhu. “Studies of boosted decision trees for MiniBooNE particle identification”. In: *Nucl. Instrum. Meth.* A555 (2005), pp. 370–385.